Spontaneous Emission in TMDs

Exciton Dispersion, Lifetimes and Purcell Factor

Group 5.330b

June 3, 2020

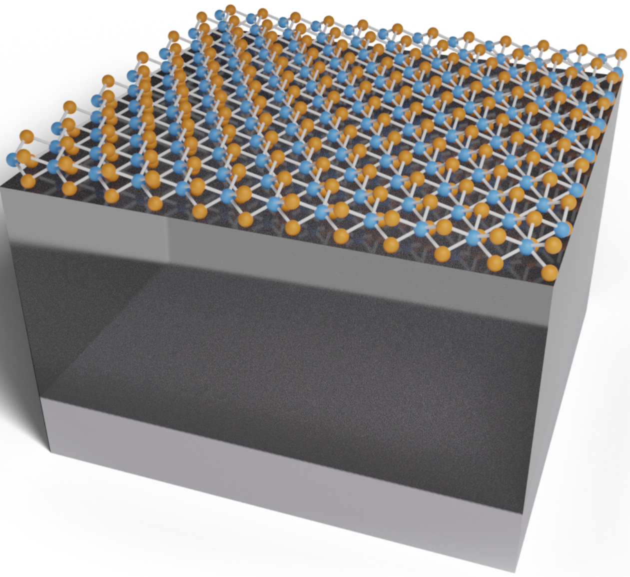

Aalborg University
Physics Master's Thesis

Title:
Spontaneous Emission of TMDs

Project timeframe:
1st of September 2019 - 3rd of June 2020

Project group:
Group 5.330b

Group members:
Carl Emil Mørch Nielsen
Lars Merring-Mikkelsen
Mikkel Ohm Sauer

Supervisors:
Thomas Garm Pedersen

Total page count: 82 pages

Appendix page count: 6 pages

Abstract

Based on DFT-calculations performed using GPAW, the excitonic, optical, and radiative properties of molybdenym- and tungsten-based TMDs have been examined in detail by use of the Bethe-Salpeter equation in a plane-wave basis with a Keldysh potential. In particular, the sheet conductivity and absorbance have been modelled as well as the radiative lifetime of bright excitonic states. The excitonic lifetimes are based on center-of-mass momenta dispersions in the optical regime, which are found by first using an interpolation scheme on high density DFT calculations and then iteratively computing the BSE.

Moreover, the Purcell enhancement of the lifetime in a simple dielectric geometry, as well as a slightly more complicated optical cavity has been examined. Finally, the modelled data has been compared to PL and absorption measurements and other theoretical data, which shows decent agreement.

A special thanks to Thomas Garm Pedersen for providing guidance and feedback throughout the entirety of this project.

Another thanks to Thomas Søndergaard for sharing his expertise in modelling of photonics, and to Alireza Taghizadeh for helping us with the use of GPAW.

Contents

1 Introduction

As the semiconductor industry is nearing the limits of performance improvements to the current technologies regarding silicon, there is a constant search for new non-traditional materials. In this search, 2D materials have received an increased interest due to their vast amount of possibilities in micro electronics. Graphene is a material which has gotten a significant amount of attention since its experimental discovery. This is due to graphene consisting of a single sheet of atoms, which can be obtained experimentally, resulting in the many unique properties [1].

However, graphene is just one material out of an endless amount of other 2D materials with fascinating properties. A such group of 2D materials could be the transition metal dichalcogenides (TMDs). Layers of TMDs are held together by weak van der Waals forces, and it is therefore experimentally feasible to obtain a thickness of a single layer [2]. This project will primarily concern itself with calculations regarding the properties of monolayer TMDs, however the methods developed can easily be used for other 2D materials. To visualize a H-phase TMD, one can look at figure 1.0.1. When a semiconductor absorbs a photon, a collective electronic state will jump to an excited collective state of higher energy. Single-electron transitions occurring between a valence band and a conduction band leaves a hole in the valence band. The hole and the electron will then interact through screened Coulomb forces, which may create a bound state known as an exciton. The exciton will lower the bandgap of the semiconductor, thus one can define an exciton binding energy to be the difference between the fundamental bandgap and the optical bandgap.

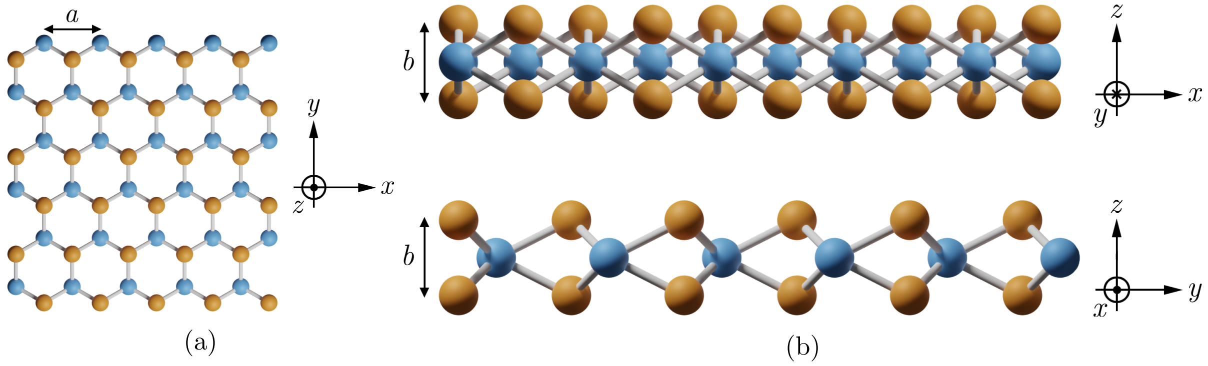

(a)

(b)

Figure 1.0.1: Blue dots indicate a transition metal atom, and orange indicates a chalgogen atom. (a) A topdown-view showing the honeycomb structure and the lattice constant, a, and (b) Planar views showing the second lattice constant, b.

The usual method for describing excitonic states is by solving the Bethe-Salpeter equation. In this project, the Bethe-Salpeter is solved using single electron eigenstates described by a plane wave expansion. In order to obtain all necessary single electron properties, a Density Functional Theory (DFT) calculation can, among others, be performed. We made use of GPAW [3–7], which is a Python-based library developed as an extension to the ASE module. The GPAW library makes use of the projector-augmented wave method [8] in order to perform DFT calculations.

The reason for considering excitonic properties of TMDs is ultimately to accurately model properties related to spontaneous emission. This means, that one needs to consider an interaction picture, where an electromagnetic field carrying some momentum interacts with our 2D material, which severely complicates calculations. In effect, the dispersion relation for excitons should be calculated and then thermally averaged to obtain the radiative lifetimes. In an article by H. Wang et al. they model these lifetimes using a Wannier-Mott model for excitons based on a tight-binding formalism [9]. Based on this they predict radiative lifetimes in the order of nanoseconds at room temperature, as well as a linear temperature dependence. M. Palummo et al. also create a model for calculating this radiative lifetime [10], where they obtain lifetimes around a nanosecond at room temperature as well.

Many have attempted to measure these radiative lifetimes, however, due to the difficulty of manufacturing pristine TMDs without any impurities the measurements are often dominated by non-radiative decay mechanisms [11]. C. Jin et al. claim to have developed a method for describing intrinsic and effective lifetimes of WSe_2 with high precission experimentally [12]. In a set of articles by M. Amani et al. they propose that these impurities can be passivated using either superacid treatment or by gating, achieving quantum yields of up to 100% [13–16]. In these articles, M. Amani et al. measure lifetimes of around 10 nanoseconds. Moreover, using passivating agents, H. M. Bretscher et al. have furthered this process, and thus developed an extended passivation protocol, and find a lifetime around 3 nanoseconds [17].

In relation to this, we also wish to examine the Purcell effect. The Purcell effect describes the enhancement of a material's emission rate with regard to its dielectric environment [18, 19]. As such, this requires modelling the general optical properties such as conductivity which therefore is another focus of this project. In particular, these optical properties can also serve as a benchmark for the exciton states calculated in this project by comparison to calculations made in the software package GPAW, which can be found in the 2D database C2DB [20], or by comparing with experimental observations.

2 Theory

This chapter will concern itself with describing theory needed to explain and model the radiative properties of excitons. Maxwell's equations will serve as a baseline for the quantum interaction picture. In the interaction picture, the quantum mechanical harmonic oscillator formulated in terms of photon quanta becomes relevant, and leads to a quantisation of the free-space electromagnetic field. Moreover, linear perturbation theory will be extremely relevant when describing optical phenomena - both in the single electron case and in the excitonic one. In addition to this, the Bethe-Salpeter equation will be formulated in a base that includes spin-orbit interaction. Furthermore, the optical properties will be discussed, which is centered around the excitonic center-of-mass dispersion. These properties also include those induced by an inhomogeneous dielectric environment, namely the Purcell effect.

2.1 Microscopic Formulation of Maxwell's Equations

For the sake of creating an overview and weave the proceeding sections together, the microscopic Maxwell equations will be presented here to serve as a stepping stone towards more complex theory. They are given as

$$\boldsymbol{\nabla} \cdot \mathbf{E} = \frac{\rho}{\varepsilon_0}, \tag{2.1.1}$$

$$\boldsymbol{\nabla} \cdot \mathbf{B} = 0, \tag{2.1.2}$$

$$\boldsymbol{\nabla} \times \mathbf{E} = -\frac{\partial \mathbf{B}}{\partial t}, \tag{2.1.3}$$

$$\boldsymbol{\nabla} \times \mathbf{B} = \mu_0 \left(\mathbf{J} + \varepsilon_0 \frac{\partial \mathbf{E}}{\partial t} \right), \tag{2.1.4}$$

where $\mathbf{E}$ is the electric field, ρ the charge density, $\mathbf{B}$ the magnetic field and $\mathbf{J}$ the current density. All these quantities are functions of time and position, t and $\mathbf{r}$, respectively, but for ease of notation the arguments are left out. As per usual, equation (2.1.2) can be satisfied by defining the electromagnetic vector-potential, $\mathbf{A}$, such that

$$\mathbf{B} = \boldsymbol{\nabla} \times \mathbf{A}. \tag{2.1.5}$$

Similarly, the electric field can be written as

$$\mathbf{E} = -\boldsymbol{\nabla}\phi - \frac{\partial \mathbf{A}}{\partial t}, \tag{2.1.6}$$

where ϕ is the usual scalar potential. Clearly, this definition of the electric field also satisfies equation (2.1.3). However, the scalar- and vector-potential do not uniquely define the electromagnetic fields. If the pair of potentials, ϕ' and $\mathbf{A}'$ satisfy equations (2.1.5) and (2.1.6), another pair of potentials, ϕ and $\mathbf{A}$, can also be ensured to satisfy the equations by using the relations

$$\phi = \phi' + \frac{\partial \xi}{\partial t}, \tag{2.1.7}$$

$$\mathbf{A} = \mathbf{A}' - \boldsymbol{\nabla}\xi, \tag{2.1.8}$$

where the arbitrary function $\xi \equiv \xi(\mathbf{r}, t)$ is the so-called *gauge function.* It can be seen by insertion, that this pair of potentials serve the exact same purpose for the electromagnetic fields. The gauge can then be specified by some condition. An example of this could be the *Coulomb gauge*, which is defined by letting the vector-potential satisfy

$$\boldsymbol{\nabla} \cdot \mathbf{A} = 0. \tag{2.1.9}$$

For the proceeding sections, the electromagnetic field will generally be in the Coulomb gauge.

2.1.1 Quantisation of the Free-Space Electromagnetic Field

The electromagnetic field is quantised in a *quantisation cavity*, which is simply a cubic region of space of sidelength L without any real boundaries. In such a region, the waves should be travelling and have periodic boundary conditions [21, ch. 4.2]. Moreover, the radiation field can be separated into modes $\mathbf{q}\lambda$, where $\mathbf{q}$ denotes the wave vectors, and λ denotes the unit polarisation vectors. The wave vector for such a confinement is defined by

$$q_x = \frac{2\pi n_x}{L}, \quad q_y = \frac{2\pi n_y}{L}, \quad q_z = \frac{2\pi n_z}{L}, \tag{2.1.10}$$

where $n_x, n_y, n_z \in \mathbb{Z}$. Moreover, the unit polarisation vectors, $\mathbf{e}_{\boldsymbol{\lambda}}$, satisfy the Coulomb gauge condition, if and only if they are transverse. If the basis was expanded by a non-transverse unit vector, the resultant vector-potential would have non-vanishing divergence. Additionally, they are chosen to be mutually orthogonal. Therefore, the following two criteria are satisfied:

$$\mathbf{e}_{\mathbf{q}\lambda} \cdot \mathbf{q} = 0, \quad \mathbf{e}_{\mathbf{q}\lambda} \cdot \mathbf{e}_{\mathbf{q}\lambda'} = \delta_{\lambda,\lambda'}, \tag{2.1.11}$$

where $\delta_{\lambda,\lambda'}$ is the Kronecker delta. The quantisation of the electromagnetic field is now performed by associating each mode of the radiation field with the one-dimensional quantum mechanical oscillator. The destruction and creation operators for a cavity mode $\mathbf{q}\lambda$ can be written as

$$\hat{a}_{\mathbf{q}\lambda} \left| n_{\mathbf{q}\lambda} \right\rangle = n_{\mathbf{q}\lambda}^{\frac{1}{2}} \left| n_{\mathbf{q}\lambda} - 1 \right\rangle \quad \text{and} \quad \hat{a}_{\mathbf{q}\lambda}^{\dagger} \left| n_{\mathbf{q}\lambda} \right\rangle = (n_{\mathbf{q}\lambda} + 1)^{\frac{1}{2}} \left| n_{\mathbf{q}\lambda} + 1 \right\rangle. \tag{2.1.12}$$

Here, the operators respectively create and destroy one photon of energy $\hbar\omega_q$ in the mode $\mathbf{q}\lambda$. As such, the number operator, $\hat{n}_{\mathbf{q}\lambda}$, now specifies the number of photons excited in the corresponding cavity mode, such that

$$\hat{n}_{\mathbf{q}\lambda} = \hat{a}_{\mathbf{q}\lambda}^{\dagger} \hat{a}_{\mathbf{q}\lambda}. \tag{2.1.13}$$

The origin of the number operator can be seen in appendix A.1.1. The eigenvalue of the number operator will simply be denoted as $n_{\mathbf{q}\lambda}$, such that

$$\hat{n}_{\mathbf{q}\lambda} \left| n_{\mathbf{q}\lambda} \right\rangle = n_{\mathbf{q}\lambda} \left| n_{\mathbf{q}\lambda} \right\rangle \quad n_{\mathbf{q}\lambda} = 1, 2, ... \tag{2.1.14}$$

The orthonormal eigenstates $\left| n_{\mathbf{q}\lambda} \right\rangle$ are called the *photon-number states* or the *Fock states* of the electromagnetic field [21, ch. 4.4]. To specify a number state of the total electromagnetic field in the cavity, an ordered string containing single-mode photon-number states is used. Different cavity modes are independent, and corresponding associated operators commute. As such, the commutation relations between these become

$$\left[\hat{a}_{\mathbf{q}\lambda}, \hat{a}_{\mathbf{q}'\lambda'}^{\dagger} \right] = \delta_{\mathbf{q},\mathbf{q}'} \delta_{\lambda\lambda'}. \tag{2.1.15}$$

The state of the total field may be expressed in a few different ways, namely

$$\left| n_{\mathbf{q}_1 1}, n_{\mathbf{q}_1 2}, n_{\mathbf{q}_2 1}, n_{\mathbf{q}_2 2}, ... \right\rangle = \left| n_{\mathbf{q}_1 1} \right\rangle \left| n_{\mathbf{q}_1 2} \right\rangle \left| n_{\mathbf{q}_2 1} \right\rangle \left| n_{\mathbf{q}_2 2} \right\rangle ... = \left| \{ n_{\mathbf{q}\lambda} \} \right|, \tag{2.1.16}$$

where $\{n_{\mathbf{q}\lambda}\}$ denotes the complete set of numbers needed to specify all excitation levels of the oscillators corresponding to the different cavity modes. The total number state only forms a complete set for the radiation field when $n_{\mathbf{q}\lambda} \in \{\mathbb{Z}^+, 0\}$ for all $\mathbf{q}$, λ. The Hamiltonian of the total electromagnetic field is then found by summing all the individual oscillator Hamiltonians, that is

$$\hat{\mathcal{H}}_R = \sum_{\mathbf{q}} \sum_{\lambda=1,2} \hat{\mathcal{H}}_{\mathbf{q}\lambda}, \quad \hat{\mathcal{H}}_{\mathbf{q}\lambda} = \frac{1}{2}\hbar\omega_q \left(\hat{a}_{\mathbf{q}\lambda}\hat{a}^\dagger_{\mathbf{q}\lambda} + \hat{a}^\dagger_{\mathbf{q}\lambda}\hat{a}_{\mathbf{q}\lambda}\right). \tag{2.1.17}$$

The single mode Hamiltonian expression here is also seen in equation (A.1.8). Therefore, the energy eigenvalue equation for the multimode number state is clearly

$$\hat{\mathcal{H}}_R \left|\{n_{\mathbf{q}\lambda}\}\right\rangle = \sum_{\mathbf{q}} \sum_{\lambda} \hbar\omega_q \left(\hat{n}_{\mathbf{q}\lambda} + \frac{1}{2}\right) \left|\{n_{\mathbf{q}\lambda}\}\right\rangle. \tag{2.1.18}$$

The ground state of the radiation field is the state in which no photons are excited in any of the field modes. This state is also called the *vacuum state* of the field, and can be expressed formally as

$$n_{\mathbf{q}\lambda} = 0 \quad \forall\, \mathbf{q}, \lambda, \tag{2.1.19}$$

which can be denoted as $|\{0\}\rangle$. The vacuum state condition can be expressed using the destruction operator as

$$\hat{a}_{\mathbf{q}\lambda} \left|\{0\}\right\rangle = 0 \quad \forall\, \mathbf{q}, \lambda. \tag{2.1.20}$$

The energy eigenvalue equation for the vacuum state is then easily seen to be

$$\hat{\mathcal{H}}_R \left|\{0\}\right\rangle = \sum_{\mathbf{q}} \sum_{\lambda} \frac{1}{2}\hbar\omega_q \left|\{0\}\right\rangle \equiv E_0 \left|\{0\}\right\rangle, \tag{2.1.21}$$

where E_0 is called the *vacuum energy*, accordingly. Moreover, the energy eigenvalue equation can be formulated with respect to the vacuum energy and the excitation energy as

$$\hat{\mathcal{H}}_R \left|\{n_{\mathbf{q}\lambda}\}\right\rangle = (E_R + E_0) \left|\{n_{\mathbf{q}\lambda}\}\right\rangle, \tag{2.1.22}$$

where the excitation energy is given as

$$E_R = \sum_{\mathbf{q}} \sum_{\lambda} \hbar\omega_q n_{\mathbf{q}\lambda}. \tag{2.1.23}$$

However, it should be noticed that the frequencies ω_q have no upper bound, which consequently enables the vacuum energy to be infinite. By deriving classically [21, ch. 4.2], it can be shown that the total radiative energy, corresponding to the classical Hamiltonian, is simply a sum of of contributions from different modes on the form

$$E_{\mathbf{q}\lambda} = \varepsilon_0 \Omega \omega_q^2 \left(A_{\mathbf{q}\lambda} A^*_{\mathbf{q}\lambda} + A^*_{\mathbf{q}\lambda} A_{\mathbf{q}\lambda}\right), \tag{2.1.24}$$

where Ω is the volume. $A_{\mathbf{q}\lambda}$ and $A^*_{\mathbf{q}\lambda}$ are the free-space mode coefficients of the electromagnetic potential, which is on the form:

$$\mathbf{A}(\mathbf{r}, t) = \sum_{\mathbf{q}} \sum_{\lambda=1,2} \mathbf{e}_{\mathbf{q}\lambda} \left(A_{\mathbf{q}\lambda} \mathrm{e}^{-i(\omega_q t - \mathbf{q}\cdot\mathbf{r})} + A^*_{\mathbf{q}\lambda} \mathrm{e}^{i(\omega_q t - \mathbf{q}\cdot\mathbf{r})}\right). \tag{2.1.25}$$

Naturally, the classical mode coefficients commute, but when equation (2.1.24) is on the current form, it can be compared to equation (2.1.17). As such, the classical vector-potential modal coefficients can be converted to quantum-mechanical operators by substituting

$$A_{\mathbf{q}\lambda} \to \left(\frac{\hbar}{2\varepsilon_0 \Omega \omega_q}\right)^{\frac{1}{2}} \hat{a}_{\mathbf{q}\lambda}, \qquad A^*_{\mathbf{q}\lambda} \to \left(\frac{\hbar}{2\varepsilon_0 \Omega \omega_q}\right)^{\frac{1}{2}} \hat{a}^\dagger_{\mathbf{q}\lambda}. \tag{2.1.26}$$

Effectively, this converts the classical vector-potential to an operator on the form:

$$\hat{\mathbf{A}}(\mathbf{r},t)=\sum_{\mathbf{q}}\sum_{\lambda=1,2}\mathbf{e}_{\mathbf{q}\lambda}\hat{A}_{\mathbf{q}\lambda}(\mathbf{r},t), \tag{2.1.27}$$

where

$$\hat{A}_{\mathbf{q}\lambda}(\mathbf{r},t)=\left(\frac{\hbar}{2\varepsilon_0\Omega\omega_q}\right)^{\frac{1}{2}}\left\{\hat{a}_{\mathbf{q}\lambda}\mathrm{e}^{-i(\omega_q t-\mathbf{q}\cdot\mathbf{r})}+\hat{a}^{\dagger}_{\mathbf{q}\lambda}\mathrm{e}^{i(\omega_q t-\mathbf{q}\cdot\mathbf{r})}\right\}. \tag{2.1.28}$$

This quantised free-space field will be important in section 2.3.4.

2.2 Linear Perturbation Theory

To measure the properties of a system, it is necessary to understand the response of the system when an external perturbation is applied. The external perturbation could be an electromagnetic perturbation, such as light. If this perturbation is small, the response of the system can be approximated to be linear in field strength. Consider now an unperturbed ground state system, which can be described by a time-independent Hamiltonian, $\hat{H}_0$. The ground state wave function can be approximated as a Slater determinant, where the orbitals are given by the Schrödinger equation,

$$\hat{H}_0\varphi_n=E_n^0\varphi_n. \tag{2.2.1}$$

Here E_n^0 is the n'th eigenvalue and φ_n is the n'th stationary eigenfunction of the ground state, which only depends on spatial coordinates. By introducing a perturbation, the electron state will be excited. Instead of finding a completely new Hamiltonian for this exited state, the excited Hamiltonian can be written as a sum of the unperturbed and interaction Hamiltonian:

$$\hat{H}=\hat{H}_0+\hat{H}'. \tag{2.2.2}$$

By assuming the response of the perturbation to be characterised by a single frequency ω and only including first order terms of the interaction Hamiltonian, the time-dependent Schrödinger equation becomes:

$$i\hbar\frac{\partial\psi}{\partial t}=\left\{\hat{H}_0+\frac{1}{2}\hat{H}_1\mathrm{e}^{-i\omega t}+\frac{1}{2}\hat{H}_1^{\dagger}\mathrm{e}^{i\omega t}\right\}\psi, \tag{2.2.3}$$

where $\hat{H}_1$ contains the spatial part of the perturbation. The total perturbed wave function can be written as a sum of each time-independent wave function, φ_n, as

$$\psi=\sum_n a_n\varphi_n\mathrm{e}^{-i\frac{E_n t}{\hbar}}, \tag{2.2.4}$$

where a_n is a time-dependent coefficient. Since the response to the external perturbation is assumed linear, the interaction Hamiltonian must therefore be linearly dependent on the field strength. Hence, a_n must also be dependent of the field strength, $\boldsymbol{\varepsilon}$, meaning $a_n=a_n(\boldsymbol{\varepsilon})$ for the electric case. Consequently, this allows a_n to be Taylor expanded with regard to the field strength, i.e.

$$a_n=a_n^{(0)}+a_n^{(1)}+a_n^{(2)}+..., \tag{2.2.5}$$

From this, it can be shown that the induced response due to a perturbation can be found using [22]:

$$X(\omega)=-\sum_{m,n}f_{nm}\frac{\langle\varphi_m|\hat{H}_1|\varphi_n\rangle\langle\varphi_n|\hat{X}|\varphi_m\rangle}{E_{mn}-\hbar\omega-i\hbar\Gamma}, \tag{2.2.6}$$

where $X(\omega)$ is the response, $\hat{X}$ is the corresponding operator, $E_{mn} = E_m - E_n$ is difference in energy levels, and $f_{nm} \equiv f(E_n) - f(E_m)$ is the corresponding difference in distribution functions. Thus, this derived expression is the first order time-dependent induced response due to some perturbation. It also shows that knowing the interaction Hamiltonian and the induced response operator, one can find the time-dependent induced response of the system.

2.3 Models of Excitons - The Bethe-Salpeter Equation

The aim of this chapter is to do accurate calculations on a many-electron system. In particular, the focus will be many-body excited states, referred to as excitons. To start off, the all-electron wave function will be approximated by Slater determinants, which is done by applying the single-particle approximation. By disallowing spin-hybridisation, due to spin-orbit interactions, between the conduction and valence bands, the ground state can be approximated with the Slater determinant

$$|0\rangle = |(v_1 \uparrow), (v_1 \downarrow), ..., (v_N \uparrow), (v_N \downarrow)| \,. \tag{2.3.1}$$

This is a good approximation for semiconductors due to the energy difference between these bands. As such, for every state n, there are four excitations due to spin, namely

$$\begin{aligned}
|(v_i \uparrow) \to (c_j \uparrow)\rangle &:= |(v_1 \uparrow), (v_1 \downarrow), ...(v_i \downarrow), (c_j \uparrow)..., (v_N \uparrow), (v_N \downarrow)| \,, && (2.3.2)\\
|(v_i \downarrow) \to (c_j \uparrow)\rangle &:= |(v_1 \uparrow), (v_1 \downarrow), ...(c_j \uparrow), (v_i \uparrow)..., (v_N \uparrow), (v_N \downarrow)| \,, && (2.3.3)\\
|(v_i \uparrow) \to (c_j \downarrow)\rangle &:= |(v_1 \uparrow), (v_1 \downarrow), ...(v_i \downarrow), (c_j \downarrow)..., (v_N \uparrow), (v_N \downarrow)| \,, && (2.3.4)\\
|(v_i \downarrow) \to (c_j \downarrow)\rangle &:= |(v_1 \uparrow), (v_1 \downarrow), ...(c_j \downarrow), (v_i \uparrow)..., (v_N \uparrow), (v_N \downarrow)| \,. && (2.3.5)
\end{aligned}$$

Writing this in vector notation as a spinor

$$|v_i \to c_j\rangle := \begin{bmatrix} |(v_i \uparrow) \to (c_j \uparrow)\rangle \\ |(v_i \downarrow) \to (c_j \uparrow)\rangle \\ |(v_i \uparrow) \to (c_j \downarrow)\rangle \\ |(v_i \downarrow) \to (c_j \downarrow)\rangle \end{bmatrix} . \tag{2.3.6}$$

Now, the excited states will be written as a linear combination of the excitations on the form of equation (2.3.6):

$$|exc\rangle = \sum_{ij} \mathbf{\Psi}_{ij} \cdot |v_i \to c_j\rangle \,, \tag{2.3.7}$$

where $\mathbf{\Psi}_{ij}$ are expansion factors, given as a vector to match the spinor. The main problem is now to find the matrix elements of the Hamiltonian super-matrix between two arbitrary states, written as

$$\overline{\mathbf{H}}_{ij}^{kl} = \left\langle v_i \to c_j \middle| \hat{H} \middle| v_k \to c_l \right\rangle , \tag{2.3.8}$$

where

$$\hat{H} = \sum_{\sigma} \sum_{n=1}^{N} \hat{h}_{n\sigma} + \sum_{\sigma,\sigma'} \sum_{n<n'}^{N} V\left(\mathbf{r}_{n\sigma} - \mathbf{r}_{n'\sigma'}\right) , \tag{2.3.9}$$

and $\hat{h}_{n\sigma}$ is the single-electron Hamiltonian, including spin-orbit coupling. The first step is to analyse the ground state energy, which, using the rules for overlap of Slater determinants [23, ch. 16.3], can be written as

$$\begin{aligned}\left\langle 0 \middle| \hat{H} \middle| 0 \right\rangle = &\sum_{m_s \in \{\uparrow,\downarrow\}} \sum_{n=1}^{N} \left\langle v_n m_s \middle| \hat{h} + \hat{h}_{SO} \middle| v_n m_s \right\rangle \\ &+ \frac{1}{2} \sum_{m_s, m_s'}^{2} \sum_{n,n'}^{N} \left\{ \langle v_n m_s, v_{n'} m_s' \,|\, V \,|\, v_n m_s, v_{n'} m_s' \rangle - \langle v_n m_s, v_{n'} m_s' \,|\, V \,|\, v_{n'} m_s', v_n m_s \rangle \right\},\end{aligned} \tag{2.3.10}$$

where the quantum number m_s is the secondary spin quantum number, $\hat{h}$ is the single-electron Hamiltonian without spin-orbit coupling, and $\hat{h}_{SO}$ is the spin-orbit interaction. The next step is to look at the elements of the super-matrix $\overline{\mathbf{H}}$. This can be done fairly simply by using the rules for matrix element between Slater determinants, mainly rules regarding single-electron operators and two-electron operators [23, ch. 16.3]. In particular, there are fourteen non-zero elements of the matrix $\overline{\mathbf{H}}_{ij}^{kl}$. Setting $s \neq s'$, the diagonal elements are either:
Zero total spin:

$$\begin{aligned}&\left\langle (v_i m_s) \to (c_j m_s) \middle| \hat{H} \middle| (v_k m_s) \to (c_l m_s) \right\rangle = \left\langle 0 \middle| \hat{H} \middle| 0 \right\rangle \delta_{jl} \delta_{ik} \\ &+ \sum_{m_s'' \in \{\uparrow,\downarrow\}} \sum_{n} \left\{ \langle v_n m_s'', c_j m_s \,|\, V \,|\, v_n m_s'', c_l m_s \rangle - \langle v_n m_s'', c_j m_s \,|\, V \,|\, c_l m_s, v_n m_s'' \rangle \right\} \delta_{ik} \\ &- \sum_{m_s'' \in \{\uparrow,\downarrow\}} \sum_{n} \left\{ \langle v_n m_s'', v_k m_s \,|\, V \,|\, v_n m_s'', v_i m_s \rangle - \langle v_n m_s'', v_k m_s \,|\, V \,|\, v_i m_s, v_n m_s'' \rangle \right\} \delta_{jl} \\ &+ \left\langle c_j m_s \middle| \hat{h} + \hat{h}_{SO} \middle| c_l m_s \right\rangle \delta_{ik} - \left\langle v_k m_s \middle| \hat{h} + \hat{h}_{SO} \middle| v_i m_s \right\rangle \delta_{jl} \\ &- \langle v_k m_s, c_j m_s \,|\, V \,|\, v_i m_s, c_l m_s \rangle + \langle v_k m_s, c_j m_s \,|\, V \,|\, c_l m_s, v_i m_s \rangle .\end{aligned} \tag{2.3.11}$$

±1 total spin:

$$\begin{aligned}&\left\langle (v_i m_s) \to (c_j m_s') \middle| \hat{H} \middle| (v_k m_s) \to (c_l m_s') \right\rangle = \left\langle 0 \middle| \hat{H} \middle| 0 \right\rangle \delta_{jl} \delta_{ik} \\ &+ \sum_{m_s'' \in \{\uparrow,\downarrow\}} \sum_{n} \left\{ \langle v_n m_s'', c_j m_s' \,|\, V \,|\, v_n m_s'', c_l m_s' \rangle - \langle v_n m_s'', c_j m_s' \,|\, V \,|\, c_l m_s', v_n m_s'' \rangle \right\} \delta_{ik} \\ &- \sum_{m_s'' \in \{\uparrow,\downarrow\}} \sum_{n} \left\{ \langle v_n m_s'', v_k m_s \,|\, V \,|\, v_n m_s'', v_i m_s \rangle - \langle v_n m_s'', v_k m_s \,|\, V \,|\, v_i m_s, v_n m_s'' \rangle \right\} \delta_{jl} \\ &+ \left\langle c_j m_s' \middle| \hat{h} + \hat{h}_{SO} \middle| c_l m_s' \right\rangle \delta_{ik} - \left\langle v_k m_s \middle| \hat{h} + \hat{h}_{SO} \middle| v_i m_s \right\rangle \delta_{jl} \\ &- \langle v_k m_s, c_j m_s' \,|\, V \,|\, v_i m_s, c_l m_s' \rangle .\end{aligned} \tag{2.3.12}$$

These can be significantly simplified by introducing the quasi-particle energies,

$$\begin{aligned}\tilde{E}_{c_j m_s}^{c_l m_s} := &\left\langle c_j m_s \middle| \hat{h} \middle| c_l m_s \right\rangle + \sum_{m_s'' \in \{\uparrow,\downarrow\}} \sum_{n=1}^{N} \left\{ \langle v_n m_s'', c_j m_s \,|\, V \,|\, v_n m_s'', c_l m_s \rangle \right. \\ &\left. - \langle v_n m_s'', c_j m_s \,|\, V \,|\, c_l m_s, v_n m_s'' \rangle \right\},\end{aligned} \tag{2.3.13}$$

$$\begin{aligned}\tilde{E}_{v_k m_s}^{v_i m_s} := &\left\langle v_k m_s \middle| \hat{h} \middle| v_i m_s \right\rangle + \sum_{m_s'' \in \{\uparrow,\downarrow\}} \sum_{n=1}^{N} \left\{ \langle v_n m_s'', v_k m_s \,|\, V \,|\, v_n m_s'', v_i m_s \rangle \right. \\ &\left. - \langle v_n m_s'', v_k m_s \,|\, V \,|\, v_i m_s, v_n m_s'' \rangle \right\}.\end{aligned} \tag{2.3.14}$$

However, due to these energies being the eigenstates of the underlying electronic system without spin-orbit coupling, they must be orthogonal. Thus, by insertion and using the orthogonality, these then give

$$\begin{aligned}\left\langle (v_i m_s) \to (c_j m_s) \,\middle|\, \hat{H} \,\middle|\, (v_k m_s) \to (c_l m_s) \right\rangle &= \left(\left\langle 0 \,\middle|\, \hat{H} \,\middle|\, 0 \right\rangle + \tilde{E}_{c_j m_s} - \tilde{E}_{v_i m_s} \right) \delta_{ik} \delta_{jl} \\ &- \langle v_k m_s, c_j m_s \,|\, V \,|\, v_i m_s, c_l m_s \rangle + \langle v_k m_s, c_j m_s \,|\, V \,|\, c_l m_s, v_i m_s \rangle \\ &+ \left\langle c_j m_s \,\middle|\, \hat{h}_{SO} \,\middle|\, c_l m_s \right\rangle \delta_{ik} - \left\langle v_k m_s \,\middle|\, \hat{h}_{SO} \,\middle|\, v_i m_s \right\rangle \delta_{jl},\end{aligned} \tag{2.3.15}$$

and

$$\begin{aligned}\left\langle (v_i m_s) \to (c_j m_s') \,\middle|\, \hat{H} \,\middle|\, (v_k m_s) \to (c_l m_s') \right\rangle &= \left(\left\langle 0 \,\middle|\, \hat{H} \,\middle|\, 0 \right\rangle + \tilde{E}_{c_j m_s'} - \tilde{E}_{v_i m_s} \right) \delta_{ik} \delta_{jl} \\ - \langle v_k m_s, c_j m_s' \,|\, V \,|\, v_i m_s, c_l m_s' \rangle &+ \left\langle c_j m_s' \,\middle|\, \hat{h} + \hat{h}_{SO} \,\middle|\, c_l m_s' \right\rangle \delta_{ik} - \left\langle v_k m_s \,\middle|\, \hat{h} + \hat{h}_{SO} \,\middle|\, v_i m_s \right\rangle \delta_{jl},\end{aligned} \tag{2.3.16}$$

respectively. The ground state energy $\langle 0|\hat{H}|0\rangle$ appears in all diagonal term of the matrix, and can thus be set equal to zero by defining it as zero-point of energy. The off-diagonal terms of $\overline{\mathbf{H}}_{ij}^{kl}$ are:

Zero total spin, off-diagonal:

$$\left\langle (v_i m_s) \to (c_j m_s) \,\middle|\, \hat{H} \,\middle|\, (v_k m_s') \to (c_l m_s') \right\rangle = \left\langle v_k m_s', c_j m_s \,\middle|\, V \,\middle|\, c_l m_s', v_i m_s \right\rangle. \tag{2.3.17}$$

Zero total spin to ±1 total spin, I:

$$\left\langle (v_i m_s) \to (c_j m_s) \,\middle|\, \hat{H} \,\middle|\, (v_k m_s') \to (c_l m_s) \right\rangle = - \left\langle v_k m_s' \,\middle|\, \hat{h}_{SO} \,\middle|\, v_i m_s \right\rangle =: -\zeta_{v_k m_s', v_i m_s}. \tag{2.3.18}$$

Zero total spin to ±1 total spin, II:

$$\left\langle (v_i m_s) \to (c_j m_s) \,\middle|\, \hat{H} \,\middle|\, (v_k m_s) \to (c_l m_s') \right\rangle = \left\langle c_j m_s \,\middle|\, \hat{h}_{SO} \,\middle|\, c_l m_s' \right\rangle =: \zeta_{c_j m_s, c_l m_s'}. \tag{2.3.19}$$

Now, the following quantities may be defined, namely

$$K_{n m_s, n' m_s'}^{n'' m_s'', n''' m_s'''} := \left\langle n m_s, n' m_s' \,\middle|\, V \,\middle|\, n'' m_s'', n''' m_s''' \right\rangle, \tag{2.3.20}$$

$$\zeta_{n m_s, n' m_s'}^{n'' m_s'', n''' m_s'''} := \zeta_{n m_s, n'' m_s''} \delta_{n', n'''} \delta_{s', s'''}, \tag{2.3.21}$$

$$\begin{aligned}E_{n m_s, n' m_s'}^{n'' m_s'', n''' m_s'''} := \Bigg[&\left(\tilde{E}_{n' m_s'}^{n''' m_s'''} - \tilde{E}_{n m_s}^{n'' m_s''} \right) \delta_{n,n''} \delta_{n',n'''} \\ &- \left\langle n' m_s' \,\middle|\, \hat{h}_{SO} \,\middle|\, n''' m_s''' \right\rangle \delta_{n,n''} + \left\langle n m_s \,\middle|\, \hat{h}_{SO} \,\middle|\, n'' m_s'' \right\rangle \delta_{n',n'''} \Bigg] \delta_{s,s''}, \delta_{s',s'''}.\end{aligned} \tag{2.3.22}$$

This allows for writing the super-matrix element as

$$\overline{\mathbf{H}}_{ij}^{kl} = \begin{bmatrix} E_{v_k\uparrow,c_j\uparrow}^{v_i\uparrow,c_l\uparrow} - K_{v_k\uparrow,c_j\uparrow}^{v_i\uparrow,c_l\uparrow} + K_{v_k\uparrow,c_j\uparrow}^{c_l\uparrow,v_i\uparrow} & -\zeta_{v_k\downarrow,c_j\uparrow}^{v_i\uparrow,c_l\uparrow} & \zeta_{c_j\uparrow,v_k\uparrow}^{c_l\downarrow,v_i\uparrow} & K_{v_k\uparrow,c_j\downarrow}^{c_l\uparrow,v_i\downarrow} \\ -\zeta_{v_k\uparrow,c_j\uparrow}^{v_i\downarrow,c_l\uparrow} & E_{v_k\uparrow,c_j\downarrow}^{v_i\uparrow,c_l\downarrow} - K_{v_k\uparrow,c_j\downarrow}^{v_i\uparrow,c_l\downarrow} & 0 & \zeta_{c_j\uparrow,v_k\downarrow}^{c_l\downarrow,v_i\downarrow} \\ \zeta_{c_j\downarrow,v_k\uparrow}^{c_l\uparrow,v_i\uparrow} & 0 & E_{v_k\downarrow,c_j\uparrow}^{v_i\downarrow,c_l\uparrow} - K_{v_k\downarrow,c_j\uparrow}^{v_i\downarrow,c_l\uparrow} & -\zeta_{v_k\downarrow,c_j\downarrow}^{v_i\uparrow,c_l\downarrow} \\ K_{v_k\downarrow,c_j\uparrow}^{c_l\downarrow,v_i\uparrow} & \zeta_{c_j\downarrow,v_k\downarrow}^{c_l\uparrow,v_i\downarrow} & -\zeta_{v_k\uparrow,c_j\downarrow}^{v_i\downarrow,c_l\downarrow} & E_{v_k\downarrow,c_j\downarrow}^{v_i\downarrow,c_l\downarrow} - K_{v_k\downarrow,c_j\downarrow}^{v_i\downarrow,c_l\downarrow} + K_{v_k\downarrow,c_j\downarrow}^{c_l\downarrow,v_i\downarrow} \end{bmatrix}. \tag{2.3.23}$$

The super-matrix eigenvalue problem now reads as

$$\sum_{kl} \overline{\mathbf{H}}_{ij}^{kl} \mathbf{\Psi}_{kl} = E_{exc} \mathbf{\Psi}_{ij}. \tag{2.3.24}$$

This is the general unscreened Bethe-Salpeter equation derived from Slater determinants with spin-orbit interaction included.

2.3.1 Excitons in Periodic Solids with Screening

This section shall specialize in the case of a periodic solid, where the orbitals are labeled by a band index and wave vector $\mathbf{k}$. Thus, the spinor states which will be analysed are the type $|v\mathbf{k} \rightarrow c\mathbf{k}'\rangle$. The process to derive these Hamiltonian matrix elements is the same as before, however, the Coulomb interaction will be screened by surrounding charges. Thus, the Coulomb potential should be replaced by a screened potential, W: [24]

$$\left\langle vm_s\mathbf{k}, cm_s'\mathbf{k}' \,\middle|\, V \,\middle|\, v'm_s\mathbf{k}, c'm_s'\mathbf{k}'\right\rangle \rightarrow \left\langle vm_s\mathbf{k}, cm_s'\mathbf{k}' \,\middle|\, W \,\middle|\, v'm_s\mathbf{k}, c'm_s'\mathbf{k}'\right\rangle . \tag{2.3.25}$$

The full matrix equation, where the screened Coulomb interaction is used, is called the screened Bethe-Salpeter equation for solids, and will be given the acronym BSE. Another thing to note is that for states of different $\mathbf{k}$, the SO overlaps will be $\zeta^{c'k'\sigma'',v'k'\sigma'''}_{ck\sigma,vk\sigma'} = 0$.

The screening interaction can be seen in figure 2.3.1, where a homogeneous layer with thickness d and dielectric constant ε, is placed between materials with dielectric constants ε_a and ε_b. The charges in the middle layer will be screened by the layer itself, but also by the charges in the surrounding sub- and superstrate. One can interpret the charges interaction through field-lines connecting the charges. The lines should be understood as, if the charges are far from one another the field line will mainly penetrate the surrounding dielectrics, meaning these will mainly contribute to the screening and vice versa.

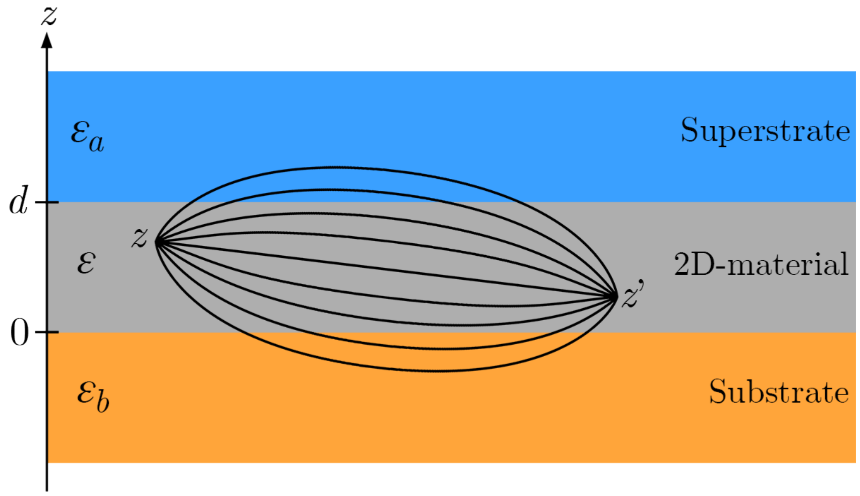

Figure 2.3.1: An encapsulated 2D material, where the charges in the material will affect one another through a screened Coulomb interaction.

As a starting point one should consider Gauss' law in differential form [22]

$$\nabla \cdot \mathbf{D}(\mathbf{r}) = e^2 \delta\left(\mathbf{r} - \mathbf{r}'\right) . \tag{2.3.26}$$

Since $\mathbf{D}(\mathbf{r}) = \varepsilon_0 \varepsilon(\mathbf{r}) \mathbf{E}(\mathbf{r})$ and the electric field is related through the potential as $\mathbf{E}(\mathbf{r}) = -\nabla V(\mathbf{r})$, one can obtain:

$$\nabla \cdot \left[\varepsilon(\mathbf{r}) \left(-\nabla V(\mathbf{r})\right)\right] = \frac{e^2}{\varepsilon_0} \delta\left(\mathbf{r} - \mathbf{r}'\right) . \tag{2.3.27}$$

Consider now the real-space potential written in terms of the 2D Fourier transform, that is

$$V(\boldsymbol{\rho}, z, z') = \frac{1}{4\pi^2} \int v(z, z'; \kappa) \mathrm{e}^{i\boldsymbol{\kappa}\cdot\boldsymbol{\rho}} d^2\kappa, \tag{2.3.28}$$

where $\hbar\boldsymbol{\kappa}$ is the in-plane momentum and $\boldsymbol{\rho}$ is the in-plane separation. In the considered geometry, $\varepsilon(\mathbf{r}) = \varepsilon(z)$. Now, by inserting this Fourier transform into equation (2.3.27) and inverse Fourier transforming both sides, one will obtain

$$\left(\kappa^2\varepsilon(z) - \frac{d}{dz}\varepsilon(z)\frac{d}{dz}\right) v(z, z'; \kappa) = \frac{e^2}{\varepsilon_0}\delta\left(z - z'\right). \tag{2.3.29}$$

If z' is in the 2D layer, the equation can be solved by standard ansatz [22]:

$$v(z, z'; \kappa) = \frac{e^2}{2\varepsilon_0\kappa}\begin{cases} C\mathrm{e}^{-\kappa|z-z'|} & z > d \\ \dfrac{1}{\varepsilon}\mathrm{e}^{-\kappa|z-z'|} + A\mathrm{e}^{-\kappa|z+z'|} + B\mathrm{e}^{-\kappa|2d-z-z'|} & 0 \leqslant z \leqslant d \\ D\mathrm{e}^{-\kappa|z-z'|} & z < d \end{cases}. \tag{2.3.30}$$

To solve the equation with these ansatz, appropriate boundary conditions have to be applied. The potential and the normal component of $\mathbf{D}$ should be continuous, which can be expressed as

$$\begin{aligned} v(z^+, z'; \kappa) &= v(z^-, z'; \kappa), \\ \varepsilon^+\frac{d}{dz}v(z^+, z'; \kappa) &= \varepsilon^-\frac{d}{dz}v(z^-, z'; \kappa). \end{aligned} \tag{2.3.31}$$

Using these boundary conditions, one can isolate for each unknown coefficient, and obtain an expression for the full potential in the desired layer [22],

$$v(z, z'; \kappa) = \frac{e^2\mathrm{e}^{-\kappa|z+z'|}}{2\kappa\varepsilon\varepsilon_0}\cdot\frac{\left(\varepsilon - \varepsilon_b + (\varepsilon + \varepsilon_b)\,\mathrm{e}^{2\kappa z_<}\right)\left(\varepsilon + \varepsilon_a + (\varepsilon - \varepsilon_a)\,\mathrm{e}^{2\kappa(z_> - d)}\right)}{(\varepsilon + \varepsilon_b)(\varepsilon + \varepsilon_a) - (\varepsilon - \varepsilon_b)(\varepsilon - \varepsilon_a)\mathrm{e}^{-2\kappa d}}, \tag{2.3.32}$$

where $z_< = \min\{z, z'\}$ and $z_> = \max\{z, z'\}$. Now, setting $z = z' = d/2$ will reduce equation (2.3.32) to

$$v(d/2, d/2; \kappa) = \frac{e^2}{2\kappa\varepsilon_0\,\varepsilon_{eff}(\kappa)}, \tag{2.3.33}$$

where

$$\varepsilon_{eff}(\kappa) = \varepsilon\left(1 - \frac{\varepsilon - \varepsilon_a}{\varepsilon - \varepsilon_a + (\varepsilon + \varepsilon_a)\mathrm{e}^{\kappa d}} - \frac{\varepsilon - \varepsilon_b}{\varepsilon - \varepsilon_b + (\varepsilon + \varepsilon_b)\mathrm{e}^{\kappa d}}\right). \tag{2.3.34}$$

It can be seen that the screening effect arises from ε_{eff}, since if all the layers are the same material meaning, $\varepsilon_a = \varepsilon_b = \varepsilon$ then $\varepsilon_{eff} = \varepsilon$. Expanding equation (2.3.34) to first order around $d = 0$ will yield

$$\varepsilon_{eff}(\kappa) \approx \frac{\varepsilon_a + \varepsilon_b}{2} + \left(\frac{\varepsilon - 1}{2} - \frac{\varepsilon_a^2 + \varepsilon_b^2 - 2\varepsilon}{4\varepsilon}\right)\kappa d. \tag{2.3.35}$$

Here the first term is the average sub- and superstrate dielectric constant and the second term in front of κ is called the screening length. Usually this is written as the *Keldysh potential* $\varepsilon_{eff} = \overline{\varepsilon} + r_0\kappa$, where

$$r_0 = \left(\frac{\varepsilon - 1}{2} - \frac{\varepsilon_a^2 + \varepsilon_b^2 - 2\varepsilon}{4\varepsilon}\right)d, \quad \overline{\varepsilon} = \frac{\varepsilon_a + \varepsilon_b}{2}. \tag{2.3.36}$$

2.3.2 Current Density Operator

In order to describe a many-electron system perturbed by an electromagnetic field, the Hamiltonian should undergo a minimal substitution, that is $\hat{\mathbf{p}}_n \to \hat{\mathbf{p}}_n + e\mathbf{A}(\mathbf{r}_n, t)$ for all electron coordinates, n. The Hamiltonian will then be on the form

$$\hat{\mathcal{H}} = \frac{1}{2m}\sum_n\left\{\hat{\mathbf{p}}_n^2 + e\hat{\mathbf{p}}_n\cdot\mathbf{A}(\mathbf{r}_n, t) + e\mathbf{A}(\mathbf{r}_n, t)\cdot\hat{\mathbf{p}}_n + e^2[\mathbf{A}(\mathbf{r}_n, t)]^2\right\} + \sum_{n,m}\hat{U}(\mathbf{r}_n, \mathbf{r}_m), \tag{2.3.37}$$

where the last term represents the potential energy of the system. Using a monochromatic field, the vector-potential can be written as

$$\mathbf{A}(\mathbf{r}_n, t) = \frac{1}{2}\big(\mathbf{A}(\mathbf{r}_n)\mathrm{e}^{-i\omega t} + \mathbf{A}^*(\mathbf{r}_n)\mathrm{e}^{i\omega t}\big), \tag{2.3.38}$$

which shows that $\mathbf{A}(\mathbf{r}_n, t)$ is real, and agrees with equation (2.2.3). Consider the continuity equation

$$-\nabla\cdot\mathbf{J}(\mathbf{r}, t) = e\frac{\partial}{\partial t}\rho(\mathbf{r}, t), \tag{2.3.39}$$

where $\rho(\mathbf{r})$ denotes the charge density. The eigenfunctions of equation (2.3.37) can be approximated as Slater determinants, that is

$$\psi(\mathbf{r}_1, \dots, \mathbf{r}_N, t) = |\varphi_1, \dots, \varphi_N| = \frac{1}{\sqrt{N}}\begin{vmatrix} \varphi_1(\mathbf{r}_1) & \dots & \varphi_N(\mathbf{r}_1) \\ \vdots & \ddots & \vdots \\ \varphi_1(\mathbf{r}_N) & \dots & \varphi_N(\mathbf{r}_N) \end{vmatrix}. \tag{2.3.40}$$

For such Slater determinants the charge density is found as

$$\rho(\mathbf{r}, t) = e\sum_n |\varphi_n(\mathbf{r}, t)|^2. \tag{2.3.41}$$

Next, the continuity equation can be revisited. To simplify it, denote the temporal derivative of ψ as $\dot\psi$, which means that $i\hbar\dot\psi = \hat{\mathcal{H}}\psi$. This also implies that $i\hbar\dot\varphi_n = \hat{\mathcal{H}}_n\varphi_n$. Therefore

$$-\nabla\cdot\mathbf{J}(\mathbf{r}, t) = \frac{e}{i\hbar}\sum_n\left\{\varphi_n^*\hat{\mathcal{H}}_n\varphi_n - \varphi_n\hat{\mathcal{H}}_n^*\varphi_n^*\right\} \tag{2.3.42}$$

$$= \frac{e}{2m}\frac{1}{i\hbar}\sum_n\left\{\varphi_n^*\left[\hat{\mathbf{p}}^2 + e\hat{\mathbf{p}}\cdot\mathbf{A}(\mathbf{r}, t) + e\mathbf{A}(\mathbf{r}, t)\cdot\hat{\mathbf{p}}\right]\varphi_n - c.c.\right\}, \tag{2.3.43}$$

where *c.c.* denotes the complex conjugate. Notice, that $\hat{U}$ was assumed real and therefore could be cancelled. Moreover, the squared terms were also cancelled. From here the expression can be divided into a "momentum" part and a "gauge part", that is

$$-\nabla\cdot\mathbf{J} = (-\nabla\cdot\mathbf{J})_p + (-\nabla\cdot\mathbf{J})_A. \tag{2.3.44}$$

For the momentum part, denoted p, the expression is

$$(-\nabla\cdot\mathbf{J})_p = \frac{e}{2m}\frac{1}{i\hbar}\sum_n\left\{\varphi_n^*(\hat{\mathbf{p}}^2\varphi_n) - \varphi_n(\hat{\mathbf{p}}^2\varphi_n)^*\right\} \tag{2.3.45}$$

$$= \nabla\cdot\frac{ie\hbar}{2m}\sum_n\left\{\varphi_n^*\nabla\varphi_n - \varphi_n\nabla\varphi_n^*\right\}. \tag{2.3.46}$$

This means that the momentum current density, denoted $\mathbf{J}_p$, can be found as

$$\mathbf{J}_p(\mathbf{r}) = -\frac{ie\hbar}{2m}\sum_n\left\{\varphi_n^*\nabla\varphi_n - \varphi_n\nabla\varphi_n^*\right\}. \tag{2.3.47}$$

The gauge part in equation (2.3.44) arises from the cross terms and clearly must be

$$(-\nabla\cdot\mathbf{J})_A = -\frac{e^2}{2m}\sum_n\left\{\varphi_n^*\left(\nabla\cdot\mathbf{A} + \mathbf{A}\cdot\nabla\right)\varphi_n + \varphi_n\left(\nabla\cdot\mathbf{A} + \mathbf{A}\cdot\nabla\right)\varphi_n^*\right\}. \tag{2.3.48}$$

If the Coulomb gauge is assumed, then $\nabla \cdot \mathbf{A} = 0$, which reduces the expression to

$$(-\nabla \cdot \mathbf{J})_A = -\frac{e^2}{m} \sum_n \{\varphi_n^* \mathbf{A} \cdot \nabla \varphi_n + \varphi_n \mathbf{A} \cdot \nabla \varphi_n^*\}. \tag{2.3.49}$$

Thus, the gauge current density can be expressed as

$$\mathbf{J}_A(\mathbf{r}, t) = \frac{e^2}{m} \sum_n \varphi_n^* \varphi_n \mathbf{A}(\mathbf{r}, t). \tag{2.3.50}$$

Moreover, since $\mathbf{J}_A(\mathbf{r}, t)$ is induced by $\mathbf{A}(\mathbf{r}, t)$, it should be on a similar form, that is

$$\mathbf{J}_A(\mathbf{r}, t) = \frac{1}{2}\big(\mathbf{J}_A(\mathbf{r})\mathrm{e}^{-i\omega t} + \mathbf{J}_A^*(\mathbf{r})\mathrm{e}^{i\omega t}\big). \tag{2.3.51}$$

This clearly shows equation (2.3.50) still holds true, if the temporal dependency is ignored. In conclusion, the total current density can be written as

$$\mathbf{J}(\mathbf{r}) = \mathbf{J}_p(\mathbf{r}) + \mathbf{J}_A(\mathbf{r}) = \frac{e}{2m} \sum_n (\varphi_n^* \hat{\mathbf{p}} \varphi_n - \varphi_n \hat{\mathbf{p}} \varphi_n^* + 2e \varphi_n^* \mathbf{A}(\mathbf{r}) \varphi_n). \tag{2.3.52}$$

Now, the current density operator $\hat{\mathbf{J}}$ should fulfill

$$\mathbf{J}(\mathbf{r}) = \int \psi^*(\mathbf{r}_1, \ldots, \mathbf{r}_N) \hat{\mathbf{J}}(\mathbf{r}; \mathbf{r}_1, \ldots, \mathbf{r}_N) \psi(\mathbf{r}_1, \ldots, \mathbf{r}_N) d\mathbf{r}_1 \ldots d\mathbf{r}_N \tag{2.3.53}$$

$$= \frac{e}{2m} \sum_n (\varphi_n^* \hat{\mathbf{p}} \varphi_n - \varphi_n \hat{\mathbf{p}} \varphi_n^* + 2e \varphi_n^* \mathbf{A}(\mathbf{r}) \varphi_n). \tag{2.3.54}$$

This equality can be shown to hold true, if $\hat{\mathbf{J}}(\mathbf{r}; \mathbf{r}_1, \ldots, \mathbf{r}_N)$ takes the form

$$\hat{\mathbf{J}}(\mathbf{r}; \mathbf{r}_1, \ldots, \mathbf{r}_N) = \frac{e}{2m} \sum_n \{\delta(\mathbf{r} - \mathbf{r}_n) \hat{\mathbf{p}}_n + \hat{\mathbf{p}}_n \delta(\mathbf{r} - \mathbf{r}_n) + 2\mathbf{A}(\mathbf{r}_n) \delta(\mathbf{r} - \mathbf{r}_n)\}. \tag{2.3.55}$$

Due to Slater selection rules for sums of one electron operators [23, ch. 16], equation (2.3.53) reduces to

$$\mathbf{J}(\mathbf{r}) = \frac{e}{2m} \sum_n \int \varphi_n^*(\mathbf{r}_n) \Big\{\delta(\mathbf{r} - \mathbf{r}_n) \hat{\mathbf{p}}_n + \hat{\mathbf{p}}_n \delta(\mathbf{r} - \mathbf{r}_n) + 2\mathbf{A}(\mathbf{r}_n) \delta(\mathbf{r} - \mathbf{r}_n)\Big\} \varphi_n(\mathbf{r}_n) d\mathbf{r}_n. \tag{2.3.56}$$

The first and third terms on the RHS of equation (2.3.56) clearly provide the corresponding terms on the RHS in equation (2.3.54). To see that this holds true for the second term as well, consider

$$\begin{aligned} &\int \varphi_n^*(\mathbf{r}') \nabla_{\mathbf{r}'} \delta(\mathbf{r} - \mathbf{r}') \varphi_n(\mathbf{r}') d\mathbf{r}' \\ &= -\int \left(\nabla \varphi_n^*(\mathbf{r}')\right) \delta(\mathbf{r} - \mathbf{r}') \varphi_n(\mathbf{r}') d\mathbf{r}' \\ &+ \sum_{[n_1, n_2, n_3]} \hat{n}_1 \int\int \left[\varphi_n^*(\mathbf{r}') \delta(n_1 - n_1') \varphi_n(\mathbf{r}')\right]_{n_1 = -\infty}^{+\infty} \delta(n_2 - n_2') \delta(n_3 - n_3') dn_2 dn_3, \end{aligned} \tag{2.3.57}$$

where the summation in the second term is to be read as

$$[n_1, n_2, n_3] \in \{[x, y, z], [y, z, x], [z, x, y]\}, \tag{2.3.58}$$

such that the sum cycles through all the Cartesian coordinates, and $\hat{n}_1$ denotes a Cartesian unit vector. However, the factor proportional to $\delta(n_1 - n_1')$ makes the entire second term vanish, due to the wave functions vanishing in the limit of large $\mathbf{r}$. Fortunately, the first term of equation (2.3.57) reduces to the desired result in agreement with equation (2.3.54).

2.3.3 Optical Properties of Excitonic Systems

Consider an electromagnetic vector potential on the form

$$\mathbf{A}(\mathbf{r}) = \mathbf{A}_0 \mathrm{e}^{i\mathbf{q}\cdot\mathbf{r}}, \tag{2.3.59}$$

which is to say that its spatial Fourier decomposition only has a single component. Moreover, the electric field can be written as

$$\mathbf{E} = -\nabla\phi' - \frac{\partial}{\partial t}\mathbf{A}', \tag{2.3.60}$$

where ϕ' is electric scalar potential. However, gauge fixing can be used to make the electric potential vanish, if $\xi := \Phi'$, where Φ' denotes the temporal integral of ϕ'. This also means that $\phi = 0$. In this gauge, it must hold true that $\mathbf{E} = i\omega\mathbf{A}$. The linear response function, $\overleftrightarrow{\boldsymbol{\sigma}}(\mathbf{r}, \mathbf{r}')$, is the conductivity, which is a non-local variable, since it relates different parts of space. It can be used to relate the electric field to the induced current density as

$$\mathbf{J}(\mathbf{r}) = i\omega \int \overleftrightarrow{\boldsymbol{\sigma}}(\mathbf{r}, \mathbf{r}')\mathbf{A}(\mathbf{r}')d\mathbf{r}'. \tag{2.3.61}$$

This means that the following equation must be satisfied:

$$i\omega \int \overleftrightarrow{\boldsymbol{\sigma}}(\mathbf{r}, \mathbf{r}')\mathbf{A}(\mathbf{r}')d\mathbf{r}' = \langle\psi|\hat{\mathbf{J}}(\mathbf{r}; \mathbf{r}_1, \ldots, \mathbf{r}_N)|\psi\rangle. \tag{2.3.62}$$

The full time-dependent wave function, $\Psi(\mathbf{r}_1, \ldots, \mathbf{r}_N, t)$, is a solution to the many-body time-dependent Schrödinger equation of the form

$$i\hbar\frac{\partial\Psi}{\partial t} = \Big\{\hat{\mathcal{H}}_0 + \frac{1}{2}\hat{\mathcal{H}}_1\mathrm{e}^{-i\omega t} + \frac{1}{2}\hat{\mathcal{H}}_1^\dagger\mathrm{e}^{i\omega t}\Big\}\Psi. \tag{2.3.63}$$

Notice, that Ψ is proportional to the fields perturbing the Hamiltonian [22, ch. 1]. As such, this wave function can be expanded with respect to the field

$$\Psi = \Psi^{(0)} + \Psi^{(1)} + \ldots, \tag{2.3.64}$$

where the superscript denotes the power of the perturbation. Considering only the last term of the current density operator (equation (2.3.55)) - the one proportional to the field, only the unperturbed part of the bra and ket of equation (2.3.62) will remain. This is due to the fact that the field corresponds to a first order perturbation, and only linear perturbations are considered in this project. Thus,

$$\mathbf{J}_A(\mathbf{r}) = i\omega \int \overleftrightarrow{\boldsymbol{\sigma}}_A(\mathbf{r}, \mathbf{r}')\mathbf{A}(\mathbf{r}')d\mathbf{r}' = \frac{e^2}{m}\int \Psi^{(0)*}\Big[\sum_n \delta(\mathbf{r} - \mathbf{r}_n)\mathbf{A}(\mathbf{r}_n)\Big]\Psi^{(0)}d\mathbf{r}_n. \tag{2.3.65}$$

Since only the spatial part of the unperturbed wave function is being considered, $\Psi^{(0)}(\mathbf{r}) = \psi(\mathbf{r})$, where $\psi(\mathbf{r})$ describes the Slater determinant of equation (2.3.40). Therefore, it can be seen that

$$\int \overleftrightarrow{\boldsymbol{\sigma}}_A(\mathbf{r}, \mathbf{r}')\mathbf{A}(\mathbf{r}')d\mathbf{r}' = \frac{e^2}{i\omega m}\sum_n \int \varphi_n^*(\mathbf{r}')\delta(\mathbf{r} - \mathbf{r}')\varphi_n(\mathbf{r}')\mathbf{A}(\mathbf{r}')d\mathbf{r}'. \tag{2.3.66}$$

Moreover, $\sum\limits_n \varphi_n^*\varphi_n$ is simply the electron density, $n(\mathbf{r})$, so the expression can be reduced to

$$\overleftrightarrow{\boldsymbol{\sigma}}_A(\mathbf{r}, \mathbf{r}') = \frac{e^2}{i\omega m}n(\mathbf{r}')\overleftrightarrow{\mathbf{I}}\,\delta(\mathbf{r} - \mathbf{r}'), \tag{2.3.67}$$

where $\overleftrightarrow{\mathbf{I}}$ is the unit dyadic. For the remaining part, equation (2.2.6) will be used. The interaction Hamiltonian is now only given by

$$\hat{H}_{1,p} = \frac{e}{2m}\sum_n \{\hat{\mathbf{p}}_n \cdot \mathbf{A}(\mathbf{r}_n) + \mathbf{A}(\mathbf{r}_n) \cdot \hat{\mathbf{p}}_n\}, \tag{2.3.68}$$

since the term related to $\mathbf{A}^2$ already has been incorporated in $\overleftrightarrow{\boldsymbol{\sigma}}_A(\mathbf{r},\mathbf{r}')$. This means that the current density, $\mathbf{J}_p(\mathbf{r})$, can be written as

$$\mathbf{J}_p(\mathbf{r},\omega) = -\sum_{k,l} f_{lk}\frac{\langle\psi_k|\hat{\mathcal{H}}_{1,p}|\psi_l\rangle\langle\psi_l|\hat{\mathbf{J}}_p(\mathbf{r};\mathbf{r}_1,\dots,\mathbf{r}_N)|\psi_k\rangle}{E_{kl}-\hbar\omega-i\hbar\Gamma}. \tag{2.3.69}$$

If $k = l$, then $f_{lk} = 0$, so the expression can be written in terms of $k > l$

$$\mathbf{J}_p(\mathbf{r},\omega) = -2\sum_{k>l} f_{lk}\frac{\langle\psi_k|\hat{\mathcal{H}}_{1,p}|\psi_l\rangle\langle\psi_l|\hat{\mathbf{J}}_p(\mathbf{r};\mathbf{r}_1,\dots,\mathbf{r}_N)|\psi_k\rangle}{E_{kl}-\hbar\omega-i\hbar\Gamma}. \tag{2.3.70}$$

Now, specialising to the case of intrinsic semiconductors, the ground state Slater determinant consists only of valence single-electron wave functions, that is

$$|0\rangle = |\varphi_{v_1},\dots,\varphi_{v_i},\dots,\varphi_{v_j},\dots,\varphi_{v_N}|. \tag{2.3.71}$$

Singly-excited states are of the form

$$|v_i \to c_j\rangle = |\varphi_{v_1},\dots,\varphi_{c_j},\dots,\varphi_{v_j},\dots,\varphi_{v_N}|, \tag{2.3.72}$$

that is to say φ_{v_i} has been excited to the state φ_{c_j}. Matrix elements for multiple excitations will have vanishing contributions due to the Fermi Dirac distribution. This also holds true for matrix elements between singly-excited states. The only contributions left is then those between singly-excited states and the ground state - for intrinsic semiconductors. For the ground state $f \approx 1$, whereas for the singly-excited states $f \approx 0$.

This project however, focuses heavily on excitonic states, which are essentially superpositions of states on the form of equation (2.3.72). As mentioned in section 2.3, such states can be written as

$$|exc\rangle = \sum_{i,j}\mathbf{\Psi}_{ij}^{exc}\cdot|v_i \to c_j\rangle, \tag{2.3.73}$$

where $|v_i \to c_j\rangle$ is a spinor as seen in equation (2.3.6). For ease of notation, the spinor notation will be removed. Instead i and j will hold a spin index, such that an excitonic state can be written simply as

$$|exc\rangle = \sum_{i,j}\Psi_{ij}^{exc}|v_i \to c_j\rangle, \tag{2.3.74}$$

where Ψ_{ij}^{exc} is now a scalar. Essentially this means, that $|\psi_l\rangle = |0\rangle$ and $|\psi_k\rangle = |exc\rangle$. The current density then reduces to

$$\mathbf{J}_p(\mathbf{r},\omega) = -2\sum_{exc}\frac{\langle exc|\hat{\mathcal{H}}_1|0\rangle\langle 0|\hat{\mathbf{J}}(\mathbf{r};\mathbf{r}_1,\dots,\mathbf{r}_N)|\,exc\rangle}{E_{exc}-\hbar\omega-i\hbar\Gamma}, \tag{2.3.75}$$

where the ground state energy has been set to zero, and E_{exc} is the corresponding eigenvalue to the excitonic state $|exc\rangle$. Due to Slater determinant selection rules for a sum of single electron operators [23, ch. 16], it can be seen that the expression reduces to

$$\begin{aligned}\mathbf{J}_p(\mathbf{r},\omega) = -\frac{2e^2}{4m^2}\sum_{exc}&\frac{\left(\sum_{i,j}(\Psi_{ij}^{exc})^*\langle\varphi_{c_j}(\mathbf{r}_i)|\hat{\mathbf{p}}_i\cdot\mathbf{A}(\mathbf{r}_i)+\mathbf{A}(\mathbf{r}_i)\cdot\hat{\mathbf{p}}_i|\varphi_{v_i}(\mathbf{r}_i)\rangle\right)}{E_{exc}-\hbar(\omega+i\Gamma)}\\ &\times\left(\sum_{i,j}\Psi_{ij}^{exc}\langle\varphi_{v_i}(\mathbf{r}_j)|\hat{\mathbf{p}}_j\delta(\mathbf{r}_j-\mathbf{r})+\delta(\mathbf{r}_j-\mathbf{r})\hat{\mathbf{p}}_j|\varphi_{c_j}(\mathbf{r}_j)\rangle\right).\end{aligned} \tag{2.3.76}$$

Using equation (2.3.61), it can easily be seen that the corresponding conductivity tensor, $\overleftrightarrow{\boldsymbol{\sigma}}_p(\mathbf{r},\mathbf{r}')$ is given as

$$\overleftrightarrow{\boldsymbol{\sigma}}_p(\mathbf{r},\mathbf{r}') = -\frac{2e^2}{i\omega m^2}\sum_{exc}\sum_{ij,kl}(\Psi_{ij}^{exc})^*\Psi_{kl}^{exc}\frac{\langle\varphi_{c_j}(\mathbf{r}_i)|\hat{\boldsymbol{\pi}}_\delta(\mathbf{r}_i,\mathbf{r}')|\varphi_{v_i}(\mathbf{r}_i)\rangle\langle\varphi_{v_k}(\mathbf{r}_l)|\hat{\boldsymbol{\pi}}_\delta(\mathbf{r}_l,\mathbf{r})|\varphi_{c_l}(\mathbf{r}_l)\rangle}{E_{exc}-\hbar(\omega+i\Gamma)}, \tag{2.3.77}$$

where

$$\hat{\boldsymbol{\pi}}_\delta(\mathbf{r}_n,\mathbf{r}) = \frac{1}{2}\{\hat{\mathbf{p}}_n\delta(\mathbf{r}_n-\mathbf{r})+\delta(\mathbf{r}_n-\mathbf{r})\hat{\mathbf{p}}_n\}. \tag{2.3.78}$$

The conductivity tensor is then found as

$$\overleftrightarrow{\boldsymbol{\sigma}}(\mathbf{r},\mathbf{r}') = \overleftrightarrow{\boldsymbol{\sigma}}_A(\mathbf{r},\mathbf{r}') + \overleftrightarrow{\boldsymbol{\sigma}}_p(\mathbf{r},\mathbf{r}'). \tag{2.3.79}$$

The current density can now be recovered using equation (2.3.61) again. This leads to the gauge current density:

$$\mathbf{J}_A(\mathbf{r}) = \frac{e^2}{m}n(\mathbf{r})\mathbf{A}(\mathbf{r}), \tag{2.3.80}$$

where $n(\mathbf{r})$ is the electron density. The momentum current density is a bit more complex. Notice, that the following expressions holds true:

$$\int\int \mathrm{e}^{i\mathbf{q}\cdot\mathbf{r}}\{\varphi_{c_j}^*(\mathbf{r}_i)\nabla_{\mathbf{r}_i}\delta(\mathbf{r}_i-\mathbf{r})\varphi_{v_i}(\mathbf{r}_i)\}d\mathbf{r}_i d\mathbf{r} = \int \varphi_{c_j}^*(\mathbf{r})\nabla_{\mathbf{r}}\mathrm{e}^{i\mathbf{q}\cdot\mathbf{r}}\varphi_{v_i}(\mathbf{r})d\mathbf{r}, \tag{2.3.81}$$

$$\int\int \mathrm{e}^{i\mathbf{q}\cdot\mathbf{r}}\{\varphi_{c_j}^*(\mathbf{r}_i)\delta(\mathbf{r}_i-\mathbf{r})\nabla_{\mathbf{r}_i}\varphi_{v_i}(\mathbf{r}_i)\}d\mathbf{r}_i d\mathbf{r} = \int \varphi_{c_j}^*(\mathbf{r})\mathrm{e}^{i\mathbf{q}\cdot\mathbf{r}}\nabla_{\mathbf{r}}\varphi_{v_i}(\mathbf{r})d\mathbf{r}. \tag{2.3.82}$$

The first of these two can be shown using partial integration similar to that of equation (2.3.57), whereas the second of the two is trivial. Using these two, it is easily seen that the momentum current density reduces to

$$\mathbf{J}_p(\mathbf{r}) = -\frac{2e^2\mathbf{A}_0}{m^2}\sum_{exc}\sum_{ij,kl}(\Psi_{ij}^{exc})^*\Psi_{kl}^{exc}\frac{\langle\varphi_{c_j}|\hat{\boldsymbol{\pi}}(\mathbf{q})|\varphi_{v_i}\rangle\langle\varphi_{v_k}(\mathbf{r}_l)|\hat{\boldsymbol{\pi}}_\delta(\mathbf{r}_l,\mathbf{r})|\varphi_{c_l}(\mathbf{r}_l)\rangle}{E_{exc}-\hbar(\omega+i\Gamma)}, \tag{2.3.83}$$

where

$$\hat{\boldsymbol{\pi}}(\mathbf{q}) = \frac{1}{2}\{\hat{\mathbf{p}}\mathrm{e}^{i\mathbf{q}\cdot\mathbf{r}}+\mathrm{e}^{i\mathbf{q}\cdot\mathbf{r}}\hat{\mathbf{p}}\}. \tag{2.3.84}$$

Analogous to equation (2.3.51), the induced response, meaning the current density, is of an equivalent form to the vector potential, and can thus be expressed as

$$\mathbf{J}(\mathbf{r}) = \mathbf{J}_0\mathrm{e}^{i\mathbf{q}\cdot\mathbf{r}}. \tag{2.3.85}$$

This can be considered as a spatial Fourier decomposition with only a single component. As such, the field strength, $\mathbf{J}_0$, of the current density can be found as

$$\mathbf{J}_0 = \frac{1}{\Omega}\int \mathbf{J}(\mathbf{r})\mathrm{e}^{-i\mathbf{q}\cdot\mathbf{r}}d\mathbf{r}. \tag{2.3.86}$$

For the gauge current density, the field strength simply reduces to

$$\mathbf{J}_{0,A} = \frac{e^2}{m\Omega}\mathbf{A}_0. \tag{2.3.87}$$

The field strength of the momentum current density, reduces to

$$\mathbf{J}_{0,p} = -\frac{2e^2\mathbf{A}_0}{m^2\Omega}\sum_{exc}\sum_{ij,kl}(\Psi_{ij}^{exc})^*\Psi_{kl}^{exc}\frac{\langle\varphi_{c_j}|\hat{\boldsymbol{\pi}}(\mathbf{q})|\varphi_{v_i}\rangle\langle\varphi_{v_k}|\hat{\boldsymbol{\pi}}(-\mathbf{q})|\varphi_{c_l}\rangle}{E_{exc}-\hbar(\omega+i\Gamma)}. \tag{2.3.88}$$

In a crystalline system, the wave functions can be written as a product of a lattice periodic function and a plane wave, that is $\varphi_{n\mathbf{k}}(\mathbf{r}) = u_{n\mathbf{k}}(\mathbf{r})\exp(i\mathbf{k}\cdot\mathbf{r})$, by Bloch's theorem. Moreover, if $|\varphi_{c_j}\rangle = |\varphi_{c\mathbf{k}'}\rangle$ and $|\varphi_{v_i}\rangle = |\varphi_{v\mathbf{k}}\rangle$, then it must hold true that $\mathbf{k}' = \mathbf{k}+\mathbf{q}$, which is in agreement with conservation of momentum. Equation (2.3.88) can be averaged by adding to it a similar expression derived from equation (2.3.70), but with k and l interchanged. This would lead to

$$\mathbf{J}_{0,p} = -\frac{2e^2\mathbf{A}_0}{m^2\Omega}\sum_{exc}\sum_{ij,kl}(\Psi_{ij}^{exc})^*\Psi_{kl}^{exc}\frac{E_{exc}\langle\varphi_{c_j}|\hat{\boldsymbol{\pi}}(\mathbf{q})|\varphi_{v_i}\rangle\langle\varphi_{v_k}|\hat{\boldsymbol{\pi}}(-\mathbf{q})|\varphi_{c_l}\rangle}{E_{exc}^2-\hbar^2(\omega+i\Gamma)^2}. \tag{2.3.89}$$

It is worth noticing that

$$\langle\varphi_{c_j}|\hat{\boldsymbol{\pi}}(\mathbf{q})|\varphi_{v_i}\rangle^* = \langle\varphi_{v_i}|\hat{\boldsymbol{\pi}}(-\mathbf{q})|\varphi_{c_j}\rangle. \tag{2.3.90}$$

Moreover, $\mathbf{J}(\mathbf{r},t) = \dot{\mathbf{P}}(\mathbf{r},t)$, where $\mathbf{P}$ denotes the polarisation density, and $\mathbf{P}(\mathbf{r},t) = \varepsilon_0\overleftrightarrow{\chi}\mathbf{E}(\mathbf{r},t)$, where $\overleftrightarrow{\chi}$ denotes the electric susceptibility. Therefore,

$$\mathbf{J}_0 = \omega^2\varepsilon_0\overleftrightarrow{\chi}\cdot\mathbf{A}_0. \tag{2.3.91}$$

Using this, it is quite easy to see that

$$\overleftrightarrow{\chi}(\omega,\mathbf{q}) = -\frac{e^2}{\varepsilon_0 m\omega^2\Omega}\overleftrightarrow{\mathbf{I}} + \frac{2e^2}{\varepsilon_0\omega^2 m^2\Omega}\sum_{exc}\sum_{ij,kl}(\Psi_{ij}^{exc})^*\Psi_{kl}^{exc}\frac{E_{exc}\langle\varphi_{c_j}|\hat{\boldsymbol{\pi}}(\mathbf{q})|\varphi_{v_i}\rangle\langle\varphi_{v_k}|\hat{\boldsymbol{\pi}}(-\mathbf{q})|\varphi_{c_l}\rangle}{E_{exc}^2-\hbar^2(\omega+i\Gamma)^2}. \tag{2.3.92}$$

The expression can be reduced by expanding the second term and using the Thomas-Reiche-Kuhn sum rule [22], such that it reduces to

$$\overleftrightarrow{\chi}(\omega,\mathbf{q}) = \frac{2e^2\hbar^2}{\varepsilon_0 m^2\Omega}\sum_{exc}\sum_{ij,kl}(\Psi_{ij}^{exc})^*\Psi_{kl}^{exc}\frac{\langle\varphi_{c_j}|\hat{\boldsymbol{\pi}}(\mathbf{q})|\varphi_{v_i}\rangle\langle\varphi_{v_k}|\hat{\boldsymbol{\pi}}(-\mathbf{q})|\varphi_{c_l}\rangle}{E_{exc}[E_{exc}^2-\hbar^2(\omega+i\Gamma)^2]}. \tag{2.3.93}$$

Diagonal elements of the susceptibility can be considered. For the xx-case, this would be

$$\chi_{xx}(\omega,\mathbf{q}) = \frac{2e^2\hbar^2}{\varepsilon_0 m^2\Omega}\sum_{exc}\frac{\left|\sum_{k,l}\Psi_{kl}^{exc}\langle\varphi_{v_k}|\hat{\pi}_x(-\mathbf{q})|\varphi_{c_l}\rangle\right|^2}{E_{exc}[E_{exc}^2-\hbar^2(\omega+i\Gamma)^2]}. \tag{2.3.94}$$

Alternatively, this expression can be written in terms of the excitonic states:

$$\chi_{xx}(\omega,\mathbf{q}) = \frac{2e^2\hbar^2}{\varepsilon_0 m^2\Omega}\sum_{exc}\frac{|\langle 0\,|\hat{P}_x(\mathbf{q})|\,exc\rangle|^2}{E_{exc}[E_{exc}^2-\hbar^2(\omega+i\Gamma)^2]}, \tag{2.3.95}$$

where

$$\hat{P}_x(\mathbf{q}) = \sum_n \tfrac{1}{2}\{\hat{p}_x\mathrm{e}^{-i\mathbf{q}\cdot\mathbf{r}} + \mathrm{e}^{-i\mathbf{q}\cdot\mathbf{r}}\hat{p}_x\}. \tag{2.3.96}$$

Equations (2.3.94) and (2.3.95) computes the response in the x-direction induced by a field propagating in the x-direction. Lastly, the xx element of the conductivity can easily be recovered from the susceptibility, using $\sigma_{xx} = -i\omega\varepsilon_0\chi_{xx}$.

2.3.4 Emission Rate for Two-Dimensional Systems

Fermi's Golden rule will be the starting point for calculating the rate of spontaneous emission. One formulation of this rule is as follows [22]:

$$\Gamma = \frac{2\pi}{\hbar}\sum_f |\langle f|\hat{\mathcal{H}}_{int}|i\rangle|^2\delta(E_{fi}), \tag{2.3.97}$$

where i and f denotes initial and final states, respectively, and $E_{fi} = E_f - E_i$. Moreover, the interaction Hamiltonian, $\hat{\mathcal{H}}_{int}$, is the Hamiltonian seen in equation (2.3.37), but for a many-electron system, that is

$$\hat{\mathcal{H}}_{int} = \frac{e}{2m}\sum_e \left\{\hat{\mathbf{p}}_e \cdot \mathbf{A}(\mathbf{r}_e) + \mathbf{A}(\mathbf{r}_e)\cdot\hat{\mathbf{p}}_e\right\}, \tag{2.3.98}$$

where the sum covers all electrons in the system. The term involving the square of the vector-potential corresponds to a second-order pertubation, and is therefore discarded. Next, the free-space field may be quantised as seen in equation (2.1.27), namely

$$\hat{\mathbf{A}}(\mathbf{r}) = \sum_{\mathbf{q}}\sum_{\lambda=1,2} \mathbf{e}_{\mathbf{q}\lambda}\left(\frac{\hbar}{2\varepsilon_0\Omega\omega_q}\right)^{\frac{1}{2}}\left\{\hat{a}_{\mathbf{q}\lambda}\mathrm{e}^{i\mathbf{q}\cdot\mathbf{r}} + \hat{a}^{\dagger}_{\mathbf{q}\lambda}\mathrm{e}^{-i\mathbf{q}\cdot\mathbf{r}}\right\}. \tag{2.3.99}$$

The final and initial states can be represented as

$$|i\rangle = |exc\rangle \otimes |n_{\mathbf{q}\lambda} = 0\rangle, \quad |f\rangle = |0\rangle \otimes |n_{\mathbf{q}\lambda} = 1\rangle, \tag{2.3.100}$$

where $\otimes$ denotes a tensor product. Since $\hat{a}_{\mathbf{q}\lambda}$ represents the annihilation operator, terms involving this operator reduces to zero when operating on the initial state. What remains is then

$$\Gamma = \frac{\pi\hbar e^2}{m^2\Omega\varepsilon_0 E_{exc}}\sum_{\mathbf{q},\lambda}|\mathbf{e}_{\mathbf{q}\lambda}\cdot\tfrac{1}{2}\langle 0|\sum_e\{\hat{\mathbf{p}}_e\mathrm{e}^{-i\mathbf{q}\cdot\mathbf{r}_e} + \mathrm{e}^{-i\mathbf{q}\cdot\mathbf{r}_e}\hat{\mathbf{p}}_e\}|exc\rangle|^2\delta(\hbar\omega_q - E_{exc}). \tag{2.3.101}$$

This can be reduced further by the fact that $\omega_q = cq$ and by letting $E_{exc} = \hbar\omega$. Using the scaling property of Dirac delta functions will lead to

$$\Gamma = \frac{\pi e^2}{m^2\Omega\varepsilon_0\hbar\omega c}\sum_{\mathbf{q},\lambda}|\mathbf{e}_{\mathbf{q}\lambda}\cdot\mathbf{P}_{exc}|^2\delta\left(q - \frac{\omega}{c}\right), \quad \mathbf{P}_{exc} = \frac{1}{2}\langle 0|\sum_e\{\hat{\mathbf{p}}_e\mathrm{e}^{-i\mathbf{q}\cdot\mathbf{r}_e} + \mathrm{e}^{-i\mathbf{q}\cdot\mathbf{r}_e}\hat{\mathbf{p}}_e\}|exc\rangle. \tag{2.3.102}$$

The ground state can be written as the simple Slater determinant seen in equation (2.3.1). The excitonic state can be expressed in a manner similar to equation (2.3.7), that is

$$|exc\rangle = \sum_{v,c,\mathbf{k}} \boldsymbol{\Psi}^{c,\mathbf{k}+\mathbf{Q}}_{v,\mathbf{k}}\cdot|v\mathbf{k}\to c(\mathbf{k}+\mathbf{Q})\rangle, \tag{2.3.103}$$

where $|v\mathbf{k}\to c(\mathbf{k}+\mathbf{Q})\rangle$ is a spinor, and $\hbar\mathbf{Q}$ is the center-of-mass momentum of the excitonic state. To ease notation in the proceeding, let $\mathbf{k}' = \mathbf{k}+\mathbf{Q}$. From here, the selection rules of matrix elements between Slater determinants [23] may be used to rewrite the excitonic momentum to

$$\mathbf{P}_{exc} = \frac{1}{2}\sum_{v,c,\mathbf{k}}\sum_{\sigma,\sigma'}\Psi^{c,\mathbf{k}',\sigma'}_{v,\mathbf{k},\sigma}\langle v\mathbf{k}\sigma\,|\,\hat{\mathbf{p}}\mathrm{e}^{-i\mathbf{q}\cdot\mathbf{r}} + \mathrm{e}^{-i\mathbf{q}\cdot\mathbf{r}}\hat{\mathbf{p}}\,|\,c\mathbf{k}'\sigma'\rangle\,\delta_{\sigma\sigma'}, \tag{2.3.104}$$

where $\sigma,\sigma' \in \{\uparrow,\downarrow\}$. The states $|v\mathbf{k}\sigma\rangle$ and $|c\mathbf{k}'\sigma'\rangle$ are single electron states, and the Kronecker delta arises, since non spin preserving transitions are forbidden. Moreover, since the system is assumed to be periodic, the single electron states can be Bloch-expanded, such that $|n\mathbf{k}\rangle = u_{n,\mathbf{k}}(\mathbf{r})\exp(i\mathbf{k}\cdot\mathbf{r})$. Using this expansion clearly shows that

$$\langle u_{v,\mathbf{k}}\mathrm{e}^{i\mathbf{k}\cdot\mathbf{r}}\,|\,\hat{\mathbf{p}}\mathrm{e}^{-i\mathbf{q}\cdot\mathbf{r}} + \mathrm{e}^{-i\mathbf{q}\cdot\mathbf{r}}\hat{\mathbf{p}}\,|\,u_{c,\mathbf{k}+\mathbf{Q}}\mathrm{e}^{i(\mathbf{k}+\mathbf{Q})\cdot\mathbf{r}}\rangle \propto \delta_{\mathbf{q},\mathbf{Q}}. \tag{2.3.105}$$

However, for materials which are not periodic along z, $Q_z = 0$ where $\mathbf{Q} = \mathbf{Q}_{\|} + \hat{z}Q_z$ and $\mathbf{Q}_{\|}$ lies in plane of the material. In such a system, the exciton momentum takes the form

$$\mathbf{P}_{exc} = \frac{1}{2}\sum_{v,c,\mathbf{k},\sigma}\Psi^{c,\mathbf{k}',\sigma}_{v,\mathbf{k},\sigma}\langle v\mathbf{k}\sigma\,|\,\hat{\mathbf{p}}\mathrm{e}^{-i(\mathbf{Q}_{\|}\cdot\mathbf{r}+q_z z)} + \mathrm{e}^{-i(\mathbf{Q}_{\|}\cdot\mathbf{r}+q_z z)}\hat{\mathbf{p}}\,|\,c\mathbf{k}'\sigma\rangle\,\delta_{q_x,Q_x}\delta_{q_y,Q_y}. \tag{2.3.106}$$

Now, it is worth mentioning that $\mathbf{e}_{\mathbf{q}\lambda}$ are perpendicular unit vectors to the propagation vector $\mathbf{q}$, which has unit vector $\hat{q}$. As such, the following trick can be used:

$$\sum_{\lambda} \mathbf{e}_{\mathbf{q}\lambda} \mathbf{e}_{\mathbf{q}\lambda} = \overleftrightarrow{\mathbf{I}} - \hat{q}\hat{q}. \tag{2.3.107}$$

Moreover, notice that in the limit of very small Δq_z, the following relation must hold true:

$$\sum_{q_z} f(q_z) \frac{\Delta q_z}{\Delta q_z} \to \frac{1}{\Delta q_z} \int f(q_z) dq_z = \frac{L}{2\pi} \int f(q_z) dq_z, \tag{2.3.108}$$

where L is the side-length of the quantisation cavity as seen in equation (2.1.10). Thus, by converting the q_z sum in equation (2.3.102) to an integral, the expression can be rewritten as

$$\Gamma(\mathbf{Q}) = \frac{e^2}{2m^2 A \varepsilon_0 \hbar \omega c} \sum_{q_x, q_y} \delta_{q_x, Q_x} \delta_{q_y, Q_y} \int \mathbf{P}^*_{exc} \cdot (\overleftrightarrow{\mathbf{I}} - \hat{q}\hat{q}) \cdot \mathbf{P}_{exc}\, \delta \left(q - \frac{\omega}{c} \right) dq_z. \tag{2.3.109}$$

Technically, $\delta_{q_x, Q_x} \delta_{q_y, Q_y}$ can now be safely removed from the exciton momentum seen in equation (2.3.106).

2.4 Purcell Effect

The Purcell effect describes the effects of the surroundings on emitted power of a (dipole) source. As such, the emission rate and the lifetime of a given emitter can be tuned by changing the immediate dielectric geometry. A two-dimensional emitter can hardly be considered a dielectric material, so when such a material is incorporated in the geometry, the Fresnel coefficients will be quite different from the usual ones. This is also described in this section.

2.4.1 A Planar Dipole

Consider a *planar dipole*, which corresponds to a dipole constrained to the plane $z = z_0$ with a given in-plane momentum, $\hbar\mathbf{Q}$. The current density for this dipole is given as

$$\mathbf{J}(\mathbf{r}) = -\frac{i\omega}{A} \boldsymbol{\mu}(\mathbf{Q}) \delta(z - z_0) \mathrm{e}^{i\mathbf{Q}\cdot\boldsymbol{\rho}}, \tag{2.4.1}$$

where $\boldsymbol{\mu}$ is the dipole moment, and A denotes the plane area, which will later be assumed to be infinite. The direct electric field emitted by the dipole can be found using the direct Green's tensor as

$$\mathbf{E}^{(d)}(\mathbf{r}) = i\omega\mu_0 \int \overleftrightarrow{\mathbf{G}}^{(d)}(\mathbf{r}, \mathbf{r}') \cdot \mathbf{J}(\mathbf{r}') d^3 r'. \tag{2.4.2}$$

The direct Green's tensor is given as [25, ch. 10]

$$\begin{aligned} \overleftrightarrow{\mathbf{G}}^{(d)}(\mathbf{r}, \mathbf{r}') &= \frac{i}{8\pi^2} \iint\limits_{-\infty}^{\infty} \overleftrightarrow{\mathbf{M}} \mathrm{e}^{i[k_x(x-x') + k_y(y-y') + k_{z1}|z-z'|]} dk_x dk_y, \\ \overleftrightarrow{\mathbf{M}} &= \frac{1}{k_1^2 k_{z1}} \begin{bmatrix} k_1^2 - k_x^2 & -k_x k_y & \mp k_x k_{z1} \\ -k_x k_y & k_1^2 - k_y^2 & \mp k_y k_{z1} \\ \mp k_x k_{z1} & \mp k_y k_{z1} & k_1^2 - k_{z1}^2 \end{bmatrix}, \end{aligned} \tag{2.4.3}$$

where $\overleftrightarrow{\mathbf{M}}$ follows the convention:

$$\begin{bmatrix} \hat{x}\hat{x} & \hat{x}\hat{y} & \hat{x}\hat{z} \\ \hat{y}\hat{x} & \hat{y}\hat{y} & \hat{y}\hat{z} \\ \hat{z}\hat{x} & \hat{z}\hat{y} & \hat{z}\hat{z} \end{bmatrix}. \tag{2.4.4}$$

Using the Green's formulation to calculate the electric field, the order of integration can be changed, such that the $\mathbf{r}'$ integral is carried out first. Clearly, the z' integral simply vanishes, whereas the x' and y' integrals provides the factors $\delta(Q_x - k_x)$ and $\delta(Q_y - k_y)$, respectively. Formally,

$$\begin{aligned}\mathbf{E}(\mathbf{r}) &= \frac{i\mu_0\omega^2}{8\pi^2}4\pi^2 \int \overleftrightarrow{\mathbf{M}}(k_x, k_y) \cdot \boldsymbol{\mu}(Q_x, Q_y)\delta(Q_x - k_x)\delta(Q_y - k_y)\mathrm{e}^{i(k_x x + k_y y)} dk_x dk_y \\ &= \frac{i\mu_0\omega^2}{2}\overleftrightarrow{\mathbf{M}}(Q_x, Q_y) \cdot \boldsymbol{\mu}(Q_x, Q_y)\mathrm{e}^{i(Q_x x + Q_y y)}. \end{aligned} \tag{2.4.5}$$

The dissipated power, corresponding to the direct field, can be found using Poynting's theorem, which states that

$$\frac{dW^{(d)}}{dt} = -\frac{1}{2}\int_V \mathrm{Re}\big\{\mathbf{J}^*(\mathbf{r}) \cdot \mathbf{E}^{(d)}(\mathbf{r})\big\} d^3r. \tag{2.4.6}$$

Notice, that when $\mathbf{J}^*(\mathbf{r})$ is inserted, the exponentials cancel. As such, the in-plane integrand is independent of x and y, meaning that it will cancel with A^{-1}. Furthermore, the z-integral vanishes due to $\delta(z - z_0)$. The remaining expression is then

$$\dot{W}^{(d)}(\mathbf{Q}) = \frac{\mu_0\omega^3}{4}\mathrm{Re}\Big\{(\boldsymbol{\mu}(\mathbf{Q}))^* \cdot \overleftrightarrow{\mathbf{M}}(\mathbf{Q}) \cdot \boldsymbol{\mu}(\mathbf{Q})\Big\}. \tag{2.4.7}$$

Thus, this is the dissipated power of a planar dipole in a homogeneous dielectric environment.

In the case of an inhomogeneous dielectric environment, the electric field used in equation (2.4.6) is

$$\mathbf{E}(\mathbf{r}) = \mathbf{E}^{(d)}(\mathbf{r}) + \mathbf{E}^{(i)}(\mathbf{r}), \tag{2.4.8}$$

where i denotes the indirect field. Since the direct contribution to the dissipated power has already been found, the focus should be directed towards the indirect contribution. In this case, the corresponding indirect Green's tensor for a single planar interface is [25, ch. 10]

$$\begin{aligned}\overleftrightarrow{\mathbf{G}}^{(i)}(\mathbf{r}, \mathbf{r}') &= \frac{i}{8\pi^2}\iint_{-\infty}^{\infty} \Big[\overleftrightarrow{\mathbf{M}}^s + \overleftrightarrow{\mathbf{M}}^p\Big] \mathrm{e}^{i[k_x(x-x') + k_y(y-y') + k_{z1}(z+z')]} dk_x dk_y, \\ \overleftrightarrow{\mathbf{M}}^s &= \frac{r^{(s)}(k_x, k_y)}{k_{z1}(k_x^2 + k_y^2)}\begin{bmatrix} k_y^2 & -k_x k_y & 0 \\ -k_x k_y & k_x^2 & 0 \\ 0 & 0 & 0\end{bmatrix}, \\ \overleftrightarrow{\mathbf{M}}^p &= \frac{-r^{(p)}(k_x, k_y)}{k_1^2(k_x^2 + k_y^2)}\begin{bmatrix} k_x^2 k_{z1} & k_x k_y k_{z1} & k_x(k_x^2 + k_y^2) \\ k_x k_y k_{z1} & k_y^2 k_{z1} & k_y(k_x^2 + k_y^2) \\ -k_x(k_x^2 + k_y^2) & -k_y(k_x^2 + k_y^2) & -(k_x^2 + k_y^2)^2/k_{z1}\end{bmatrix}. \end{aligned} \tag{2.4.9}$$

The process for deriving the indirect dissipated power is analogous to that of the direct. The final expression becomes

$$\dot{W}^{(i)}(\mathbf{Q}) = \frac{\mu_0\omega^3}{4}\mathrm{Re}\Big\{(\boldsymbol{\mu}(\mathbf{Q}))^* \cdot \Big(\overleftrightarrow{\mathbf{M}}^s(\mathbf{Q}) + \overleftrightarrow{\mathbf{M}}^p(\mathbf{Q})\Big)\mathrm{e}^{2ik_{z1}z_0} \cdot \boldsymbol{\mu}(\mathbf{Q})\Big\}. \tag{2.4.10}$$

The mode-dependent Purcell effect, $P(\mathbf{Q})$, is then defined as

$$P(\mathbf{Q}) := \frac{\dot{W}^{(d)}(\mathbf{Q}) + \dot{W}^{(i)}(\mathbf{Q})}{\dot{W}^{(d)}(\mathbf{Q})} = 1 + \frac{\dot{W}^{(i)}(\mathbf{Q})}{\dot{W}^{(d)}(\mathbf{Q})}, \tag{2.4.11}$$

meaning it is the ratio of dissipated power in an inhomogeneous environment to that of the corresponding homogeneous environment.

2.4.2 Fresnel Coefficients for a Conducting Sheet Interface

Consider a dielectric environment, where a two-dimensional sheet lies at height z_0 between two materials with no magnetisation, such that

$$\varepsilon(z) = \begin{cases} \varepsilon_1, & z > z_0^+ \\ \varepsilon_2, & z < z_0^- \end{cases}, \tag{2.4.12}$$

where both dielectric constants are assumed real and positive. This can also be seen in figure 2.4.1.

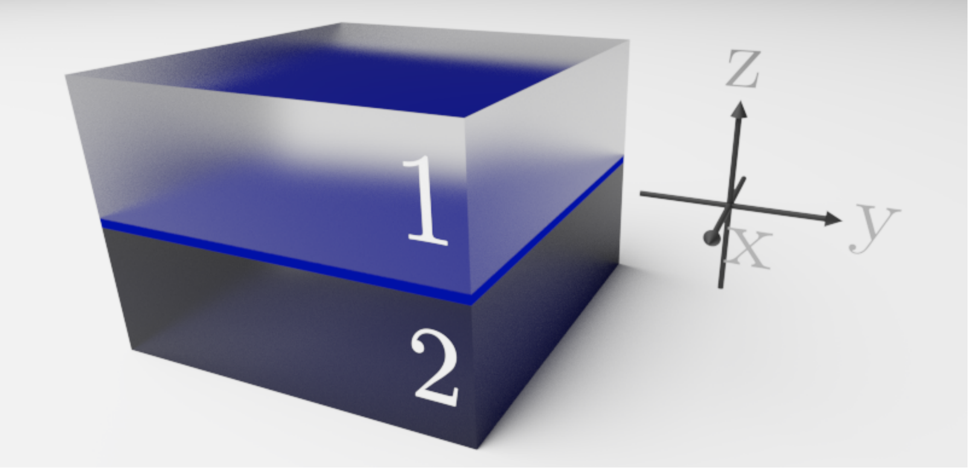

Figure 2.4.1: Two different media surrounding around an emitter.

The two dimensional interface between the two regions can then be described using a sheet current $\mathbf{J}_s$ and charge density ρ_s. The boundary conditions for such an interface are

$$\begin{aligned} &(1)\ \hat{z} \times \big(\mathbf{E}(\boldsymbol{\rho}, z_0^-) - \mathbf{E}(\boldsymbol{\rho}, z_0^+)\big) = \mathbf{0}, && (2)\ \hat{z} \cdot \big(\varepsilon_1 \mathbf{E}(\boldsymbol{\rho}, z_0^-) - \varepsilon_2 \mathbf{E}(\boldsymbol{\rho}, z_0^+)\big) = -\frac{\rho_s}{\varepsilon_0}, \\ &(3)\ \hat{z} \times \big(\mathbf{B}(\boldsymbol{\rho}, z_0^-) - \mathbf{B}(\boldsymbol{\rho}, z_0^+)\big) = -\mu_0 \mathbf{J}_s, && (4)\ \hat{z} \cdot \big(\mathbf{B}(\boldsymbol{\rho}, z_0^-) - \mathbf{B}(\boldsymbol{\rho}, z_0^+)\big) = 0, \end{aligned}$$

where the parallel and perpendicular subscripts are defined relative to the interface plane. Consider then a single wave-component of the electric field propagating through the upper medium towards the interface. The plane of incidence is taken to be the xz-plane and therefore, it should hold that $q_1^2 = q_x^2 + q_{z1}^2$. From here, the two cases of s- and p-polarisation may be considered.

Firstly, for s-polarisation, the direct electric field can be expressed as

$$\mathbf{E}^{(d)} = E^{(d)} \mathrm{e}^{i(q_x x - q_{zi} z)} \hat{y}. \tag{2.4.13}$$

Moreover, the magnetic field can then be found using $i\omega\mathbf{B} = \nabla \times \mathbf{E}$. In medium 1, the total fields have contributions from the direct field and the indirect field. Similarly, in medium 2 the total fields are merely the transmitted ones. The three electric and magnetic fields are then

$$\mathbf{E}^{(d)} = E^{(d)} \mathrm{e}^{i(q_x x - q_{z1} z)} \hat{y}, \quad \mathbf{B}^{(d)} = \frac{E^{(d)}}{\omega} (q_{z1} \hat{x} + q_x \hat{z}) \mathrm{e}^{i(q_x x - q_{z1} z)}, \tag{2.4.14}$$

$$\mathbf{E}^{(i)} = E^{(i)} \mathrm{e}^{i(q_x x + q_{z1} z)} \hat{y}, \quad \mathbf{B}^{(i)} = \frac{E^{(i)}}{\omega} (-q_{z1} \hat{x} + q_x \hat{z}) \mathrm{e}^{i(q_x x + q_{z1} z)}, \tag{2.4.15}$$

$$\mathbf{E}^{(t)} = E^{(t)} \mathrm{e}^{i(q_x x - q_{z2} z)} \hat{y}, \quad \mathbf{B}^{(t)} = \frac{E^{(t)}}{\omega} (q_{z2} \hat{x} + q_x \hat{z}) \mathrm{e}^{i(q_x x - q_{z2} z)}. \tag{2.4.16}$$

Applying the appropriate boundary conditions, (1) and (3), at $z = z_0 = 0$ then leads to

$$E^{(t)} - E^{(d)} - E^{(i)} = 0, \tag{2.4.17}$$

$$q_{z2}E^{(t)} - q_{z1}\big(E^{(d)} - E^{(i)}\big) = -\omega\mu_0 J_{s,y}. \tag{2.4.18}$$

Now, the usual current density can be found using $\mathbf{J} = \overleftrightarrow{\boldsymbol{\sigma}} \cdot \mathbf{E}$. For the sheet current density $\overleftrightarrow{\boldsymbol{\sigma}} = \overleftrightarrow{\boldsymbol{\sigma}}_s$ is a tensor which only relates x and y, and $\mathbf{E} = \mathbf{E}_{\|}$. Therefore, the sheet current density can be found as $\mathbf{J}_s = \overleftrightarrow{\boldsymbol{\sigma}}_s \cdot \mathbf{E}_{\|}(z = z_0)$. The sheet conductivity is assumed invariant with respect to the in-plane angle and can therefore simply be replaced by σ_s. This reduces equation (2.4.18) to

$$q_{z2}E^{(t)} - q_{z1}\big(E^{(d)} - E^{(i)}\big) = -\omega\mu_0\sigma_s E^{(t)}. \tag{2.4.19}$$

By inserting $E^{(t)} = E^{(d)} + E^{(i)}$ in equation (2.4.19) and solving for the reflective coefficient, one will obtain

$$r_s := \frac{E^{(i)}}{E^{(d)}} = \frac{q_{z1} - q_{z2} - \omega\mu_0\sigma_s}{q_{z1} + q_{z2} + \omega\mu_0\sigma_s}. \tag{2.4.20}$$

The transmission coefficient can be found using a similar approach. It is given as

$$t_s := \frac{E^{(t)}}{E^{(d)}} = \frac{2q_{z1}}{q_{z1} + q_{z2} + \omega\mu_0\sigma_s}, \tag{2.4.21}$$

which is to say that $t_s = 1 + r_s$.

A similar approach can be used for the p-polarised part of the field. In this case, the direct magnetic field is exclusively along the y-direction, such that

$$\mathbf{B}^{(d)} = B^{(d)}\mathrm{e}^{i(q_x x - q_{z1}z)}\hat{y}, \tag{2.4.22}$$

where the electric field can be found using $-i\omega\varepsilon\mathbf{E} = c^2\nabla \times \mathbf{B}$. In any case, the three electric and magnetic fields become

$$\mathbf{B}^{(d)} = B^{(d)}\mathrm{e}^{i(q_x x - q_{z1}z)}\hat{y}, \quad \mathbf{E}^{(d)} = -\frac{c^2B^{(d)}}{\varepsilon_1\omega}(q_{z1}\hat{x} + q_x\hat{z})\mathrm{e}^{i(q_x x - q_{z1}z)}, \tag{2.4.23}$$

$$\mathbf{B}^{(i)} = B^{(i)}\mathrm{e}^{i(q_x x + q_{z1}z)}\hat{y}, \quad \mathbf{E}^{(i)} = -\frac{c^2B^{(i)}}{\varepsilon_1\omega}(-q_{z1}\hat{x} + q_x\hat{z})\mathrm{e}^{i(q_x x + q_{z1}z)}, \tag{2.4.24}$$

$$\mathbf{B}^{(t)} = B^{(t)}\mathrm{e}^{i(q_x x - q_{z2}z)}\hat{y}, \quad \mathbf{E}^{(t)} = -\frac{c^2B^{(t)}}{\varepsilon_2\omega}(q_{z2}\hat{x} + q_x\hat{z})\mathrm{e}^{i(q_x x - q_{z2}z)}. \tag{2.4.25}$$

Applying boundary conditions (1) and (3) leads to

$$B^{(t)}\frac{q_{z2}}{\varepsilon_2} - \big(B^{(d)} - B^{(i)}\big)\frac{q_{z1}}{\varepsilon_1} = 0, \tag{2.4.26}$$

$$B^{(d)} + B^{(i)} - B^{(t)} = -\mu_0 J_{s,x}. \tag{2.4.27}$$

Once again, it can be used that $\mathbf{J}_s = \sigma_s\mathbf{E}_{\|}$, such that $J_{s,x} = \sigma_s E_x^{(t)}$, which leads to

$$B^{(d)} + B^{(i)} - B^{(t)} = \frac{\mu_0\sigma_s c^2 q_{z2}}{\varepsilon_2\omega}B^{(t)}. \tag{2.4.28}$$

Now, by using the two boundary conditions and some algebra, the following expression for the p-polarised reflection coefficient is found:

$$r_p := \frac{B^{(i)}}{B^{(d)}} = \frac{q_{z1}\varepsilon_2 - q_{z2}\varepsilon_1 + q_{z1}q_{z2}\sigma_s(\omega\varepsilon_0)^{-1}}{q_{z1}\varepsilon_2 + q_{z2}\varepsilon_1 + q_{z1}q_{z2}\sigma_s(\omega\varepsilon_0)^{-1}}. \tag{2.4.29}$$

Next, the transmission coefficient can be found as

$$t_p := \frac{B^{(t)}}{B^{(d)}} = \left(1 - \frac{B^{(i)}}{B^{(d)}}\right)\frac{q_{z1}\varepsilon_2}{q_{z2}\varepsilon_1} = \Big(1 - r_p\Big)\frac{q_{z1}\varepsilon_2}{q_{z2}\varepsilon_1}. \tag{2.4.30}$$

3 Implementation

For the purpose of modelling the electronic properties of the TMDs covered in this project, the software library GPAW [3–7] has been used in conjunction with code of our own. Moreover, we have made use of the DTU-developed database C2DB in order to avoid having to compute already known properties of the 2D materials. This includes lattice constants, polarizability and fundamental bandgaps among others.

In particular, GPAW was used for calculating the one-electron wave functions, in a plane wave basis, using density functional theory (DFT) and the PAW method. The excitonic properties were then determined by solving the Bethe-Salpeter equation (BSE) for the wave functions obtained from the DFT, but scissor shifted to match the fundamental bandgap. Theoretical fundamental bandgaps for the considered TMDs can be seen in table 3.1. The BSE was then solved for non-zero center of mass momenta, yielding a dispersion relation, which is then used to calculate the emission rate. In this chapter, MoS_2 will be used as a reference TMD, such that the results easily can be referred to literature considering MoS_2.

TMD	MoS_2	$MoSe_2$	WS_2	WSe_2
G0W0 Bandgap (eV) [20]	2.53	2.12	2.53	2.10

Table 3.1: A table of the fundamental bandgap values for the considered TMDs calculated by G0W0.

3.1 Density Functional Theory using GPAW

When performing DFT calculations using GPAW, there are many parameters which can be tuned. One of these parameters is the choice of exchange-correlation functional, denoted XC. The XC used in the report will be the so-called 'PBE'-functional [26], which is an example of the generalised gradient approximation (GGA).

Another important metric that should be considered during the DFT calculations is the choice of k-point grid. One of the main purposes of the DFT calculations in this project is to enable a BSE calculation, and in such a calculation all k-points couple to one-another. Therefore, it is not sufficient to merely consider the irreducible element, but instead the entire first Brillouin zone should be discretised. However, as can be seen in figure 4.2.1, the primary excitons are localised in the K-point of symmetry. As such, it is numerically favorable to have a k-point grid, where the K-point is found not along the edges, but in the interior of the grid. Thus, the k-point grid used in this report is a Monkhorst-grid spanning $\mathbf{k} \in ([0,1],[0,1])$ in the space of the reciprocal lattice vectors. Furthermore, it is chosen to be slightly displaced relative to the Γ-point, which can be seen in figure 3.1.1a and 3.1.1b.

As mentioned, all calculations will be performed in the PAW formalism with pseudo wave

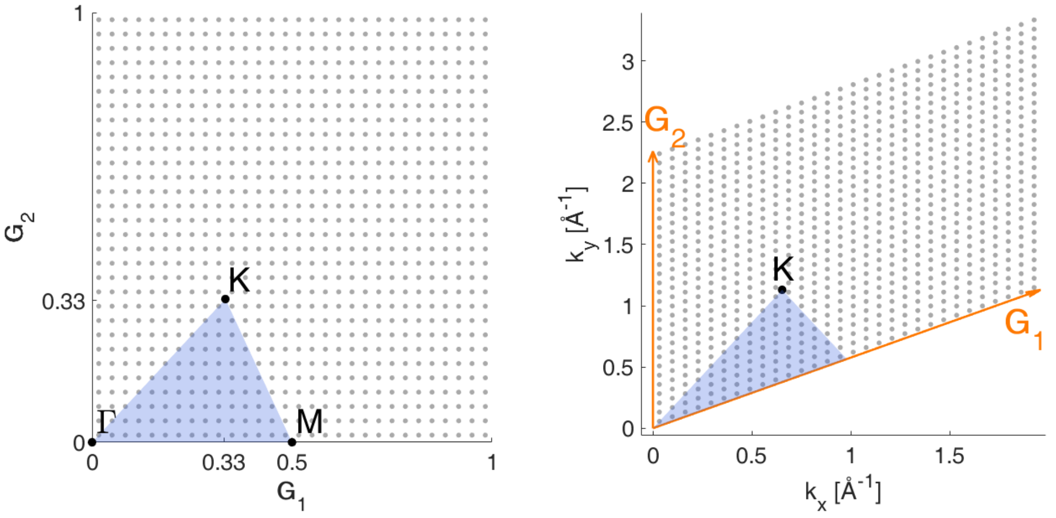

(a) (b)

Figure 3.1.1: (a) A 30 × 30 grid in the basis of the two reciprocal lattice vectors. (b) The same grid in reciprocal space.

functions in a planewave basis. As such, the pseudo wave basis is on the form

$$|\tilde{\psi}_{n\mathbf{k}}\rangle = \frac{1}{\sqrt{\Omega}}\frac{1}{\sqrt{\zeta_{n\mathbf{k}}}}\sum_{\mathbf{G}}\overline{C}_{n\mathbf{k}}(\mathbf{G})\mathrm{e}^{i(\mathbf{k}+\mathbf{G})\cdot\mathbf{r}}, \tag{3.1.1}$$

where n denotes the band, $\mathbf{G}$ is a linear superposition of the reciprocal lattice vectors and $\mathbf{k}$ denotes the k-vector. $\Omega^{-1/2}$ is a volumetric normalisation factor, and $\zeta_{n\mathbf{k}}^{-1/2}$ represents a normalisation of the non-normalised plane wave coefficients, $\overline{C}_{n\mathbf{k}}(\mathbf{G})$. More on this in section 3.1.2.

Clearly, it would be numerically impossible to expand the pesudo wave functions in a complete basis of plane waves, so a cut-off energy must be chosen. Naturally, this energy should be chosen in such a way, that the wave functions have converged. In figure 3.1.2a, the $\mathbf{G}$-vectors are represented as dots, which form a sphere in reciprocal space. In figure 3.1.2b, $\sum_{\mathbf{k}}|C_{n\mathbf{k}}(\mathbf{G})|$ is plotted against the absolute value of the corresponding $\mathbf{G}$.

The DFT calculation performed by GPAW includes a number of convergence criteria which are performed throughout the cycle, and which can be tuned. Throughout this report, all DFT calculations are performed using the default convergence parameters, which are as follows:

- The energy change for the last three iterations should be less than 0.5 meV per valence electron.
- The integrated absolute value of the change in density should be less than 0.0001 electrons per valence electron.
- The integrated value of the square of the residuals of the Kohn-Sham equations should be less than $4.0 \cdot 10^{-8}$ eV^2 per valence electron.

As mentioned, the lattice constants, and also the atomic positions in the unit cell, are retrieved by using C2DB. For MoS$_2$, this yields a lattice constant of $a = 3.184$ Å and a sulphur-sulphur distance of $b = 3.127$ Å. Along the edges of the irreducible element, which is depicted in figure 3.1.3a (which can be compared to figure 3.1.1), the corresponding band structure can be seen in figure 3.1.3b.

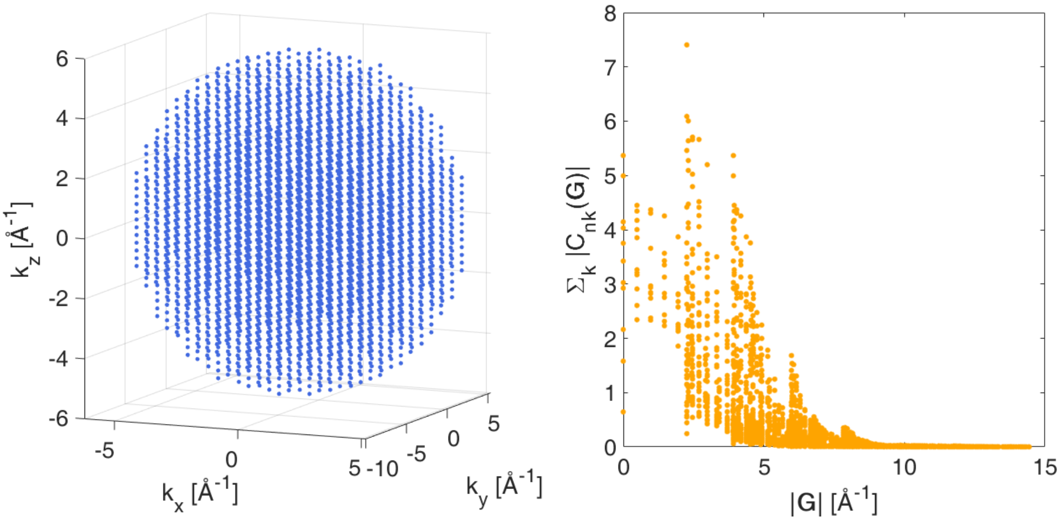

(a) (b)

Figure 3.1.2: DFT calculation for MoS_2 with 30×30 k-points and a cut-off energy of 450 eV. (a) The **G**-vectors represented as blue dots in reciprocal space, and (b) is the sum over k-vectors of the absolute value of the wave function for each **G**-vector used in the plane wave basis as a function of the distance from the Γ-point. Here, n spans seven valence bands and four conduction bands.

However, the band structure depicted here is without spin-orbit coupling included. Moreover, the current DFT calculation produces a bandgap of about 1.6 eV, which should be compared to an experimental value of 2.4 eV [27] and a C2DB value of 2.53 eV. In order to correct the bandgap, the conduction bands should be scissor-shifted by a value corresponding to the difference - in this case about 0.9 eV.

3.1.1 Obtaining Spin-Orbit Eigenvalues

Spin-orbit coupling can be included non-selfconsistently using the spin-orbit module of GPAW. In practise, it is done by first considering the full Hamiltonian in a basis of scalar-relativistic Kohn-Sham eigenstates [28], that is

$$\mathcal{H}_{nn'\sigma\sigma'}(\mathbf{k}) = \varepsilon_{n\sigma}\delta_{nn'}\delta_{\sigma\sigma'} + \langle\psi_{n\sigma}|\hat{h}_{SO}|\psi_{n'\sigma'}\rangle\,. \tag{3.1.2}$$

Since spin-orbit coupling is strongest close to the nuclei, the wave functions can be restricted to the regions inside the PAW-augmentation spheres [28]. In these regions, the wave functions can be expanded as

$$|\psi_{n\sigma}\rangle = \sum_{a,i}\langle\tilde{p}^a_{i\sigma}|\tilde{\psi}_{n\sigma}\rangle\,|\phi^a_{i\sigma}\rangle\,, \tag{3.1.3}$$

where $|\phi^a_{i\sigma}\rangle$ are the all-electron partial waves, $|\tilde{p}^a_{i\sigma}\rangle$ are their dual projectors, and $|\tilde{\psi}_{n\sigma}\rangle$ are the smooth pseudo wave functions, which were also described in section A.2. This turns equation (3.1.2) into

$$\mathcal{H}_{nn'\sigma\sigma'}(\mathbf{k}) = \varepsilon_{n\sigma}\delta_{nn'}\delta_{\sigma\sigma'} + \sum_a\sum_{i,j}\langle\tilde{p}^a_{i\sigma}|\tilde{\psi}_{n\sigma}\rangle^*\langle\tilde{p}^a_{j\sigma'}|\tilde{\psi}_{n'\sigma'}\rangle\langle\phi^a_{i\sigma}|\hat{h}_{SO}|\phi^a_{j\sigma'}\rangle\,. \tag{3.1.4}$$

The spin-orbit module returns both the spin-orbit eigenvalues but also the spin-orbit projection along the z-axis. In addition, the module also includes a function for calculating the term

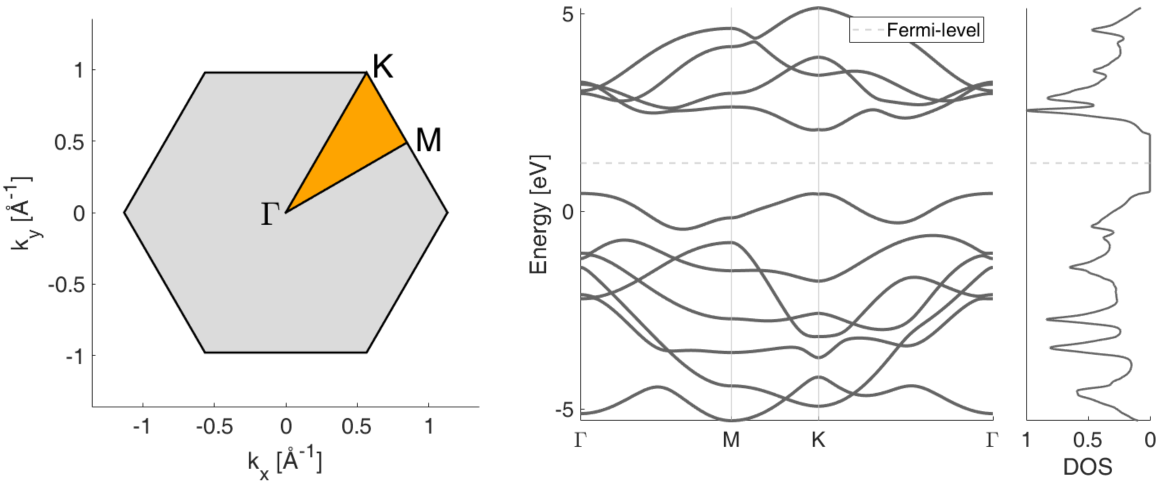

(a) (b)

Figure 3.1.3: (a) The Brillouin zone in gray and the irreducible element in orange, and (b) the band structure of MoS_2 without spin-orbit interactions showing a bandgap of approximately 1.6 eV along with the density of states.

$\langle \phi^a_{i\sigma}|\hat{h}_{SO}|\phi^a_{j\sigma'}\rangle$, which is useful for calculating the spin-orbit coupling in the BSE, as seen in section 3.3.2.

3.1.2 Orthonormalisation of the Wave Functions

When plane wave coefficients of the pseudo waves are extracted from GPAW, they are not represented in a way that orthonormalises the true wave functions. Orthonomalisation of the true wave functions clearly requires that

$$\langle \psi_{n\mathbf{k}}|\psi_{n'\mathbf{k}'}\rangle = \delta_{nn'}\delta_{\mathbf{k}\mathbf{k}'}, \quad |\psi_{n\mathbf{k}}\rangle = |\tilde{\psi}_{n\mathbf{k}}\rangle + \sum_a \sum_i \Big(\phi^a_i(\mathbf{r}) - \tilde{\phi}^a_i(\mathbf{r})\Big) \langle \tilde{p}^a_i|\tilde{\psi}_{n\mathbf{k}}\rangle\,. \tag{3.1.5}$$

The pseudo wave functions are on the form

$$|\tilde{\psi}_{n\mathbf{k}}\rangle = \frac{1}{\sqrt{\Omega}}\frac{1}{\sqrt{\zeta_{n\mathbf{k}}}}\sum_{\mathbf{G}} \overline{C}_{n\mathbf{k}}(\mathbf{G})\mathrm{e}^{i(\mathbf{G}+\mathbf{k})\cdot\mathbf{r}}. \tag{3.1.6}$$

If $\zeta_{n\mathbf{k}}^{-1/2}$ is removed, the pseudo waves do not meet the orthonormalisation criteria of the true waves in equation (3.1.5). The bar over the plane wave coefficients is meant to indicate this fact, and these coefficients are what GPAW outputs.

In the PAW formalism, the operator matrix element of a local operator is given by equation (A.2.19). Finding the overlap between wave functions corresponds to setting $\hat{O} = 1$ in equation (A.2.19), which leads to

$$\begin{aligned}
\langle \psi_{n\mathbf{k}}|\psi_{n'\mathbf{k}'}\rangle &= \langle \tilde{\psi}_{n\mathbf{k}}|\tilde{\psi}_{n'\mathbf{k}'}\rangle + \sum_a \sum_{i,j} \langle \tilde{p}^a_i|\tilde{\psi}_{n\mathbf{k}}\rangle^* \langle \tilde{p}^a_j|\tilde{\psi}_{n'\mathbf{k}'}\rangle \Big(\langle \phi^a_i|\phi^a_j\rangle - \langle \tilde{\phi}^a_i|\tilde{\phi}^a_j\rangle\Big) && (3.1.7)\\
&= \langle \tilde{\psi}_{n\mathbf{k}}|\tilde{\psi}_{n'\mathbf{k}'}\rangle + \tilde{O}_{nn',\mathbf{k}\mathbf{k}'} && (3.1.8)\\
&= \delta_{nn'\mathbf{k}\mathbf{k}'}, && (3.1.9)
\end{aligned}$$

where $\tilde{O}_{nn',\mathbf{k}\mathbf{k}'}$ holds the PAW corrections terms. Setting $n' = n$, $\mathbf{k}' = \mathbf{k}$ and subtracting $\tilde{O}_{nn',\mathbf{k}\mathbf{k}'}$ on both sides leads to

$$1 - \tilde{O}_{nn,\mathbf{k}\mathbf{k}} = \frac{1}{\Omega}\frac{1}{\zeta_{n\mathbf{k}}}\int \Big(\sum_{\mathbf{G}} \overline{C}^*_{n\mathbf{k}}(\mathbf{G})\mathrm{e}^{i(\mathbf{G}+\mathbf{k})\cdot\mathbf{r}}\Big)\Big(\sum_{\mathbf{G}'} \overline{C}_{n\mathbf{k}}(\mathbf{G}')\mathrm{e}^{i(\mathbf{G}'+\mathbf{k})\cdot\mathbf{r}}\Big) d\mathbf{r} \tag{3.1.10}$$

$$= \frac{1}{\Omega}\frac{1}{\zeta_{n\mathbf{k}}}\sum_{\mathbf{G}}\sum_{\mathbf{G}'} \overline{C}^*_{n\mathbf{k}}(\mathbf{G})\overline{C}_{n\mathbf{k}}(\mathbf{G}')\delta(\mathbf{G}' - \mathbf{G}) \tag{3.1.11}$$

$$= \frac{1}{\zeta_{n\mathbf{k}}}\sum_{\mathbf{G}} |\overline{C}^*_{n\mathbf{k}}(\mathbf{G})|^2, \tag{3.1.12}$$

where the last expression is found by combining $\Omega^{-1/2}$ with the Dirac delta function to create the Kronecker delta, $\delta_{\mathbf{G}',\mathbf{G}}$. Ultimately, this means we can rewrite the pseudo waves as

$$|\tilde{\psi}_{n\mathbf{k}}\rangle = \frac{1}{\sqrt{\Omega}}\sum_{\mathbf{G}} C_{n\mathbf{k}}(\mathbf{G})\mathrm{e}^{i(\mathbf{G}+\mathbf{k})\cdot\mathbf{r}}, \quad C_{n\mathbf{k}}(\mathbf{G}) = \overline{C}_{n\mathbf{k}}(\mathbf{G})\sqrt{\frac{1 - \tilde{O}_{nn,\mathbf{k}\mathbf{k}}}{\sum_{\mathbf{G}} |\overline{C}_{n\mathbf{k}}(\mathbf{G})|^2}}. \tag{3.1.13}$$

3.2 Momentum Matrix Elements from a Plane Wave Basis with PAW-Terms

In this section, we will discuss how to calculate momentum matrix elements using a plane wave basis. This will prove useful when calculating the excitonic momentum seen in equation (2.3.106) and the electric susceptibility seen in equation (2.3.94). The pseudo wave functions can be written as

$$|\tilde{\psi}_{n\mathbf{k}}\rangle = \frac{1}{\sqrt{\Omega}}\sum_{\mathbf{G}} C_{n\mathbf{k}}(\mathbf{G})\mathrm{e}^{i(\mathbf{G}+\mathbf{k})\cdot\mathbf{r}}. \tag{3.2.1}$$

The $\mathbf{k}$-vectors are two-dimensional, and $\mathbf{k}' = \mathbf{k} + \mathbf{Q}$, where $\mathbf{Q}$ is also two-dimensional. The momentum matrix elements are on the form

$$\langle\psi_{v\mathbf{k}}|\hat{\mathbf{p}}(\mathbf{q})|\psi_{c\mathbf{k}'}\rangle = \langle\psi_{v\mathbf{k}}\,|\,\tfrac{1}{2}\{\hat{\mathbf{p}}\mathrm{e}^{-i(\mathbf{q}_\parallel\cdot\mathbf{r}+q_z z)} + \mathrm{e}^{-i(\mathbf{q}_\parallel\cdot\mathbf{r}+q_z z)}\hat{\mathbf{p}}\}\,|\,\psi_{c\mathbf{k}'}\rangle\,\delta_{q_x,Q_x}\delta_{q_y,Q_y}. \tag{3.2.2}$$

For ease of notation, the Kronecker deltas will be removed by setting $\mathbf{Q} = \mathbf{q}_\parallel$, where $\mathbf{q}_\parallel$ is the component of $\mathbf{q}$ parallel to the material plane. Naturally, this also means that $\mathbf{k}' = \mathbf{k} + \mathbf{q}_\parallel$, and the momentum matrix elements take the form

$$\langle\psi_{v\mathbf{k}}|\hat{\mathbf{p}}(\mathbf{q})|\psi_{c\mathbf{k}'}\rangle = \frac{1}{2}\langle\psi_{v\mathbf{k}}\,|\,\hat{\mathbf{p}}\mathrm{e}^{-i(\mathbf{q}_\parallel\cdot\mathbf{r}+q_z z)} + \mathrm{e}^{-i(\mathbf{q}_\parallel\cdot\mathbf{r}+q_z z)}\hat{\mathbf{p}}\,|\,\psi_{c\mathbf{k}'}\rangle \tag{3.2.3}$$

$$= -\frac{\hbar}{2}\langle\psi_{v\mathbf{k}}|\mathbf{q}\mathrm{e}^{-i(\mathbf{q}_\parallel\cdot\mathbf{r}+q_z z)}|\psi_{c\mathbf{k}'}\rangle - i\hbar\langle\psi_{v\mathbf{k}}|\mathrm{e}^{-i(\mathbf{q}_\parallel\cdot\mathbf{r}+q_z z)}\boldsymbol{\nabla}|\psi_{c\mathbf{k}'}\rangle. \tag{3.2.4}$$

From here, each term can be written in the PAW formalism using equation (A.2.19), that is

$$\langle\psi_n|\hat{O}|\psi_{n'}\rangle = \langle\tilde{\psi}_n|\hat{O}|\tilde{\psi}_{n'}\rangle + \sum_a\sum_{i,j}\langle\tilde{p}^a_i|\tilde{\psi}_n\rangle^*\langle\tilde{p}^a_j|\tilde{\psi}_{n'}\rangle\Big(\langle\phi^a_i|\hat{O}|\phi^a_j\rangle - \langle\tilde{\phi}^a_i|\hat{O}|\tilde{\phi}^a_j\rangle\Big). \tag{3.2.5}$$

For ease of notation, the momentum matrix elements will be written as a sum of its pseudo wave part (denoted PS) and its PAW correction in agreement with equation (3.2.5), that is

$$\langle\psi_{v\mathbf{k}}|\hat{\mathbf{p}}(\mathbf{q})|\psi_{c\mathbf{k}'}\rangle = \langle\psi_{v\mathbf{k}}|\hat{\mathbf{p}}(\mathbf{q})|\psi_{c\mathbf{k}'}\rangle_{PS} + \langle\psi_{v\mathbf{k}}|\hat{\mathbf{p}}(\mathbf{q})|\psi_{c\mathbf{k}'}\rangle_{PAW}. \tag{3.2.6}$$

First, consider the pseudo part of the momentum matrix elements, which can be rewritten as

$$\begin{aligned}
&\langle \psi_{v\mathbf{k}} | \hat{\mathbf{p}}(\mathbf{q}) | \psi_{c\mathbf{k}'} \rangle_{PS} \\
&= -\frac{\hbar}{2} \langle \tilde{\psi}_{v\mathbf{k}} | \mathbf{q} \mathrm{e}^{-i(\mathbf{q}_{\parallel} \cdot \mathbf{r} + q_z z)} | \tilde{\psi}_{c\mathbf{k}'} \rangle - i\hbar \langle \tilde{\psi}_{v\mathbf{k}} | \mathrm{e}^{-i(\mathbf{q}_{\parallel} \cdot \mathbf{r} + q_z z)} \boldsymbol{\nabla} | \tilde{\psi}_{c\mathbf{k}'} \rangle \qquad (3.2.7) \\
&= \frac{\hbar}{\Omega_{uc}} \sum_{\mathbf{G}} \sum_{\mathbf{G}'} \langle C_{v\mathbf{k}}(\mathbf{G}) \mathrm{e}^{i(\mathbf{k}+\mathbf{G})\cdot\mathbf{r}} | (\mathbf{G}' + \mathbf{k}' - \tfrac{\mathbf{q}}{2}) \mathrm{e}^{-i(\mathbf{q}_{\parallel} \cdot \mathbf{r} + q_z z)} | C_{c\mathbf{k}'}(\mathbf{G}') \mathrm{e}^{i(\mathbf{k}'+\mathbf{G}')\cdot\mathbf{r}} \rangle \qquad (3.2.8) \\
&= \frac{\hbar}{L_z} \sum_{\mathbf{G}} \sum_{\mathbf{G}'} C^*_{v\mathbf{k}}(\mathbf{G}) C_{c\mathbf{k}'}(\mathbf{G}') (\mathbf{G}' + \mathbf{k} + \tfrac{\mathbf{q}}{2}) \delta_{G'_x, G_x} \delta_{G'_y, G_y} \int \mathrm{e}^{i(G'_z - G_z - q_z)z} dz. \qquad (3.2.9)
\end{aligned}$$

The z-integral is a bit more complicated than the in-plane ones. In GPAW, the unit cell is structured such that the height is composed of a vacuum plus the thickness of the layer. In this project we have used a vacuum parameter of 6 Å. The thickness of the layer is about 3.2 Å, so the total height of the unit cell is about 15.2 Å. Whatever this height may be, it will be denoted as Λ, and it is illustrated in figure 3.2.1. GPAW structures the unit cell, such that the structure is centered in the interval $(0, \Lambda)$, and therefore the z-integral should be evaluated in the same limit. This reduces the pseudo part of the momentum matrix element to

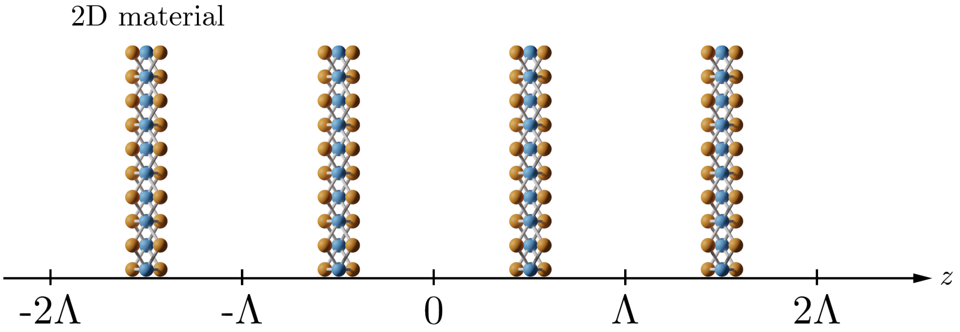

Figure 3.2.1: This figure shows the virtual periodicity between the 2D layers, that GPAW uses in its Fourier transform along the z-axis.

$$\begin{aligned}
\langle \psi_{v\mathbf{k}} | \hat{\mathbf{p}}(\mathbf{q}) | \psi_{c\mathbf{k}'} \rangle_{PS} = \frac{\hbar}{i\Lambda} &\sum_{G_x, G_y, G_z} \sum_{G'_z} C^*_{v\mathbf{k}}(G_x, G_y, G_z) C_{c\mathbf{k}'}(G_x, G_y, G'_z) \\
&\times (\hat{x} G_x + \hat{y} G_y + \hat{z} G'_z + \mathbf{k} + \tfrac{\mathbf{q}}{2}) \frac{\mathrm{e}^{-iq_z\Lambda}}{G'_z - G_z - q_z}.
\end{aligned} \qquad (3.2.10)$$

Now, we may denote $\mathbf{G} = (G_x, G_y, G_z)$, and $\mathbf{G}' := (G_x, G_y, G'_z)$. Moreover, since we denote $\Delta G_z = G'_z - G_z$, it is clear that $\Delta G_z = 2\pi n/\Lambda$ where $n \in \mathbb{Z}$. With these notations, we can simplify the expression to

$$\langle \psi_{v\mathbf{k}} | \hat{\mathbf{p}}(\mathbf{q}) | \psi_{c\mathbf{k}'} \rangle_{PS} = \frac{\hbar}{i\Lambda} \sum_{G_x, G_y, G_z} \sum_{G'_z} C^*_{v\mathbf{k}}(\mathbf{G}) C_{c\mathbf{k}'}(\mathbf{G}') (\mathbf{G}' + \mathbf{k} + \tfrac{\mathbf{q}}{2}) \frac{\mathrm{e}^{-iq_z\Lambda}}{\Delta G_z - q_z}. \qquad (3.2.11)$$

From here, the PAW terms of the momentum matrix elements should be considered. They are given as

$$\begin{aligned}
&\langle \psi_{v\mathbf{k}} | \hat{\mathbf{p}}(\mathbf{q}) | \psi_{c\mathbf{k}'} \rangle_{PAW} \\
&= -\frac{\hbar\mathbf{q}}{2} \sum_a \sum_{i,j} \langle \tilde{p}^a_i | \tilde{\psi}_{v\mathbf{k}} \rangle^* \langle \tilde{p}^a_j | \tilde{\psi}_{c\mathbf{k}'} \rangle \Big(\langle \phi^a_i | \mathrm{e}^{-i(\mathbf{q}_{\parallel} \cdot \mathbf{r} + q_z z)} | \phi^a_j \rangle - \langle \tilde{\phi}^a_i | \mathrm{e}^{-i(\mathbf{q}_{\parallel} \cdot \mathbf{r} + q_z z)} | \tilde{\phi}^a_j \rangle \Big) \\
&- i\hbar \sum_a \sum_{i,j} \langle \tilde{p}^a_i | \tilde{\psi}_{v\mathbf{k}} \rangle^* \langle \tilde{p}^a_j | \tilde{\psi}_{c\mathbf{k}'} \rangle \Big(\langle \phi^a_i | \mathrm{e}^{-i(\mathbf{q}_{\parallel} \cdot \mathbf{r} + q_z z)} \boldsymbol{\nabla} | \phi^a_j \rangle - \langle \tilde{\phi}^a_i | \mathrm{e}^{-i(\mathbf{q}_{\parallel} \cdot \mathbf{r} + q_z z)} \boldsymbol{\nabla} | \tilde{\phi}^a_j \rangle \Big).
\end{aligned} \qquad (3.2.12)$$

However, in order to implement this numerically, we do not discretise $\mathbf{q}$ in three dimensions. Instead, only $\mathbf{q}_{||}$ is used, and we calculate q_z by

$$q_z = \sqrt{\frac{\omega^2}{c^2} - |\mathbf{q}_{||}|^2}. \tag{3.2.13}$$

Moreover, ω can be assumed constant for the spontaneous emission calculations seen in section 3.5, since we mostly consider the lowest exciton, that is exciton A. Lastly, the wave functions and corresponding energies calculated in this report are found using a technique, that doesn't incorporate non-local effects, as opposed to a GW-calculation. In order to correct the momentum matrix elements, the following substitution should then be made [29–33]

$$\langle \psi_{v\mathbf{k}} | \hat{\mathbf{p}}(\mathbf{q}) | \psi_{c\mathbf{k}'} \rangle \rightarrow \langle \psi_{v\mathbf{k}} | \hat{\mathbf{p}}(\mathbf{q}) | \psi_{c\mathbf{k}'} \rangle \frac{E^{GW}_{c,\mathbf{k}'} - E^{GW}_{v,\mathbf{k}}}{E^{DFT}_{c,\mathbf{k}'} - E^{DFT}_{v,\mathbf{k}}}, \tag{3.2.14}$$

where DFT denotes the energies corresponding to a non scissor-shifted DFT calculation, and GW denotes the energies of a GW-calculation (in our case, the scissor-shifted energies).

3.3 Bethe-Salpeter in a Plane-Wave Basis with PAW-Terms

To describe the excitonic properties, this section will concern itself with numerically solving the BSE for 2D semiconductors. The first step will be to calculate the Coulomb (direct) and exchange (indirect) kernel in the basis of planewaves with PAW-corrections. Following this, the matrix equation including spin-orbit will be introduced as well as the excitonic momentum elements in regards to the optical response. Finally, some numerical detail of the calculations which where performed in this project will be presented.

3.3.1 The Coulomb and Exchange Kernel

As seen in equation (3.2.1), the true wave functions can be decomposed into a lattice periodic part and a phase part. The lattice periodic part can be found as

$$u_{n\mathbf{k}}(\mathbf{r}) = \psi_{n\mathbf{k}}(\mathbf{r}) \mathrm{e}^{-i\mathbf{k}\cdot\mathbf{r}}. \tag{3.3.1}$$

In order to calculate the Coulomb and exchange kernel of the BSE, the next step is to Fourier decompose the product

$$\begin{aligned} u^*_{n\mathbf{k}}(\mathbf{r}) u_{m\mathbf{k}'}(\mathbf{r}) &= \psi^*_{n\mathbf{k}}(\mathbf{r}) \mathrm{e}^{i(\mathbf{k}-\mathbf{k}')\cdot\mathbf{r}} \psi_{m\mathbf{k}'}(\mathbf{r}) && (3.3.2) \\ &= \sum_{\mathbf{G}} I_{n\mathbf{k},m\mathbf{k}'}(\mathbf{G}) \mathrm{e}^{i\mathbf{G}\cdot\mathbf{r}}. && (3.3.3) \end{aligned}$$

As such, the Fourier coefficients of the above expansion can be calculated as

$$\begin{aligned} I_{n\mathbf{k},m\mathbf{k}'}(\mathbf{G}) &= \frac{1}{\Omega_{\mathrm{uc}}} \int_{\mathrm{uc}} \psi^*_{n\mathbf{k}} \mathrm{e}^{i(\mathbf{k}-\mathbf{k}'-\mathbf{G})\cdot\mathbf{r}} \psi_{m\mathbf{k}'} d\mathbf{r} && (3.3.4) \\ &= \frac{1}{\Omega} \int \psi^*_{n\mathbf{k}} \mathrm{e}^{i(\mathbf{k}-\mathbf{k}'-\mathbf{G})\cdot\mathbf{r}} \psi_{m\mathbf{k}'} d\mathbf{r}, && (3.3.5) \end{aligned}$$

where the latter integral is taken over all space and the volume is correspondingly large, while both are still confined to multiples of the unit cell. Now, since $\mathrm{e}^{i(\mathbf{k}-\mathbf{k}'-\mathbf{G})\cdot\mathbf{r}}$ is a local operator, equation (A.2.19) can be used. The integral then becomes

$$\begin{aligned}
I_{n\mathbf{k},m\mathbf{k}'}(\mathbf{G}) &= \frac{1}{\Omega}\langle\psi_{n\mathbf{k}}|\mathrm{e}^{i(\mathbf{k}-\mathbf{k}'-\mathbf{G})\cdot\mathbf{r}}|\psi_{m\mathbf{k}'}\rangle \qquad (3.3.6)\\
&= \frac{1}{\Omega}\Big[\sum_{\mathbf{G}'} C^*_{n\mathbf{k}}(\mathbf{G}'-\mathbf{G})C_{m\mathbf{k}'}(\mathbf{G}')\\
&+\sum_{a}\sum_{i_1 i_2}\langle\tilde{p}^a_i|\tilde{\psi}_{n\mathbf{k}}\rangle^*\langle\tilde{p}^a_i|\tilde{\psi}_{m\mathbf{k}'}\rangle\Big(\langle\phi^a_{i_1}|\mathrm{e}^{i(\mathbf{k}-\mathbf{k}'-\mathbf{G})\cdot\mathbf{r}}|\phi^a_{i_2}\rangle-\langle\tilde{\phi}^a_{i_1}|\mathrm{e}^{i(\mathbf{k}-\mathbf{k}'-\mathbf{G})\cdot\mathbf{r}}|\tilde{\phi}^a_{i_2}\rangle\Big)\Big]. \qquad (3.3.7)
\end{aligned}$$

Likewise, the potential W is also expanded, however, only in 2D Fourier components as

$$W(\mathbf{r},\mathbf{r}') = \sum_{\boldsymbol{\kappa}_\parallel,\mathbf{G}_\parallel} w(\boldsymbol{\kappa}_\parallel+\mathbf{G}_\parallel)\mathrm{e}^{i(\boldsymbol{\kappa}_\parallel+\mathbf{G}_\parallel)\cdot(\mathbf{r}-\mathbf{r}')}, \qquad (3.3.8)$$

with $\boldsymbol{\kappa}_\parallel$ limited to the first Brillouin zone. The Coulomb or exchange kernel can now be written as

$$\begin{aligned}
\big\langle\psi_{\alpha,\mathbf{k}_\alpha}\psi_{\gamma,\mathbf{k}_\gamma}\,\big|\,W(\mathbf{r},\mathbf{r}')\,\big|\,\psi_{\beta,\mathbf{k}_\beta}\psi_{\delta,\mathbf{k}_\delta}\big\rangle &= \sum_{\boldsymbol{\kappa}_\parallel,\mathbf{G}_\parallel}\sum_{\mathbf{G}_{\alpha,\beta},\mathbf{G}_{\gamma,\delta}} w(\boldsymbol{\kappa}_\parallel+\mathbf{G}_\parallel)I_{\alpha\mathbf{k}_\alpha,\beta\mathbf{k}_\beta}(\mathbf{G}_{\alpha,\beta})I_{\gamma\mathbf{k}_\gamma,\delta\mathbf{k}_\delta}(\mathbf{G}_{\gamma,\delta})\\
&\times\int\!\!\int \mathrm{e}^{i(\mathbf{k}_\beta-\mathbf{k}_\alpha+\mathbf{G}_{\alpha\beta}+\boldsymbol{\kappa}_\parallel+\mathbf{G}_\parallel)\cdot\mathbf{r}}\mathrm{e}^{i(\mathbf{k}_\delta-\mathbf{k}_\gamma+\mathbf{G}_{\gamma\delta}-\boldsymbol{\kappa}_\parallel-\mathbf{G}_\parallel)\cdot\mathbf{r}'}d^3\mathbf{r}d^3\mathbf{r}', \qquad (3.3.9)
\end{aligned}$$

where the integrals demands $\mathbf{G}_{\alpha\beta}$ and $\mathbf{G}_{\gamma\delta}$ to have a z-component equal to zero, since the potential $W(\mathbf{r},\mathbf{r}')$ has been expanded in 2D. The only terms of the sum, which will yield a non-zero result are those who satisfies both these conditions:

$$\begin{aligned}
\mathbf{k}_\beta-\mathbf{k}_\alpha+\mathbf{G}_{\alpha\beta}+\boldsymbol{\kappa}_\parallel+\mathbf{G}_\parallel &= 0,\\
\mathbf{k}_\delta-\mathbf{k}_\gamma+\mathbf{G}_{\gamma\delta}-\boldsymbol{\kappa}_\parallel-\mathbf{G}_\parallel &= 0.
\end{aligned} \qquad (3.3.10)$$

The limitation of $\boldsymbol{\kappa}_\parallel$ being restrained to the Brillouin zone, results in $\boldsymbol{\kappa}_\parallel$ cancelling with the $\mathbf{k}$'s, yielding

$$\begin{aligned}
(\mathbf{k}_\alpha-\mathbf{k}_\beta) &= \boldsymbol{\kappa}_\parallel = (\mathbf{k}_\delta-\mathbf{k}_\gamma),\\
\mathbf{G}_{\alpha\beta} &= -\mathbf{G}_\parallel \quad\text{and}\quad \mathbf{G}_{\gamma\delta} = \mathbf{G}_\parallel.
\end{aligned} \qquad (3.3.11)$$

By defining $V_{\alpha\beta\gamma\delta} := \big\langle\psi_{\alpha,\mathbf{k}_\alpha}\psi_{\gamma,\mathbf{k}_\gamma}\,\big|\,W(\mathbf{r},\mathbf{r}')\,\big|\,\psi_{\beta,\mathbf{k}_\beta}\psi_{\delta,\mathbf{k}_\delta}\big\rangle$, $\mathbf{G} := \mathbf{G}_\parallel$, and $\boldsymbol{\kappa} := \boldsymbol{\kappa}_\parallel$, equation (3.3.9) now becomes

$$V_{\alpha\beta,\gamma\delta} = \Omega^2\sum_{\mathbf{G}} w(\boldsymbol{\kappa}+\mathbf{G})I_{\alpha\mathbf{k}_\alpha,\beta\mathbf{k}_\beta}(-\mathbf{G})I_{\gamma\mathbf{k}_\gamma,\delta\mathbf{k}_\delta}(\mathbf{G}). \qquad (3.3.12)$$

Now, for the Coulomb potential, α and β will be the valence bands v' and v, respectively, while γ and δ will be c and c', respectively. Setting $\boldsymbol{\kappa} = \mathbf{k}'-\mathbf{k}$, the potential becomes

$$V^{Cou}_{v'v,cc'} = \Omega^2\sum_{\mathbf{G}} w_{Cou}(\boldsymbol{\kappa}+\mathbf{G})I_{v'\mathbf{k}',v\mathbf{k}}(-\mathbf{G})I_{c\mathbf{k},c'\mathbf{k}'}(\mathbf{G}). \qquad (3.3.13)$$

For the exchange potential, α and γ are the valence bands and β and δ are the conduction bands. This consequently means the Bloch phases will vanish, since $\mathbf{k}_\alpha = \mathbf{k}_\beta$ and $\mathbf{k}_\gamma = \mathbf{k}_\delta$, such that $\boldsymbol{\kappa} = 0$. For the exchange integral the term with $\mathbf{G} = 0$ can advantageously be removed from the sum, improving numerical stability, meaning the exchange matrix elements becomes,

$$V^{exc}_{v'c',cv} = \Omega^2\sum_{\mathbf{G}\neq 0} w_{exc}(\mathbf{G})I_{v'\mathbf{k}',c'\mathbf{k}'}(-\mathbf{G})I_{c\mathbf{k},v\mathbf{k}}(\mathbf{G}). \qquad (3.3.14)$$

It's worth noticing that $I_{\alpha\mathbf{k}_\alpha,\beta\mathbf{k}_\beta}(-\mathbf{G}) = I^*_{\beta\mathbf{k}_\beta,\alpha\mathbf{k}_\alpha}(\mathbf{G})$. In the case of only looking at singlet states, that is ignoring spin-orbit coupling, the Hamiltonian matrix elements can be determined by [22, eq. 18.4]. Inserting the Coulomb and exchange kernels then gives

$$\begin{aligned} H_{\mathbf{k},\mathbf{k}'} =& E^{(\mathbf{k},\mathbf{k}')}_{cc'vv'} - \Omega^2 \sum_{\mathbf{G}} I_{v'\mathbf{k}',v\mathbf{k}}(-\mathbf{G}) I_{c\mathbf{k},c'\mathbf{k}'}(\mathbf{G}) w_{Cou}(\mathbf{k}-\mathbf{k}'+\mathbf{G}) \\ &+ 2\Omega^2 \sum_{\mathbf{G}\neq 0} I_{v'\mathbf{k}',c'\mathbf{k}'}(-\mathbf{G}) I_{c\mathbf{k},v\mathbf{k}}(\mathbf{G}) w_{exc}(\mathbf{G}), \end{aligned} \tag{3.3.15}$$

where $E^{(\mathbf{k},\mathbf{k}')}_{i'ijj'} = (\tilde{E}^{j'}_j(\mathbf{k}) - \tilde{E}^{i}_{i'}(\mathbf{k}))\delta_{\mathbf{k},\mathbf{k}'}\delta_{i,i'}\delta_{j,j'}$. Furthermore, one can easily introduce here the two band approximation, $v' = v$ and $c' = c$.

3.3.2 Including Spin-Orbit in the Bethe-Salpeter Equation

The SO-BSE super matrix elements are given as equation (2.3.23), which in the formalism derived in this section is written as

$$\begin{bmatrix} E^{(\mathbf{k},\mathbf{k}')}_{v'_\uparrow v_\uparrow c_\uparrow c'_\uparrow} - V^{\text{Coul}}_{v'_\uparrow v_\uparrow c_\uparrow c'_\uparrow} + V^{\text{exc}}_{v'_\uparrow c'_\uparrow c_\uparrow v_\uparrow} & -\zeta^{(\mathbf{k},\mathbf{k}')}_{v'_\downarrow v_\uparrow c_\uparrow c'_\uparrow} & \zeta^{(\mathbf{k},\mathbf{k}')}_{c_\uparrow c'_\downarrow v'_\uparrow v_\uparrow} & V^{\text{exc}}_{v'_\downarrow c'_\downarrow c_\uparrow v_\uparrow} \\ -\zeta^{(\mathbf{k},\mathbf{k}')}_{v'_\uparrow v_\downarrow c_\uparrow c'_\uparrow} & E^{(\mathbf{k},\mathbf{k}')}_{v'_\downarrow v_\downarrow c_\uparrow c'_\uparrow} - V^{\text{Coul}}_{v'_\downarrow v_\downarrow c_\uparrow c'_\uparrow} & 0 & \zeta^{(\mathbf{k},\mathbf{k}')}_{c_\uparrow c'_\downarrow v'_\downarrow v_\downarrow} \\ \zeta^{(\mathbf{k},\mathbf{k}')}_{c_\downarrow c'_\uparrow v'_\uparrow v_\uparrow} & 0 & E^{(\mathbf{k},\mathbf{k}')}_{v'_\uparrow v_\uparrow c_\downarrow c'_\downarrow} - V^{\text{Coul}}_{v'_\uparrow v_\uparrow c_\downarrow c'_\downarrow} & -\zeta^{(\mathbf{k},\mathbf{k}')}_{v'_\downarrow v_\uparrow c_\downarrow c'_\downarrow} \\ V^{\text{exc}}_{v'_\uparrow c'_\uparrow c_\downarrow v_\downarrow} & \zeta^{(\mathbf{k},\mathbf{k}')}_{c_\downarrow c'_\uparrow v'_\downarrow v_\downarrow} & -\zeta^{(\mathbf{k},\mathbf{k}')}_{v'_\uparrow v_\downarrow c_\downarrow c'_\downarrow} & E^{(\mathbf{k},\mathbf{k}')}_{v'_\downarrow v_\downarrow c_\downarrow c'_\downarrow} - V^{\text{Coul}}_{v'_\downarrow v_\downarrow c_\downarrow c'_\downarrow} + V^{\text{exc}}_{v'_\downarrow c'_\downarrow c_\downarrow v_\downarrow} \end{bmatrix}, \tag{3.3.16}$$

where $\zeta^{(\mathbf{k},\mathbf{k}')}_{i'ijj'} = \langle i'|\hat{h}_{SO}|i\rangle\,\delta_{\mathbf{k}\mathbf{k}'}\delta_{jj'}$, with the braket being given as equation (3.1.4). Furthermore, the terms $E^{(\mathbf{k},\mathbf{k}')}_{i'ijj'}$ are defined as in equation (2.3.22), that is

$$E^{(\mathbf{k},\mathbf{k}')}_{i'ijj'} = \left[\left(\tilde{E}^{j'}_j(\mathbf{k}) - \tilde{E}^{i}_{i'}(\mathbf{k})\right)\delta_{i,i'}\delta_{j,j'} - \left\langle i' \,\middle|\, \hat{h}_{SO} \,\middle|\, i\right\rangle \delta_{j,j'} + \left\langle j \,\middle|\, \hat{h}_{SO} \,\middle|\, j'\right\rangle \delta_{i,i'}\right]\delta_{\mathbf{k},\mathbf{k}'}. \tag{3.3.17}$$

A consequence of including spin-orbit, is that one must include more bands of opposing parity for a good result, due to spin hybridisation. An example of this can be seen in figure 3.3.1b. When comparing with figure 3.3.1a, it is obvious that spin hybridisation is largest when two bands of differing parity intersect. Furthermore, it can be seen that there is little to no spin hybridisation around the K-valley for MoS_2.

3.3.3 Calculation of Exciton Momentum Matrix Elements and the Dielectric Response

With the use of the expression from equation (2.3.95), one can calculate the optical properties of a many-body system, if the single-particle momentum matrix elements are replaced by the many-body momentum matrix elements, given by the operator

$$\hat{\mathbf{P}} = \sum_\sigma \sum_{n=1}^{N} \hat{\mathbf{p}}_n(\mathbf{q}), \quad \hat{\mathbf{p}}_n(\mathbf{q}) = -\frac{i\hbar}{2}\left(\boldsymbol{\nabla}_n \mathrm{e}^{-i\mathbf{q}\cdot\mathbf{r}_n} + \mathrm{e}^{-i\mathbf{q}\cdot\mathbf{r}_n}\boldsymbol{\nabla}_n\right). \tag{3.3.18}$$

Since the many-body operator is just a sum over single-body operators and there is one difference between the ground state and each of the basis states, the momentum matrix elements can be written into a weighted sum

$$\langle 0|\hat{\mathbf{P}}|exc\rangle = \sum_{v,c,\mathbf{k}} \sum_{\sigma,\sigma'} \Psi^{c,\mathbf{k},\sigma'}_{v,\mathbf{k},\sigma} \langle v\mathbf{k}\sigma \,|\, \hat{\mathbf{p}}(\mathbf{q}) \,|\, c\mathbf{k}\sigma'\rangle\,\delta_{\sigma\sigma'}. \tag{3.3.19}$$

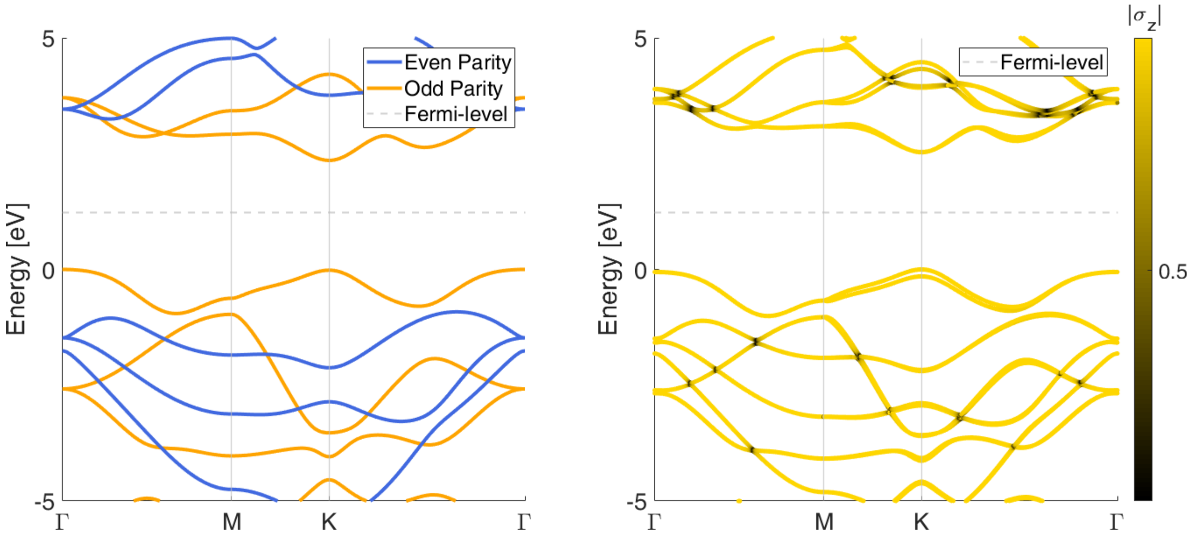

(a) (b)

Figure 3.3.1: (a) Band structure for MoS_2 excluding spin orbit but with parity displayed. (b) Band structure of MoS_2 with spin-orbit interaction. The shade of the graph represent the absolute value of the z-projection of the spin, $|\sigma_z|$. A low value for this, means that states of differing spin hybridise.

We have deliberately chosen not to resolve the spin Kronecker delta, such that the momentum elements match the basis of our BSE calculation. Naturally, for ease of notation one could resolve the σ'-sum using the Kronecker delta. The exciton wave function is normalized as

$$\sum_{v,c,\mathbf{k}} \sum_{\sigma,\sigma'} |\Psi^{c,\mathbf{k},\sigma'}_{v,\mathbf{k},\sigma}|^2 = 1. \tag{3.3.20}$$

Is is now possible to convert the true exciton wave function coefficients $\Psi^{c,\mathbf{k},\sigma'}_{v,\mathbf{k},\sigma}$, into the exciton wave coeffeicients for our chosen grid points, $\mathbf{k}'$. This is done with the usual conversion:

$$\sum_{v,c,\mathbf{k}} \sum_{\sigma,\sigma'} |\Psi^{c,\mathbf{k},\sigma'}_{v,\mathbf{k},\sigma}|^2 \simeq \frac{1}{(\Delta\mathbf{k})^2} \sum_{v,c} \sum_{\sigma,\sigma'} \int \left|\Psi^{c,\mathbf{k},\sigma'}_{v,\mathbf{k},\sigma}\right|^2 d^2k \simeq \frac{A}{(2\pi)^2} \sum_{v,c,\mathbf{k}'} \sum_{\sigma,\sigma'} \left|\Psi^{c,\mathbf{k}',\sigma'}_{v,\mathbf{k}',\sigma}\right|^2 \Delta k'_x \Delta k'_y. \tag{3.3.21}$$

This conversion emphasizes the importance of the chosen amount of k-points. Now, due to the normalisation of the calculated wave function on the k'-grid, we have

$$\sum_{v,c,\mathbf{k}'} \sum_{\sigma,\sigma'} \left|\alpha^{c,\mathbf{k}',\sigma'}_{v,\mathbf{k}',\sigma}\right|^2 = 1, \tag{3.3.22}$$

where $\alpha^{c,\mathbf{k}',\sigma'}_{v,\mathbf{k}',\sigma}$ is the coefficients calculated on the k'-grid. For ease of notation, we'll return to denoting k' as k, such that k now denotes our choice of k-point grid. Setting equation (3.3.21) equal to equation (3.3.22), and using that both sums run over $\mathbf{k}$, where the phase of the coefficients can be arbitrarily chosen, then

$$\Psi^{c,\mathbf{k},\sigma'}_{v,\mathbf{k},\sigma} = \sqrt{\frac{A}{(2\pi)^2}} \alpha^{c,\mathbf{k},\sigma'}_{v,\mathbf{k},\sigma} \sqrt{\Delta k_x \Delta k_y}. \tag{3.3.23}$$

This then turns equation (3.3.19) into

$$\mathbf{P}_{exc} := \langle 0|\hat{\mathbf{P}}|exc\rangle = \sqrt{\frac{A}{(2\pi)^2}} \sum_{v,c,\mathbf{k}} \sum_{\sigma,\sigma'} \alpha^{c,\mathbf{k},\sigma'}_{v,\mathbf{k},\sigma} \langle v_\mathbf{k}|\hat{\mathbf{p}}(\mathbf{q})|c_\mathbf{k}\rangle \delta_{\sigma\sigma'} \sqrt{\Delta k_x \Delta k_y}. \tag{3.3.24}$$

For the purpose of calculating the in-plane tensor components of the dielectric response, we need only the coordinates along x and y. Furthermore, we can approximate $q = 0$, such that

$$\langle 0|\hat{P}_{xy}|exc\rangle = \sqrt{\frac{A}{(2\pi)^2}} \sum_{v,c,\mathbf{k}} \sum_{\sigma,\sigma'} \alpha^{c,\mathbf{k},\sigma'}_{v,\mathbf{k},\sigma} \langle v_{\mathbf{k}}|\hat{p}_{xy}|c_{\mathbf{k}}\rangle \delta_{\sigma\sigma'} \sqrt{\Delta k_x \Delta k_y}, \tag{3.3.25}$$

where $\hat{p}_{xy}$ is either the x- or y-coordinate of the $\hat{\mathbf{p}}(\mathbf{q}) \to \hat{\mathbf{p}}(\mathbf{0})$ operator. Now, by taking the absolute square of equation (3.3.25), one will obtain

$$|\langle 0|\hat{P}_{xy}|exc\rangle|^2 = \frac{A}{4\pi^2} |P_{S,xy}|^2, \tag{3.3.26}$$

where

$$P_{S,xy} := \left| \sum_{v,c,\mathbf{k}} \sum_{\sigma,\sigma'} \alpha^{c,\mathbf{k},\sigma'}_{v,\mathbf{k},\sigma} \langle v_{\mathbf{k}}|\hat{p}_{xy}|c_{\mathbf{k}}\rangle \delta_{\sigma\sigma'} \right|^2 \Delta k_x \Delta k_y. \tag{3.3.27}$$

This means the susceptibility can be written as

$$\chi_{xx}(\omega) = \frac{e^2\hbar^2 A}{2\pi^2 \varepsilon_0 m^2 \Omega} \sum_S \frac{|P_{S,x}|^2}{E_S \left[E_S^2 - \hbar^2(\omega + i\Gamma)^2\right]}, \tag{3.3.28}$$

and since we are working with 2D materials, and are thus interested in the 2D susceptibility, A and Ω will now cancel. Furthermore, due to the symmetries of the TMDs in question, we require $\chi_{xx} = \chi_{yy}$, thus one can advantageously calculate the average of these in order to reduce numerical errors, that is

$$\chi_{xx,yy}(\omega) = \frac{e^2\hbar^2}{2\pi^2 \varepsilon_0 m^2} \sum_S \frac{|P_S|^2}{E_S \left[E_S^2 - \hbar^2(\omega + i\Gamma)^2\right]}, \tag{3.3.29}$$

where

$$|P_S|^2 = \frac{|P_{S,x}|^2 + |P_{S,y}|^2}{2}. \tag{3.3.30}$$

3.3.4 Numerical Detail Concerning the Bethe-Salpeter Equation

As seen in equation (3.3.7), it is necessary to calculate the product between plane wave coefficients, where one of the two has its argument shifted by an in-plane superposition of reciprocal lattice vectors. However, when using plane waves in GPAW for the pseudo wave functions, the plane wave bases at different k-points are not guaranteed to be the same. Explained in another way, the pseudo wave $|\tilde{\psi}_{m\mathbf{k}}\rangle$ consists of N plane waves, while $|\tilde{\psi}_{m\mathbf{k}'}\rangle$ constitutes N' plane waves. As such, to calculate the overlap between the states, they must be put in the same basis. This is implemented by first finding the unique $\mathbf{G}$'s collectively for the plane wave expansion of all pseudo waves. Then, each state is sorted to match this basis. If at a certain $\mathbf{G}$ the pseudo wave in question doesn't have a matching plane wave coefficient, the coefficient is simply defined to be zero. Another step, that some may choose to include in BSE calculations is to sort the states according to parity. The parity operator, $\hat{\Pi}_z$, can be defined as

$$\hat{\Pi}_z |\psi_{n\mathbf{k}}(x,y,z)\rangle = |\psi_{n\mathbf{k}}(x,y,-z)\rangle. \tag{3.3.31}$$

We only check for parity inversion of the z-coordinate, since states of opposite parity will be unable to have their in-plane dipole matrix elements couple, if $q_z = 0$. This is a good approximation, since the momentum of photons is very small. Naturally, we can only check the parity of the pseudo wave functions. However, the criterion of having either odd or even parity applies at every spacial coordinate, but outside the augmentation spheres the pseudo wave functions become the true wave function. As such, checking the parity of the pseudo wave functions is sufficient. Due to the parity operator having eigenvalue ± 1, numerically we merely need to check if the pseudo wave functions are odd or even with respect to z. In figure 3.3.1a, the parity-sorted band structure evaluated along the path $\Gamma \rightarrow \mathrm{M} \rightarrow \mathrm{K} \rightarrow \Gamma$ can be seen without spin-orbit included. If spin-orbit coupling is not included in the BSE calculation, the memory-usage and computation time can be severely reduced by including band parity. But, since the spin-orbit operator couples bands of differing parity as well, this is not a viable option in our calculations.

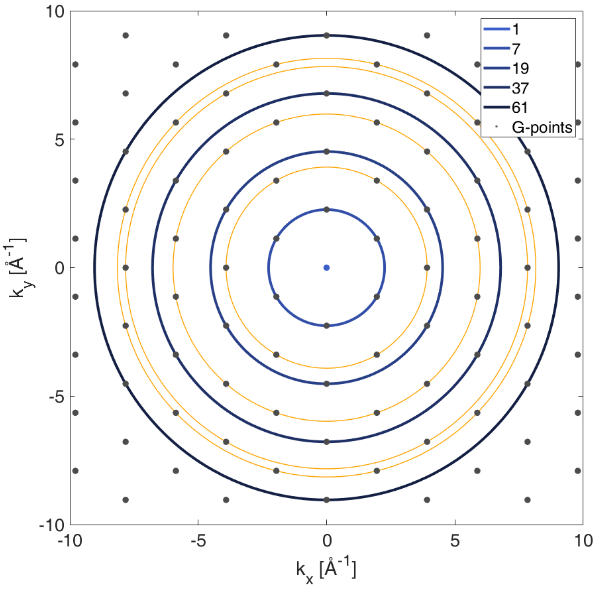

Figure 3.3.2: Reciprocal space with $\mathbf{G}$'s of equal length highlighted by circles. Blue lines correspond to $\mathbf{G}$'s that have a length equal to some integer multiple of the length of a reciprocal lattice vector.

Another important subject, when performing BSE calculations, is the $\mathbf{G}$ sum seen in equation (3.3.15). Due to the Keldysh potential in the Coulomb term, $\mathbf{G}$'s of increasing absolute value contribute less to this term than small ones. A similar argument holds for the exchange term, however the rate at which the $\mathbf{G}$'s converge is slightly slower here. Therefore, when performing the $\mathbf{G}$ summation, the terms with greatest impact are those with the smallest norm. In figure 3.3.2, $\mathbf{G}$'s of equal length can be seen. The blue ones are those $\mathbf{G}$'s with a length that is simply a multiple of the length of a reciprocal lattice vector.

It is also important to notice, that overlaps such as $I_{v'\mathbf{k}',v\mathbf{k}}(-\mathbf{G})$ includes a $\mathbf{G}$-shifted plane wave coefficient. Since our basis does not consists of all possible $\mathbf{G}$'s, larger values of $\mathbf{G}$ will decrease the number of plane wave coefficients that contribute to the overlap. As such, the contribution to the two potentials in the BSE would also weaken for large $\mathbf{G}$'s due to this fact.

Convergence with respect to k-points

Naturally, we would like to use as few k-points as possible in order to decrease the time and memory usage of the calculations. To achieve this, seven different DFT-calculations have been performed, ranging from 18×18 k-points to 54×54 k-points. All DFT-calculations have been performed using the PBE exchange correlation and with a cut-off frequency of 800 eV. Then, BSE calculations were performed with $\mathbf{G}$-radii corresponding to include 37 $\mathbf{G}$-vectors, using two valence bands and four conduction bands counted with spin-orbit hybridisation, and with a screening length of $r_0 = 2\pi\alpha_{xy}$ [22], where α_{xy} denotes the in-plane static total polarisability. This polarisability is extracted from the C2DB databse. In figure 3.3.3, two different convergence checks are shown. Figure 3.3.3a shows the binding energy, E_b, as a function of the number of k-points. The binding energy is calculated as

$$E_b = E_g - E_X, \tag{3.3.32}$$

where E_g denotes the fundamental bandgap, and E_X denotes the lowest exciton energy. As seen from the parameters of the exponential fit to data points, the binding energy should converge towards 0.55 eV in the limit of very high k-resolutions. In figure 3.3.3b, the 24 lowest exciton energies are shown as a function of k-resolution. It should be noted that the states are degenerate. At a resolution of 36 × 36 k-points the binding energy differs by $\leqslant$1% from that found using 54 × 54 k-points. Moreover, the exciton energies shown here deviates $\leqslant$2%, while the squared absolute of the bright dipole matrix elements are off by up to 18%. However, at 42 × 42 k-points this deviation is down to about 6% compared to 54 × 54, which suggest that it converges rather rapidly with respect to k-density. However, at the A excitonic resonance the absolute squared bright dipole matrix elements deviate $\leqslant$2%, when comparing a resolution of 36 × 36 to 54 × 54 k-points.

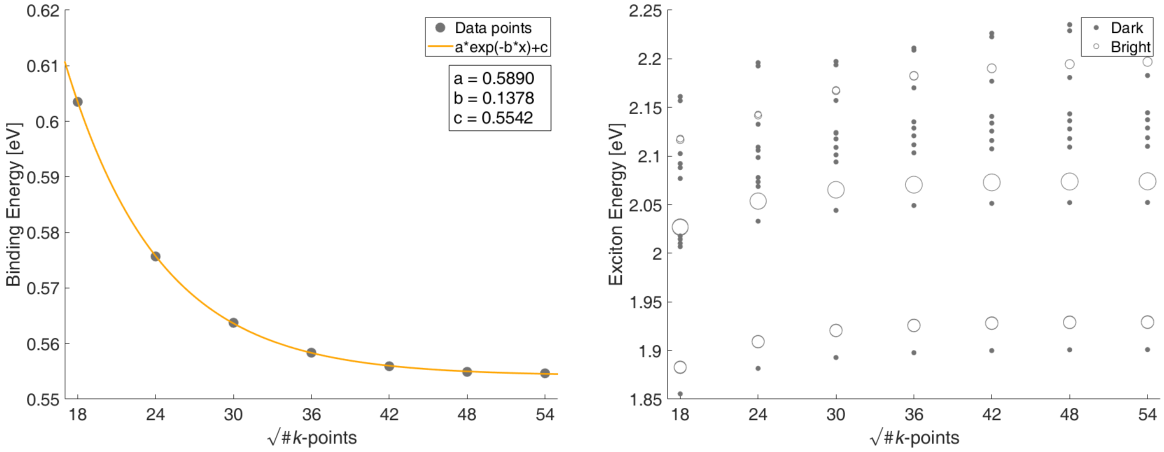

(a) (b)

Figure 3.3.3: (a) Convergence of binding energy with respect to k-density fitted with an exponential function. (b) Convergence of the 24 lowest exciton energies with respect to k-density displaying the absolute square of the (bright) corresponding dipole matrix elements as marker size.

An important aspect of the BSE calculations, and therefore also of the DFT calculations, is that the two fundamental excitons, A and B, are localised at the K-point, which in basis of the reciprocal lattice vectors has coordinates $(1/3, 1/3)$. These excitonic states are displayed in section 4.2. We choose the k-points such that they are distributed symmetrically around the high symmetry points - especially the K-point. As evident from figure 3.1.1 and the coordinate of the K-point, this can only be done by having k-points distributed in multiples of three (or six if you include the M-point) along the reciprocal vectors.

Ultimately, we have chosen a k-resolution of 39 × 39. At this density, which is a multiple of three, the BSE can be calculated at decent speeds without exceeding the threshold of available computer memory. Moreover, finding eigenvalues of $m \times m$-matrices scales with m^3, which means memory usage and computation time quickly can get out of hand.

Convergence with respect to Cut-off Energy

In figure 3.3.4, the binding energy and the 24 lowest exciton energies are displayed as a function of the cut-off energy. These calculations were performed on a 39 × 39 k-point grid using 4 × 4 spin-orbit hybridised bands and 37 **G**-vectors.

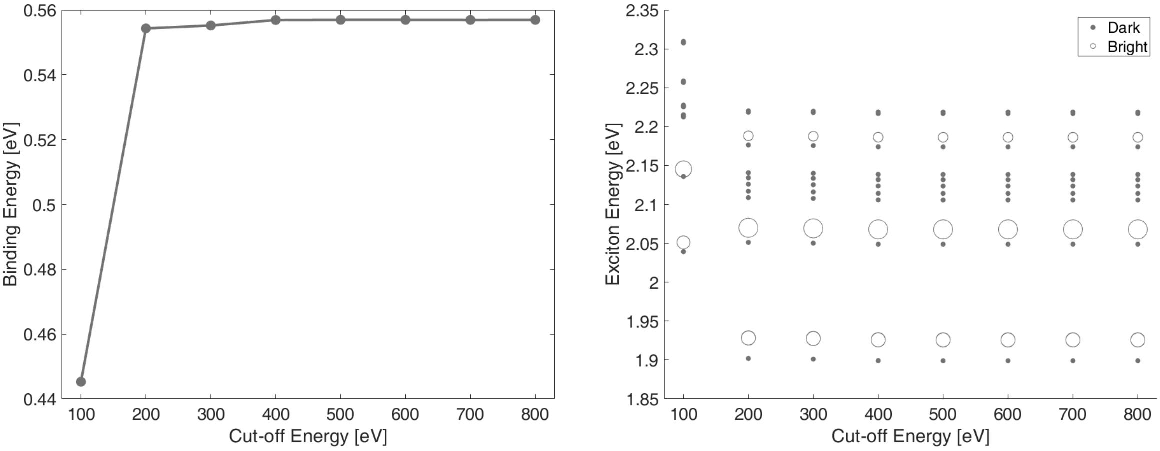

(a) (b)

Figure 3.3.4: (a) Convergence of binding energy with respect to cut-off energy. (b) Convergence of the 24 lowest exciton energies with respect to cut-off energy displaying the absolute square of the (bright) corresponding dipole matrix elements as marker size.

It seems the BSE calculations converge even at about 200 eV, where the exciton energies differ $\leqslant$0.1% from those found at a cut-off energy of 800 eV. Moreover, the excitonic momentum of the bright states differ by $\leqslant$0.5%. At a cut-off energy at 600 eV, the binding energy, excitonic energies, and absolute squared dipole matrix elements all deviate $\leqslant$0.01%, compared to 800 eV. For the sake of ensuring that the interpolation method is reliable, which is discussed in the following section, we have chosen to keep our cut-off energy at 600 eV. Higher cut-off energies do not severely increase the time or memory-usage of the BSE calculations in the PAW formalism. The time and memory-consuming part is calculating the PAW correction to the overlaps.

Convergence with respect to G-radii

In figure 3.3.5, the binding energy and the 24 lowest exciton energies can be seen with respect to the amount of **G**-vectors included in the Fourier decomposition's of the BSE, as seen in equation (3.3.3). This can be compared to figure 3.3.2. These calculations were performed on a 39 × 39 k-point grid, using a cut-off energy of 600 eV, and 4 × 4 spin-orbit hybridised bands.
It seems decent convergence is reached when 19 **G**-vectors are included in the Fourier decomposition, which is also the amount of **G**-vectors, we have chosen to include. Compared to using 61 **G**-vectors, the binding energy is barely different, the excitonic energies deviate $\leqslant$0.1%, and the absolute squared bright momentum matrix elements deviate $\leqslant$5%. It's worth mentioning that BSE computation time and memory usage scale somewhat linearly with increasing number of **G**-vectors.

Convergence with respect to Bands

Another subject, which is quite important when calculating the Purcell effect for a 2D layer is the sheet conductivity. In figure 3.3.6, the sheet conductivity is displayed with respect to the number

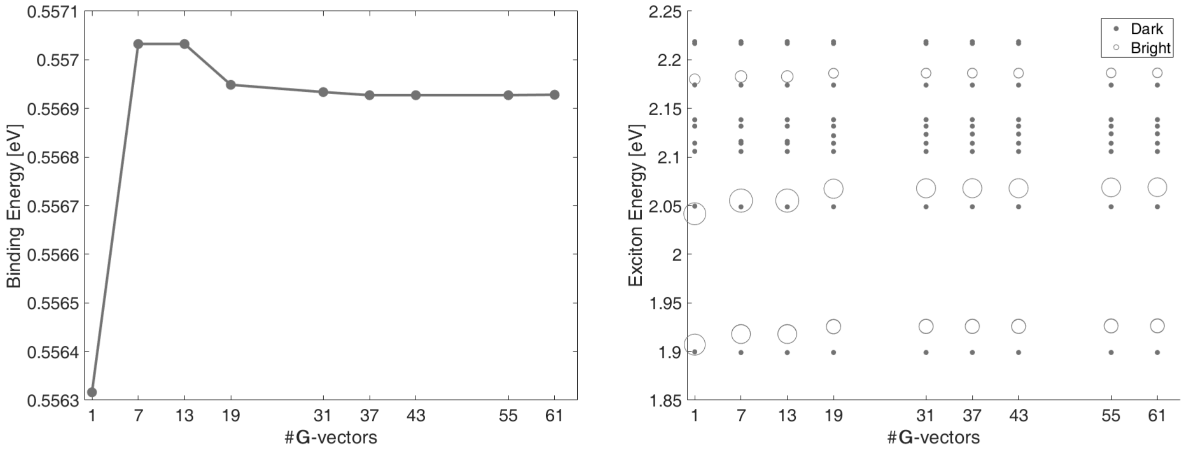

(a) (b)

Figure 3.3.5: (a) Convergence of binding energy with respect to **G**-radii. (b) Convergence of the 24 lowest exciton energies with respect to **G**-radii displaying the absolute square of the (bright) corresponding dipole matrix elements as marker size.

of bands included in the BSE calculation for MoS_2. The calculations were performed using 19 **G**-vectors, 39×39 k-points, a cut-off energy of 600 eV, a dampening factor of $\hbar\Gamma = 0.04$ eV, and finally $Q = 0$. In particular, the figure shows the importance of including an extra valence band. Clearly, this increases the sheet conductivity at the A exciton peak, which is the essential value(s) used for calculating Fresnel coefficients of a conducting 2D layer.

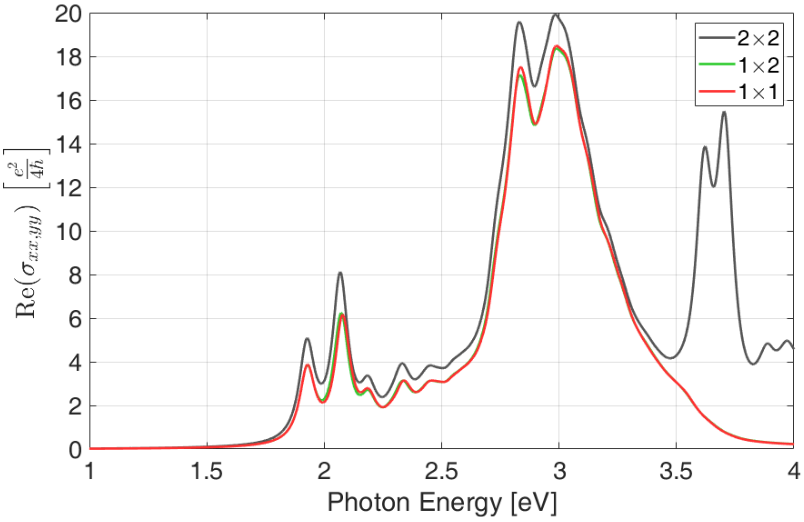

Figure 3.3.6: Optical sheet conductivity with respect to number of bands displayed as $v \times c$. Each band includes two spin-orbit hybridised bands.

Due to the computing power and time required to perform BSE calculations with an increasing numbers of bands, we will settle with showing and using conductivities found using 4×4 spin-orbit hybridised bands.

3.4 Bethe-Salpeter with Center of Mass Momentum

Of particular interest, when determining the spontaneous emission from a material, is the exciton dispersion for their center of mass momentum. Adding a center of mass momentum $\mathbf{Q}$ to the BSE simply amounts to replacing the conduction state $|c, \mathbf{k}\rangle \rightarrow |c, \mathbf{k}+\mathbf{Q}\rangle$ for all conduction states due to conservation of momentum. Applying this substitution to equation (3.3.13) and (3.3.14) gives

$$V^{Cou}_{v'vcc'}(\mathbf{G}) = \Omega^2 \sum_{\mathbf{G}} w_{Cou}(\mathbf{k}' - \mathbf{k} + \mathbf{G}) I_{v'\mathbf{k}',v\mathbf{k}}(-\mathbf{G}) I_{c\mathbf{k}+\mathbf{Q},c'\mathbf{k}'+\mathbf{Q}}(\mathbf{G}), \tag{3.4.1}$$

$$V^{exc}_{vcc'v'}(\mathbf{G}) = \Omega^2 \sum_{\mathbf{G}} w_{exc}(\mathbf{G} - \mathbf{Q}) I_{v\mathbf{k},c\mathbf{k}+\mathbf{Q}}(-\mathbf{G}) I_{c'\mathbf{k}'+\mathbf{Q},v'\mathbf{k}'}(\mathbf{G}). \tag{3.4.2}$$

This means that for each $\mathbf{Q}$, one needs an additional set of wave functions, calculated by the DFT, at the point $\mathbf{k}+\mathbf{Q}$, meaning there are three ways of handling this.

- Method 1: Limit oneself to $\mathbf{Q} = \mathbf{k} - \mathbf{k}'$ for points $\mathbf{k}, \mathbf{k}'$ already in the k-grid for the DFT.
- Method 2: Calculate the DFT anew for each $\mathbf{Q} \neq \mathbf{k} - \mathbf{k}'$ for points $\mathbf{k}, \mathbf{k}'$ already in the k-grid for the DFT.
- Method 3: Apply an interpolation scheme to attain the wave functions and energies at $\mathbf{k}+\mathbf{Q}$

Of these three methods, it is the third method which has been implemented, due to it having the versatility of method two without the need to evaluate a lot of timely DFT calculations.

3.4.1 Interpolation of the DFT-Quantities

Due to the wave functions having a random k-dependent phase, one must apply a phase correction in order to correctly interpolate these quantities. In particular, the wave functions are given in a plane wave basis with coefficients given as $C_{n\mathbf{k}}(\mathbf{G})$. Thus, in order to correct the phases, we take the shared largest value for $|C_{n\mathbf{k}}(\mathbf{G})|$, as shared for all n and $\mathbf{k}$, calling the corresponding $\max_{\text{shared}}(\mathbf{G}) =: \mathbf{G}_{\max}$. The next step is then to require $C_{n\mathbf{k}}(\mathbf{G}_{\max})$ to be entirely real and positive by dividing through with $\mathrm{e}^{i\arg(C_{n\mathbf{k}}(\mathbf{G}_{\max}))}$ for all of the planewaves $C_{n\mathbf{k}}(\mathbf{G})$. Likewise the planewaves $C_{m\mathbf{k}'}(\mathbf{G})$ are divided by the phase $\mathrm{e}^{i\arg(C_{m\mathbf{k}'}(\mathbf{G}_{\max}))}$. This same phase correction is applied to the PAW correction, by dividing through by the same phase for the quantities $\langle \tilde{p}^a_i | \tilde{\psi}_{n\mathbf{k}} \rangle$.

For the interpolation itself, there are a couple of different approaches. A general approach, which is viable to almost any k-grid, is to make a Delanuay triangulation on the grid-points and interpolate using this. This approach does however have some limitations as to which interpolation schemes are applicable. Another, much slower, approach would be to use regression and the least squares method. However, since a standard quadratic Monkhorst grid is being used, then the k-grid will be a standard meshed grid in the basis of the reciprocal vectors. Thus by switching the basis to the reciprocal vectors, one is able to apply gridded interpolation schemes, which are much faster than a regression approach. In particular, the 'spline' scheme has been chosen, as implemented by the SciPy package for python.

To avoid doing extrapolation, the interpolant grid, has been chosen to range from $[0,1]G_1$ and $[0,1]G_2$, meaning the states at the opposite boundaries of the grid are the same. This is then interpolated to a new grid, used for the BSE, where every state is unique. An issue arising due to interpolation, is that the introduced error means that states are no longer normalised, which is solved by renormalising the interpolated states. To make this approach work, one has to utilise the fact that for the plane wave expansion of the wavefunctions

$$\sum_{\mathbf{G}} C^*_{n,\mathbf{k}+\mathbf{Q}}(\mathbf{G}) \mathrm{e}^{i(\mathbf{G}+\mathbf{k}+\mathbf{Q})\cdot\mathbf{r}} = \sum_{\mathbf{G}} C^*_{n,\mathbf{k}+\mathbf{Q}}(\mathbf{G}+\mathbf{G}') \mathrm{e}^{i(\mathbf{G}+\mathbf{k}+\mathbf{Q}+\mathbf{G}')\cdot\mathbf{r}}, \tag{3.4.3}$$

meaning that by shifting the state by entire $\mathbf{G}$ vectors, the wavefunction stays the same, except for a transformation to the plane-wave basis.

To make this interpolation scheme yield good results, the interpolant grid is required to have a high enough resolution, for all the involved quantities to interpolate nicely. In figure 3.4.1 the Q-dependence for different interpolant resolutions can be seen. The relative dipole oscillator strength is a variable proportional to the absolute square of the parallel or perpendicular projection of the momentum elements on $\mathbf{Q}$. The material WSe_2 is shown here, since it has shown to converge the slowest of the TMDs in question, due to having the most in-continuities. Based on this, the interpolant resolution of 118×118 k-points was chosen for use in the presented results, since lower resolutions shows bumps on the linear and parabolic band.

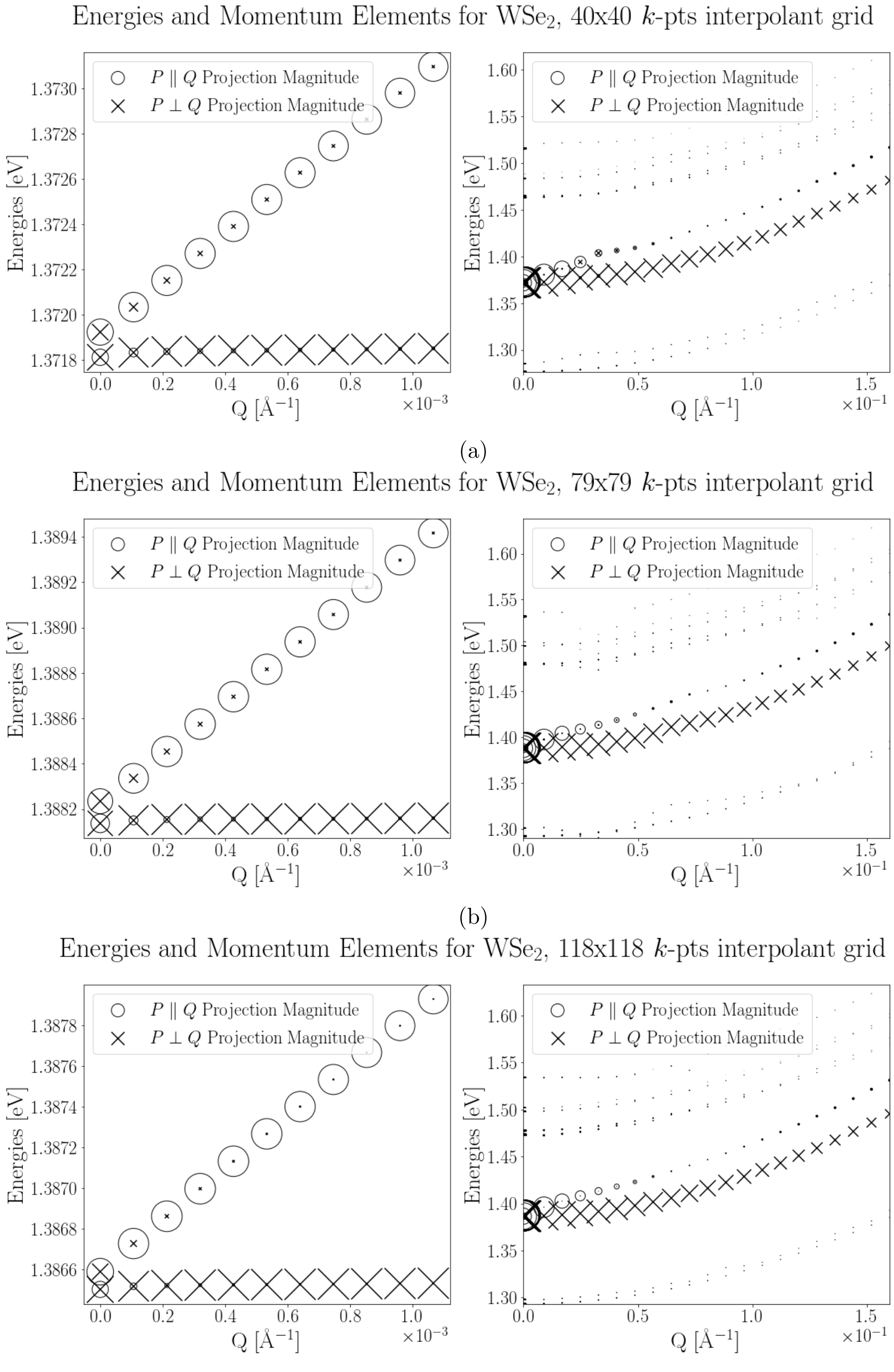

(a)

(b)

(c)

Figure 3.4.1: The Q-dependence of the energies and momentum elements at different interpolant resolutions. The squared projection of the parallel (perpendicular) momentum matrix elements upon $\mathbf{Q}$ is shown by the size of the circles (crosses).

Choice of Q-Grid

In theory, one must tabulate the entire irreducible Brillouin zone to attain the exciton band structure, however we find that for small values of Q, tabulating in a single direction is sufficient, since there is very little to no angular dependence, as can be seen in figure 3.4.2. In addition, it can also be seen that the momentum matrix elements for the upper linear band is purely parallel to $\mathbf{Q}$, while it is purely perpendicular to $\mathbf{Q}$ for the lower parabolic band.

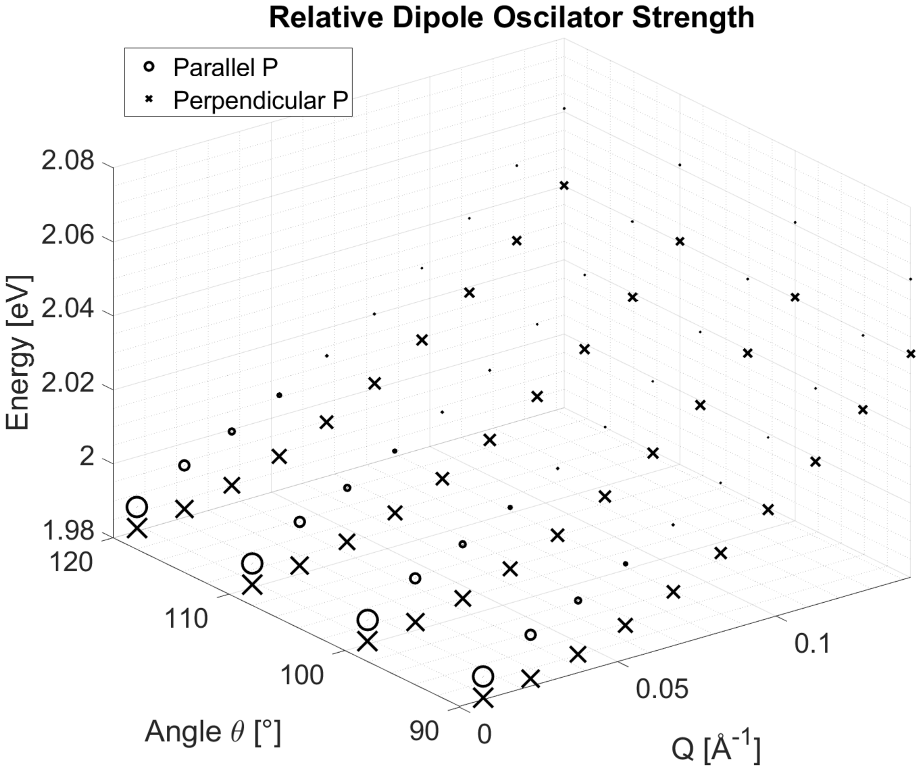

Figure 3.4.2: Lowest exciton energies and momentum element at different values of $\mathbf{Q}$, as well as the squared projection of the parallel (perpendicular) momentum matrix elements upon $\mathbf{Q}$ shown by the size of the circles (crosses) for MoS_2.

3.5 Emission for 2D-Materials

The emission rate for a 2D-material has been derived in section 2.3.4 and is given by equation (2.3.109)

$$\begin{aligned}\Gamma_{2D}(\mathbf{Q}) &= \frac{e^2}{2\omega\varepsilon_0\hbar m^2 cA}\sum_{q_x,q_y}\delta_{q_x,Q_x}\delta_{q_y,Q_y}\int \mathbf{P}^*_{\text{exc}}\cdot(\overleftrightarrow{\mathbf{I}} - \hat{q}\hat{q})\cdot\mathbf{P}_{\text{exc}}\delta\left(\frac{\omega}{c}-q\right)dq_z \\ &= \Gamma_0\begin{cases}\int\left(\frac{q_z}{q}\right)^2\delta\left(\frac{\omega}{c}-q\right)dq_z & \mathbf{P}_{exc}\parallel\mathbf{Q}\\ \int\delta\left(\frac{\omega}{c}-q\right)dq_z & \mathbf{P}_{exc}\perp\mathbf{Q}\end{cases}, \quad \text{with} \quad \Gamma_0 = \frac{e^2\|\mathbf{P}_{exc}\|^2}{2\omega\varepsilon_0\hbar m^2 cA}.\end{aligned} \tag{3.5.1}$$

There will therefore be two scenarios for q_z, namely propagating waves ($q_z \in (-\infty,\infty)$) and evanescent waves ($q_z \in i(-\infty,\infty)$). Due to the delta function being an even function, the integration bounds can be changed to $q_z \in (0, \infty)$ by multiplying the integral by 2. Thus, calculating the integral for propagating waves by substituting $q_z = \sqrt{q^2 - Q^2}$ yields

$$\Gamma_{2D}(\mathbf{Q}) = 2\Gamma_0 \begin{cases} \int_Q^\infty \frac{q_z}{q} \delta\left(\frac{\omega}{c} - q\right) dq & \mathbf{P}_{exc} \parallel \mathbf{Q} \\ \int_Q^\infty \frac{q}{q_z} \delta\left(\frac{\omega}{c} - q\right) dq & \mathbf{P}_{exc} \perp \mathbf{Q} \end{cases} \tag{3.5.2}$$

$$= 2\Gamma_0 \begin{cases} \frac{cq_z}{\omega} & \mathbf{P}_{exc} \parallel \mathbf{Q} \text{ and } Q \in [0, \omega/c) \\ \frac{\omega}{cq_z} & \mathbf{P}_{exc} \perp \mathbf{Q} \text{ and } Q \in [0, \omega/c) \end{cases}. \tag{3.5.3}$$

It should be noted that in this case, $\mathbf{P}_{exc}$ is restricted to the xy-plane with no z-component. Returning to $\mathbf{P}_{exc}$, it is given as

$$\mathbf{P}_{exc} = \sqrt{\frac{A}{(2\pi)^2}} \sum_{v,c,\mathbf{k}} \sum_{\sigma,\sigma'} \alpha_{v,\mathbf{k},\sigma}^{c,\mathbf{k},\sigma'} \langle v_\mathbf{k} | \hat{\mathbf{p}}(\mathbf{Q}) | c_\mathbf{k} \rangle \delta_{\sigma\sigma'} \sqrt{\Delta k_x \Delta k_y}, \tag{3.5.4}$$

as in equation (3.3.24). Here $\hat{\mathbf{p}}$ has been written as a function of simply $\mathbf{Q}$, that being the in-plane component of $\mathbf{q}$. This is justified due to the relation $q_z(\omega, \mathbf{q}) = \sqrt{\frac{\omega^2}{c^2} - ||\mathbf{q}||^2}$, where ω is assumed constant for the optical response around exciton A.

Assuming a pseudo-equilibrium for the excitons means their distribution should follow a Boltzmann statistic. In addition, due to the large energy difference between the two lowest exciton energies and the remaining excitons, one can safely assume that it is only these two excitons which are occupied at room- and lower temperature. Thus, the mean emission rate is

$$\langle \Gamma \rangle = \frac{1}{Z_1 + Z_2} \sum_{|\mathbf{Q}| < \omega/c} \left(\Gamma_1(\mathbf{Q}) \mathrm{e}^{-E_1(\mathbf{Q})/k_B T} + \Gamma_2(\mathbf{Q}) \mathrm{e}^{-E_2(\mathbf{Q})/k_B T} \right), \tag{3.5.5}$$

with E_1 and E_2 being the exciton energies, Γ_1 and Γ_2 the emission rates, and Z_1 and Z_2 the partition functions for the two lowest excitons. The sum over the photon momenta runs over $Q < \omega/c$, since a value higher than this would correspond to an evanescent wave. The expected lifetime can, from this, be calculated by simply using $\langle \tau \rangle = 1/\langle \Gamma \rangle$.

3.5.1 Quadratic and Linear Dispersion

The dispersion for the two lowest excitons in TMDs is generally that one is linear and the other parabolic for small Q, due to them being localised in the K-, and K'-valley. Defining exciton 1 as the parabolic and exciton 2 as the linear

$$E_1 = \frac{\hbar^2 Q^2}{2M}, \quad E_2 = \hbar V Q. \tag{3.5.6}$$

M and V are obtained by fitting E_1 and E_2 to the BSE results. A useful definition is then

$$\gamma_1 := \sqrt{\frac{\hbar^2}{M k_B T}}, \quad \gamma_2 := \frac{\hbar V}{k_B T}. \tag{3.5.7}$$

The partition functions are now

$$Z_1 = \sum_{\mathbf{Q}} \mathrm{e}^{-\frac{1}{2}\gamma_1^2 Q^2} = \frac{A}{2\pi\gamma_1^2}, \tag{3.5.8}$$

$$Z_2 = \sum_{\mathbf{Q}} \mathrm{e}^{-\gamma_2 Q} = \frac{A}{2\pi\gamma_2^2} \tag{3.5.9}$$

$$\Rightarrow \frac{1}{Z_1 + Z_2} = \frac{2\pi}{A} \left(\frac{\gamma_1^2 \gamma_2^2}{\gamma_1^2 + \gamma_2^2} \right). \tag{3.5.10}$$

Furthermore, it is assumed that $\Gamma_0(\mathbf{Q}) \approx \Gamma_0$ is constant for all states $|\mathbf{Q}| < \omega/c$, then

$$\begin{aligned}
\langle \Gamma \rangle &= \frac{2\pi}{A}\left(\frac{\gamma_1^2\gamma_2^2}{\gamma_1^2+\gamma_2^2}\right)\sum_{|\mathbf{Q}|<\omega/c}\Big(\Gamma_1(\mathbf{Q})\mathrm{e}^{-\frac{1}{2}(\gamma_1 Q)^2}+\Gamma_2(\mathbf{Q})\mathrm{e}^{-\gamma_2 Q}\Big) \qquad (3.5.11)\\
&\simeq \frac{1}{2\pi}\left(\frac{\gamma_1^2\gamma_2^2}{\gamma_1^2+\gamma_2^2}\right)\int_0^{2\pi}\int_0^{\omega/c}\Big(\Gamma_1(\mathbf{Q})\mathrm{e}^{-\frac{1}{2}(\gamma_1 Q)^2}+\Gamma_2(\mathbf{Q})\mathrm{e}^{-\gamma_2 Q}\Big)QdQd\theta. \qquad (3.5.12)
\end{aligned}$$

We may consider the linear ($\Gamma_0^{(2)}$) and parabolic ($\Gamma_0^{(1)}$) part separately, for the separate cases of $\mathbf{P}_n \perp \mathbf{Q}$ and $\mathbf{P}_n \parallel \mathbf{Q}$.

Parabolic, $\mathbf{P}_n \perp \mathbf{Q}$:

$$\begin{aligned}
\Gamma_0^{(1)}\int_0^{\omega/c} 2\left[1-\left(\frac{Qc}{\omega}\right)^2\right]^{-1/2}\mathrm{e}^{-\frac{1}{2}(\gamma_1 Q)^2}QdQ &= \Gamma_0^{(1)}\frac{\omega\sqrt{2\pi}}{\gamma_1 c}\mathrm{e}^{-\frac{\omega^2\gamma_1^2}{2c^2}}\operatorname{erfi}\left(\frac{\omega\gamma_1}{c\sqrt{2}}\right)\\
&\approx \Gamma_0^{(1)}\frac{2\omega^2}{c^2}.
\end{aligned} \qquad (3.5.13)$$

Parabolic, $\mathbf{P}_n \parallel \mathbf{Q}$:

$$\begin{aligned}
\Gamma_0^{(1)}\int_0^{\omega/c} 2\left[1-\left(\frac{Qc}{\omega}\right)^2\right]^{1/2}\mathrm{e}^{-\frac{1}{2}(\gamma_1 Q)^2}QdQ &= 2\Gamma_0^{(1)}\left[\frac{1}{\gamma_1^2}-\frac{c\sqrt{\frac{\pi}{2}}\mathrm{e}^{-\frac{\omega^2\gamma_1^2}{2c^2}}\operatorname{erfi}\left(\frac{\gamma_1\omega}{\sqrt{2}c}\right)}{\omega\gamma_1^3}\right]\\
&\approx \Gamma_0^{(1)}\frac{\omega^2}{3c^2},
\end{aligned} \qquad (3.5.14)$$

where $\operatorname{erfi}(x)$ denotes the imaginary error function.

Linear, $\mathbf{P}_n \perp \mathbf{Q}$:

$$\begin{aligned}
\Gamma_0^{(2)}\int_0^{\omega/c} 2\left[1-\left(\frac{Qc}{\omega}\right)^2\right]^{-1/2}\mathrm{e}^{-\gamma_2 Q}QdQ &= \Gamma_0^{(2)}\frac{\pi\omega^2}{c^2}\left[L_{-1}\left(\frac{\omega\gamma_2}{c}\right)-I_1\left(\frac{\omega\gamma_2}{c}\right)\right]\\
&\approx \Gamma_0^{(2)}\frac{\pi\omega^2}{c^2}\left[\frac{1}{\Gamma\left(\frac{3}{2}\right)\Gamma\left(\frac{1}{2}\right)}-\frac{\omega\gamma_2}{2c}\right]\\
&\approx \Gamma_0^{(2)}\frac{2\omega^2}{c^2}.
\end{aligned} \qquad (3.5.15)$$

Linear, $\mathbf{P}_n \parallel \mathbf{Q}$:

$$\begin{aligned}
&\Gamma_0^{(2)}\int_0^{\omega/c} 2\left[1-\left(\frac{Qc}{\omega}\right)^2\right]^{1/2}\mathrm{e}^{-\gamma_2 Q}QdQ\\
&= \Gamma_0^{(2)}\frac{2\omega^2}{c^2}\left[-\frac{\pi c}{2\omega\gamma_2}I_0\left(\frac{\omega\gamma_2}{c}\right)+\frac{\pi c}{2\omega\gamma_2}L_0\left(\frac{\omega\gamma_2}{c}\right)+\frac{\pi c^2}{\omega^2\gamma_2^2}I_1\left(\frac{\omega\gamma_2}{c}\right)-\frac{\pi c^2}{\omega^2\gamma_2^2}L_1\left(\frac{\omega\gamma_2}{c}\right)\right]\\
&\approx \Gamma_0^{(2)}\frac{2\omega^2}{3c^2},
\end{aligned} \qquad (3.5.16)$$

where $I_n(x)$ denotes the modified Bessel function of the first kind and $L_n(x)$ denotes the modified Struve function. The integrals in the above calculations have been carried out using different CAS-tools. A general observed result for the materials being examined in this project, is that the exciton with linear dispersion is polarised almost entirely parallel to $\mathbf{Q}$, and vice versa for the parabolic one. Thus, the expectation value for the emission rate becomes

$$\langle\Gamma\rangle \approx \frac{\gamma_1^2\gamma_2^2}{\gamma_1^2+\gamma_2^2}\frac{\omega^2}{c^2}\left[2\,\Gamma_0^{(1)} + \frac{2}{3}\,\Gamma_0^{(2)}\right]. \tag{3.5.17}$$

Another interesting expression to derive, would be one for the spectrum as a function of $\mathbf{Q}$. In practice, the normalised spectrum is given by the normalised summand of equation (3.5.11)

$$\frac{\Gamma(\mathbf{Q})}{\Gamma(0)} = \frac{\Gamma_1(\mathbf{Q})\mathrm{e}^{-\frac{1}{2}(\gamma_1 Q)^2} + \Gamma_2(\mathbf{Q})\mathrm{e}^{-\gamma_2 Q}}{\Gamma_1(0)+\Gamma_2(0)} \tag{3.5.18}$$

$$= \frac{\Gamma_0^{(1)}\left[1-\left(\frac{Qc}{\omega}\right)^2\right]^{-1/2}\mathrm{e}^{-\frac{1}{2}(\gamma_1 Q)^2} + \Gamma_0^{(2)}\left[1-\left(\frac{Qc}{\omega}\right)^2\right]^{1/2}\mathrm{e}^{-\gamma_2 Q}}{\Gamma_0^{(1)}+\Gamma_0^{(2)}}. \tag{3.5.19}$$

3.5.2 Numerical Integration of Dispersion

In practise Γ_0 will depend on $\mathbf{Q}$, especially for large values of $\mathbf{Q}$. In addition, the assumption that the linear dispersed exciton is polarised entirely parallel to $\mathbf{Q}$ and vice versa for the parabolic dispersed exciton, is not guaranteed for non K-valley bound excitons. Finally, at temperatures above a few kelvin, the partition function should be integrated numerically, since the linear dispersion becomes non-linear at $Q \gg \omega/c$. To improve upon this, one will have to solve the integral in equation (3.5.5) numerically. When doing this, one can also easily include additional bright bands, since no assumptions of the dispersions will be made. The partition function can be calculated using a simple trapezoidal numerical integration method, where it is thus required that the BSE has been evaluated for enough values of $\mathbf{Q}$. In addition, we still assume the angular dependence of $E_n(\mathbf{Q})$ to be negligible, thus assuming that the BSE has been solved for M_1 different values of $Q \in [0, B\omega/c]$, for some sufficiently large number B, the partition function is

$$Z_n = \frac{A}{2\pi}\sum_{i=1}^{M_1-1}\frac{\mathrm{e}^{-E_n(Q_{i+1})/k_BT}+\mathrm{e}^{-E_n(Q_i)/k_BT}}{2}\frac{Q_{i+1}^2-Q_i^2}{2}. \tag{3.5.20}$$

The upper limit on Q is set to $B\omega/c$, since the corresponding energy at this point should give a very low contribution at room temperature and lower. It is worth to note that at higher values of Q, the energy will go back to the case of $Q = 0$, however surpassing the energy barrier to get there will be very unlikely, thus these states are assumed impossible in a pseudo equilibrium like this. As a result of this, the value of B in this project is around 150.

Numerically calculating (3.5.5) is done by assuming that $\Gamma_i(Q,\theta)$ depends on Q as a step function and then solving the remaining integral as before. Furthermore, an interpolation scheme has been implemented to make sure the steps are small enough for the integral to be accurate, which becomes important due to how large the $\Gamma(Q)$-values get at $Q \approx \omega/c$. Once again there is assumed no angular dependence. Assuming the BSE has been solved for M_2 different values of $Q \in [0, \omega/c]$ the thermally averaged emission rate is

$$\langle\Gamma\rangle = \frac{1}{\sum_n Z_n}\sum_n\sum_{|\mathbf{Q}|<\omega/c}\Gamma_n(\mathbf{Q})\mathrm{e}^{-E_n(\mathbf{Q})/k_BT} \tag{3.5.21}$$

$$\simeq \frac{A}{2\pi\sum_n Z_n}\sum_n\int_0^{\omega/c}\Gamma_n(Q)\mathrm{e}^{-E_n(Q)/k_BT}QdQ \tag{3.5.22}$$

$$\simeq \frac{A}{2\pi\sum_n Z_n}\sum_n\sum_{i=1}^{M_2-1}\frac{\Gamma_n(Q_{i+1})\mathrm{e}^{-E_n(Q_{i+1})/k_BT}+\Gamma_n(Q_i)\mathrm{e}^{-E_n(Q_i)/k_BT}}{2}\frac{Q_{i+1}^2-Q_i^2}{2}. \tag{3.5.23}$$

The difference between the simple model (Γ_0-model) derived in the preceding section, and this model for $\langle\Gamma\rangle$ for MoS$_2$ can be seen in figure 3.5.1. For the rest of the project, the 'numerical' model will be used, since it should be more accurate, and does not require significant computation time or memory usage.

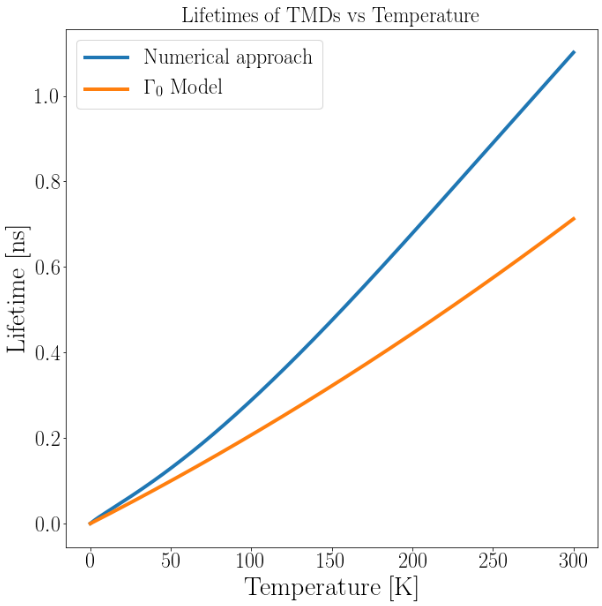

Figure 3.5.1: $\langle\tau\rangle$ for MoS$_2$ as a function of temperature.

3.6 Purcell Enhancement

As seen in the previous sections, a given center of mass momentum, $\hbar\mathbf{Q}$, always induces a response in the form of a dipole moment, which is either parallel or perpendicular to the momentum. Moreover, the response is independent of the direction of $\mathbf{Q}$, which was shown in figure 3.4.2. Thus, letting $\mathbf{Q} = Q_y\hat{y}$, implies that the dipole moment is oriented along either $\hat{x}$ or $\hat{y}$. Using equations (2.4.7) and (2.4.9), the direct dissipated power can be found as

$$W^{(d)}(Q_y) = \frac{\mu_0\omega^3|\boldsymbol{\mu}|^2}{4}\begin{cases}\mathrm{Re}\Big\{\frac{1}{k_{z1}}\Big\}, & \boldsymbol{\mu}\perp\mathbf{Q}\\ \mathrm{Re}\Big\{\frac{k_{z1}}{k_1^2}\Big\}, & \boldsymbol{\mu}\parallel\mathbf{Q}\end{cases}, \tag{3.6.1}$$

where it has been used that $Q_x = 0$. Similarly, the indirect dissipated power may be found as

$$W^{(i)}(Q) = \frac{\mu_0\omega^3|\boldsymbol{\mu}|^2}{4}\begin{cases}\mathrm{Re}\Big\{\frac{r^{(s)}(Q_y)}{k_{z1}}\mathrm{e}^{2ik_{z1}d}\Big\}, & \boldsymbol{\mu}\perp\mathbf{Q}\\ \mathrm{Re}\Big\{-\frac{r^{(p)}(Q_y)k_{z1}}{k_1^2}\mathrm{e}^{2ik_{z1}d}\Big\}, & \boldsymbol{\mu}\parallel\mathbf{Q}\end{cases}. \tag{3.6.2}$$

Ultimately, this means that the Purcell effect, $P(Q_y)$, can be found as

$$P(Q_y) = 1 + \frac{\mathrm{Re}\Big\{\frac{r^{(s)}(Q_y)}{k_{z1}}\mathrm{e}^{2ik_{z1}d}\Big\}}{\mathrm{Re}\Big\{\frac{1}{k_{z1}}\Big\}}\delta_{\mu_y,0} - \frac{\mathrm{Re}\Big\{\frac{r^{(p)}(Q_y)k_{z1}}{k_1^2}\mathrm{e}^{2ik_{z1}d}\Big\}}{\mathrm{Re}\Big\{\frac{k_{z1}}{k_1^2}\Big\}}\delta_{\mu_x,0}. \tag{3.6.3}$$

However, the expression can be reduced further. We consider only modes where $Q_y^2 < k_1^2$, which means that $\mathrm{Re}\{k_{z1}\} = k_{z1}$. Moreover, it is worth noticing that $k_{z1}^2 = k_1^2 - Q_y^2$. The expression is then reduced to

$$P(Q_y) = 1 + \mathrm{Re}\Big\{r^{(s)}(Q_y)\mathrm{e}^{2ik_{z1}d}\Big\}\delta_{\mu_y,0} - \mathrm{Re}\Big\{r^{(p)}(Q_y)\mathrm{e}^{2ik_{z1}d}\Big\}\delta_{\mu_x,0}. \tag{3.6.4}$$

This is then the Purcell enhancement of a single mode Q_y. As such, the emission rate, and thus the lifetime, is modified by

$$\Gamma(Q_y) = P(Q_y)\Gamma_0(Q_y). \tag{3.6.5}$$

In order to calculate the thermally averaged emission rate in an inhomogeneous environment, $\Gamma_n(Q)$ in equation (3.5.23) should then simply undergo the substitution $\Gamma_n(Q) \to P(Q)\Gamma_n(Q)$.

3.6.1 Choice of Geometry

In order to calculate the Purcell effect, the dielectric geometry must first be established. We have chosen to examine an environment such as the one seen in figure 3.6.1.

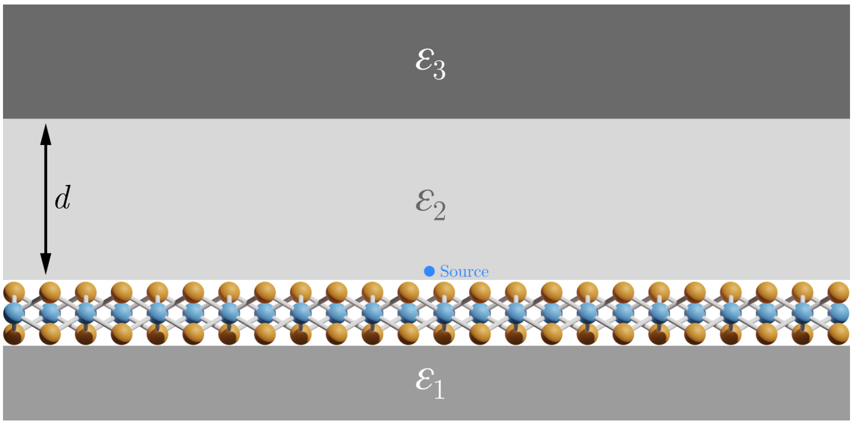

Figure 3.6.1: Dielectric environment considered in this project. The emitting layer consisting of the TMD should be assumed infinitesimally thin for this purpose.

Formally, this can be written as

$$\varepsilon(z) = \begin{cases} \varepsilon_1, & z_0 > z \\ \varepsilon_2, & z_0 - d > z > z_0 \\ \varepsilon_3, & z > z_0 - d \end{cases}. \tag{3.6.6}$$

From here, we will assume that $\varepsilon_1 = \varepsilon_2$. We need an effective reflection coefficient for the entire material, if we are to calculate the Purcell effect. If the "source" is located above but infinitesimally close to the emitter, the reflection coefficients can then be calculated as

$$r_{eff}^{(s,p)} = r_{23}^{(s,p)}\mathrm{e}^{2iq_{z1}d}\sum_{n=0}^{\infty}\left(r_E^{(s,p)}r_{23}^{(s,p)}\mathrm{e}^{2iq_{z1}d}\right)^n. \tag{3.6.7}$$

The reflection coefficients are found as:

$$r_E^{(s)} = \frac{-\omega\mu_0\sigma_s}{2q_{z1} + \omega\mu_0\sigma_s}, \quad r_E^{(p)} = \frac{q_{z1}^2\sigma_s(\omega\varepsilon_0)^{-1}}{2q_{z1}\varepsilon_1 + q_{z1}^2\sigma_s(\omega\varepsilon_0)^{-1}}, \tag{3.6.8}$$

$$r_{23}^{(s)} = \frac{q_{z3} - q_{z1}}{q_{z3} + q_{z1}}, \quad r_{23}^{(s)} = \frac{q_{z3}\varepsilon_1 - q_{z1}\varepsilon_3}{q_{z3}\varepsilon_1 + q_{z1}\varepsilon_3}, \tag{3.6.9}$$

where equation (3.6.8) agrees with section 2.4.2. Equation (3.6.7) can be rewritten as

$$r_{eff}^{(s,p)} = \frac{r_{23}^{(s,p)} \mathrm{e}^{2iq_{z1}d}}{1 - r_E^{(s,p)} r_{23}^{(s,p)} \mathrm{e}^{2iq_{z1}d}}. \tag{3.6.10}$$

Finally, the Q-dependent Purcell enhancement should then be corrected, since $\exp(2iq_{z1}d)$ is included in the reflection coefficients (thus letting $z_0 = 0$), such that

$$P(Q_y) = \frac{2 + \mathrm{Re}\left\{r_{eff}^{(s)}(Q_y)\right\}\delta_{\mu_y,0} - \mathrm{Re}\left\{r_{eff}^{(p)}(Q_y)\right\}\delta_{\mu_x,0}}{2}, \tag{3.6.11}$$

where the division by two arises due to the material emitting on both sides.

3.6.2 Enclosed Cavity Geometry

Another interesting geometry would be a fully enclosed cavity as illustrated in figure 3.6.2, where multiple reflections will take place, meaning one would expect much bigger effects from the 2D material. Consider the geometry in figure 3.6.2, here the upwards and downwards reflection coefficients are

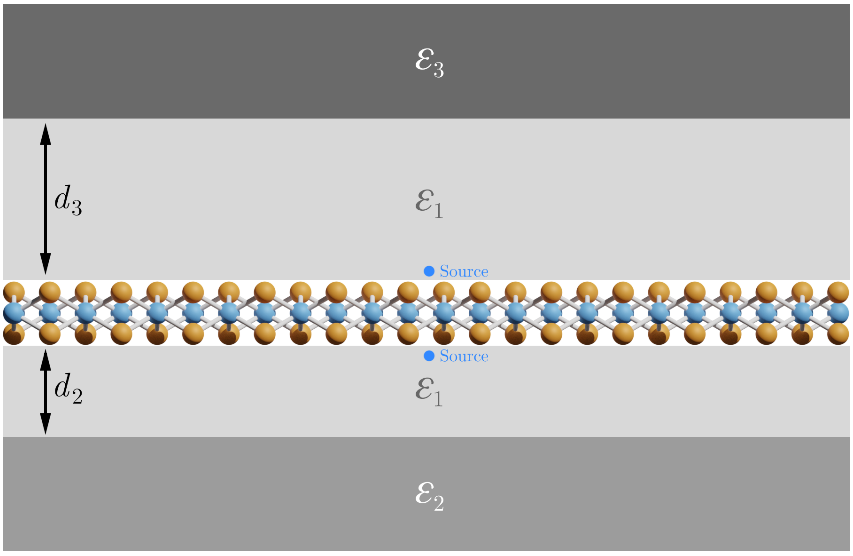

Figure 3.6.2: The cavity environment considered in section 3.6.2. The emitting layer consisting of the TMD should be assumed infinitesimally thin for this purpose.

$$r_{\text{up}} = r_{13}\mathrm{e}^{2id_3q_{z1}} \sum_{n=0}^{\infty} \left(r_{\text{down}}^* r_{13}\mathrm{e}^{2id_3q_{z1}}\right)^n = \frac{r_{13}\mathrm{e}^{2id_3q_{z1}}}{1 - r_{\text{down}}^* r_{13}\mathrm{e}^{2id_3q_{z1}}}, \tag{3.6.12}$$

$$r_{\text{down}} = r_{12}\mathrm{e}^{2id_2q_{z1}} \sum_{n=0}^{\infty} \left(r_{\text{up}}^* r_{12}\mathrm{e}^{2id_2q_{z1}}\right)^n = \frac{r_{12}\mathrm{e}^{2id_2q_{z1}}}{1 - r_{\text{up}}^* r_{12}\mathrm{e}^{2id_2q_{z1}}}, \tag{3.6.13}$$

where

$$r_{\text{up}}^* = r_E + t_E^2 r_{13}\mathrm{e}^{2id_3q_{z1}} \sum_{n=0}^{\infty} \left(r_{\text{down}}^* r_{13}\mathrm{e}^{2id_3q_{z1}}\right)^n = r_E + \frac{t_E^2 r_{13}\mathrm{e}^{2id_3q_{z1}}}{1 - r_{\text{down}}^* r_{13}\mathrm{e}^{2id_3q_{z1}}}, \tag{3.6.14}$$

$$r_{\text{down}}^* = r_E + t_E^2 r_{12}\mathrm{e}^{2id_2q_{z1}} \sum_{n=0}^{\infty} \left(r_{\text{up}}^* r_{12}\mathrm{e}^{2id_2q_{z1}}\right)^n = r_E + \frac{t_E^2 r_{12}\mathrm{e}^{2id_2q_{z1}}}{1 - r_{\text{up}}^* r_{12}\mathrm{e}^{2id_2q_{z1}}}. \tag{3.6.15}$$

Here t_E is given as equation (2.4.21) and (2.4.30) for s- and p-polarization. We have solved these equations for r^*_{down} in section A.3, where the following expression was derived:

$$r^*_{\text{down}} = \frac{-1 - r_E r_{13} \mathrm{e}^{2id_3 q_{z1}} \pm \sqrt{D_d}}{-2r_{13}\mathrm{e}^{2id_3 q_{z1}}}, \tag{3.6.16}$$

where

$$D_d = \left(1 - r_E r_{13} \mathrm{e}^{2id_3 q_{z1}}\right)^2 - \frac{4\left(1 - r_E r_{13}\mathrm{e}^{2id_3 q_{z1}}\right) t_E^2 r_{12} r_{13} \mathrm{e}^{2iq_{z1}(d_2+d_3)}}{1 + r_E r_{12}\mathrm{e}^{2id_2 q_{z1}}}. \tag{3.6.17}$$

It should be noted here that when considering the limit of $\varepsilon_1 = \varepsilon_2 = \varepsilon_3$, only the plus solution gives a finite answer, namely

$$\lim_{r_{13}, r_{12} \to 0} D_d = 1 - 2r_E r_{13}\mathrm{e}^{2id_2 q_{z1}}, \tag{3.6.18}$$

$$\lim_{r_{13}, r_{12} \to 0} r^*_{\text{down}} = \frac{-1 - r_E r_{13}\mathrm{e}^{2id_2 q_{z1}} \pm \left(1 - r_E r_{13}\mathrm{e}^{2id_2 q_{z1}}\right)}{-2r_{13}\mathrm{e}^{2id_2 q_{z1}}}, \tag{3.6.19}$$

which in the case of the plus solution yields $\lim_{r_{13}, r_{12}\to 0} r^*_{\text{down}} = r_E$, as expected from equation (3.6.15). The exact same derivation can be done for r^*_{up}, and can therefore be expressed as

$$r^*_{\text{up}} = \frac{-1 - r_E r_{12}\mathrm{e}^{2id_2 q_{z1}} \pm \sqrt{D_u}}{-2r_{12}\mathrm{e}^{2id_2 q_{z1}}}, \tag{3.6.20}$$

where

$$D_u = \left(1 - r_E r_{12}\mathrm{e}^{2id_2 q_{z1}}\right)^2 - \frac{4\left(1 - r_E r_{12}\mathrm{e}^{2id_2 q_{z1}}\right) t_E^2 r_{12} r_{13}\mathrm{e}^{2iq_{z1}(d_2+d_3)}}{1 + r_E r_{13}\mathrm{e}^{2id_3 q_{z1}}}. \tag{3.6.21}$$

The Q-dependent Purcell factor is then calculated using

$$P(Q_y) = \frac{2 + \mathrm{Re}\left\{r^{(s)}_{\text{up}}(Q_y) + r^{(s)}_{\text{down}}(Q_y)\right\}\delta_{\mu_y,0} - \mathrm{Re}\left\{r^{(p)}_{\text{up}}(Q_y) + r^{(p)}_{\text{down}}(Q_y)\right\}\delta_{\mu_x,0}}{2}. \tag{3.6.22}$$

4 Results

In this section, we will show results based on the calculations presented in the preceding chapter. In particular, the electronic band structures based on the DFT calculations and spectra calculated from the BSE will be presented and described. Following this, the excitonic emission oriented calculations will be presented, herein lies the energy levels and momentum element projections for excitons with a center of mass momentum $Q \neq 0$, proceeded by the lifetimes derived thereof. Finally, these results will be used to make a simple calculation for the Purcell enhancement, and its role on the exciton lifetimes.

4.1 DFT Band Structures for TMDs

In figure 4.1.1, the band structures of the four different TMDs are shown. They are plotted along a path of time reversal symmetry, which can be seen in the flip of the z-spin projection of the spin-orbit eigenvalues. The figure also shows the stronger effect of spin-orbit coupling introduced in WS_2 and WSe_2, which is due to the increased mass of the tungsten atom compared to molybdenum. It is worth noticing, that -K corresponds to K' and -M to M.

4.2 Exciton Results of TMDs

As mentioned in section 3.1, the primary excitons A and A' are localised at the K- and K'-points of symmetry. These excitons form the start of the lowest linear and quadratic bright bands in the excitonic dispersions seen in section 4.2.2. In figures 4.2.1a and 4.2.1b, the absolute value of the wave-functions/eigenvectors corresponding to the two lowest bright excitonic states can be seen for MoS_2. The BSE calculation was performed using one valence band, two conduction bands (one odd and one even), and with $Q = \omega/c \approx 10^{-3}\,\text{Å}^{-1}$. In figures 4.2.1c and 4.2.1d, plots from the same calculation can be seen, but this time excitons B and B' are displayed, which correspond to the second-lowest bright exciton energy.

4.2.1 Optical Spectra of TMDs

In figure 4.2.2, the sheet conductivities of the four TMDs in question can be seen with spin-orbit coupling included. All calculations were performed using two valence bands and two conduction bands. Furthermore, a damping factor of $\hbar\Gamma = 0.04$ eV has been used in all cases. Moreover, all calculations were performed using $Q = 0$, since we found that there is virtually no difference between using $Q = 0$ and using some Q smaller than ω/c in the optical spectra. The only visible difference is a small shift in the energies. Using the optical sheet conductivity, it is also possible to calculate the optical absorbance. The transmittance can be found using [22, ch. 17]

$$T(\omega) = \exp\left(-\frac{2d\omega \text{Im}\{\sqrt{\varepsilon(\omega)}\}}{c}\right), \quad \varepsilon(\omega) = 1 + i\frac{\sigma(\omega)}{\varepsilon_0 \omega d}, \tag{4.2.1}$$

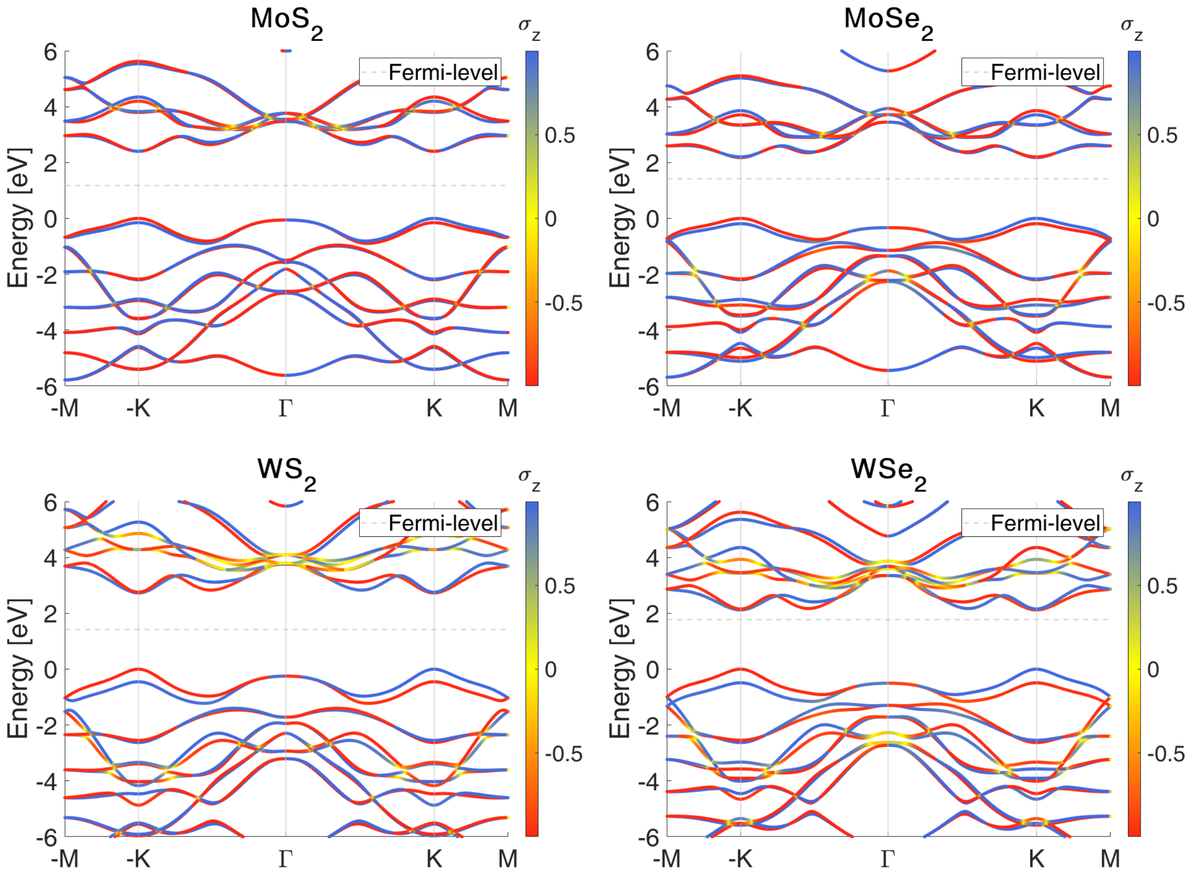

Figure 4.1.1: DFT band diagrams for the four TMDs considered in this report with a cut-off energy of 600 eV and 1800 k-points using the PBE functional. The highest valence eigenvalue is set to 0 eV.

where d denotes the thickness of the layer. The optical absorbance is then found using $A(\omega) = 1 - T(\omega)$, which can also be seen in figure 4.2.2.

4.2.2 Exciton Dispersions

In this section, the results obtained by performing the calculations detailed in section 3.4 will be presented. In figure 4.2.3 and 4.2.4, the calculated dispersion relations are shown for the ten lowest energy excitons, for low values of Q. In particular, a lot of evaluated points are placed in the region $Q < \omega/c \approx 0.9 \cdot 10^{-3}\text{Å}^{-1}$, since this is of particular interest when calculating the emission. These figures clearly show the parabolic and non-analytical band for the materials in question. Furthermore, a polynomial fit has been made for the lowest bright polynomial band, which has a corresponding effective mass presented under each figure, as calculated by a polynomial fit

$$E_p(Q) = E_p(0) + Q^2 \frac{\hbar^2}{2m_e M_p^*} = E_p(0) + f_1 Q^2 \tag{4.2.2}$$

$$\Rightarrow M_p^* = \frac{\hbar^2}{2m_e f_1}, \tag{4.2.3}$$

where f_1 is the curvature of polynomial fit. For all cases the fit follows the calculated points excellently, supporting some of the approximations made in section 3.5. In addition, it can be

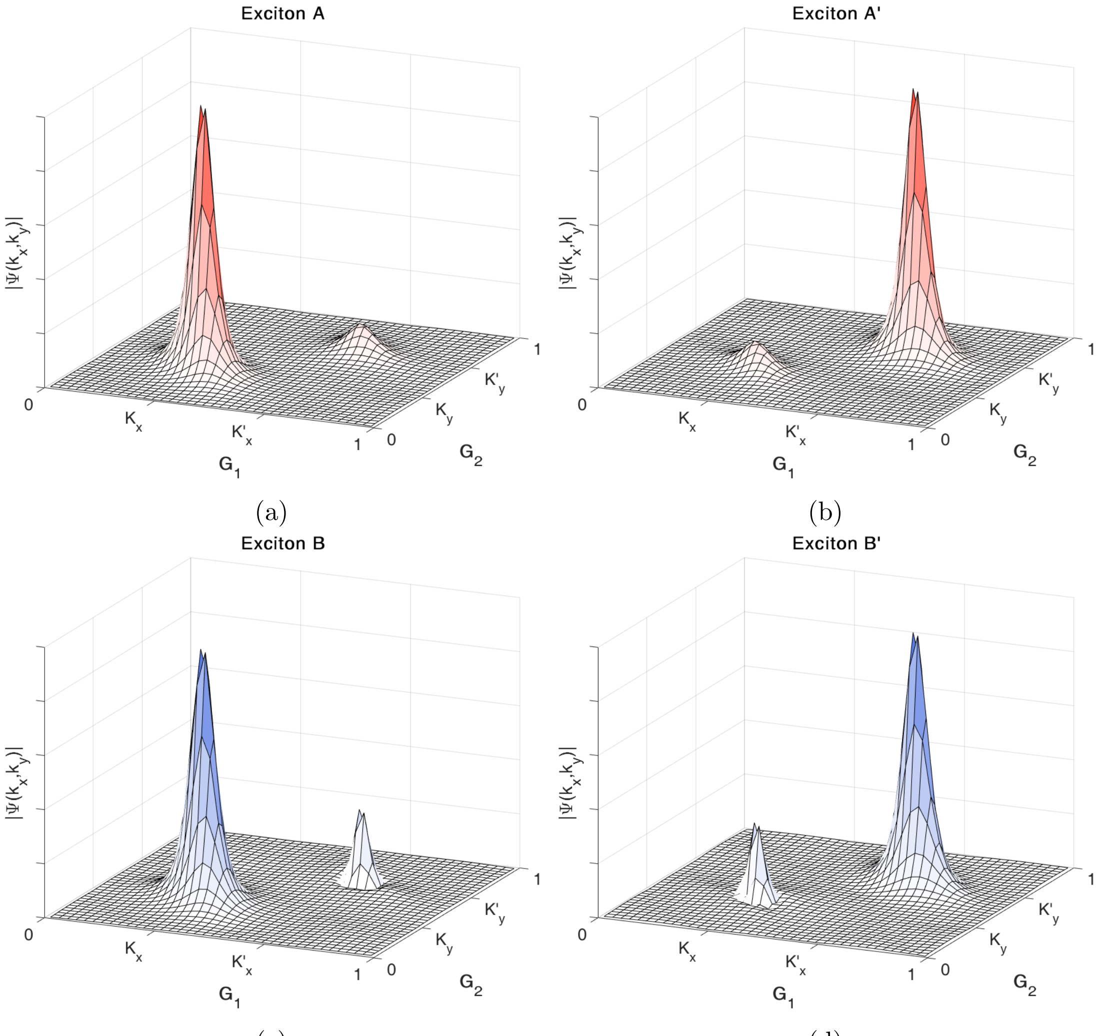

(a) (b)

(c) (d)

Figure 4.2.1: (a) The wave function of exciton A, which is localised at the K-point, and (b) the wave function of exciton A' localised at the K'-point. (c) The wave function of exciton B, which is localised at the K-point, and (d) the wave function of exciton B' localised at the K'-point.

seen that the non-analytical band only stays linear for very low values of Q, explaining the deviation shown in figure 3.5.1.

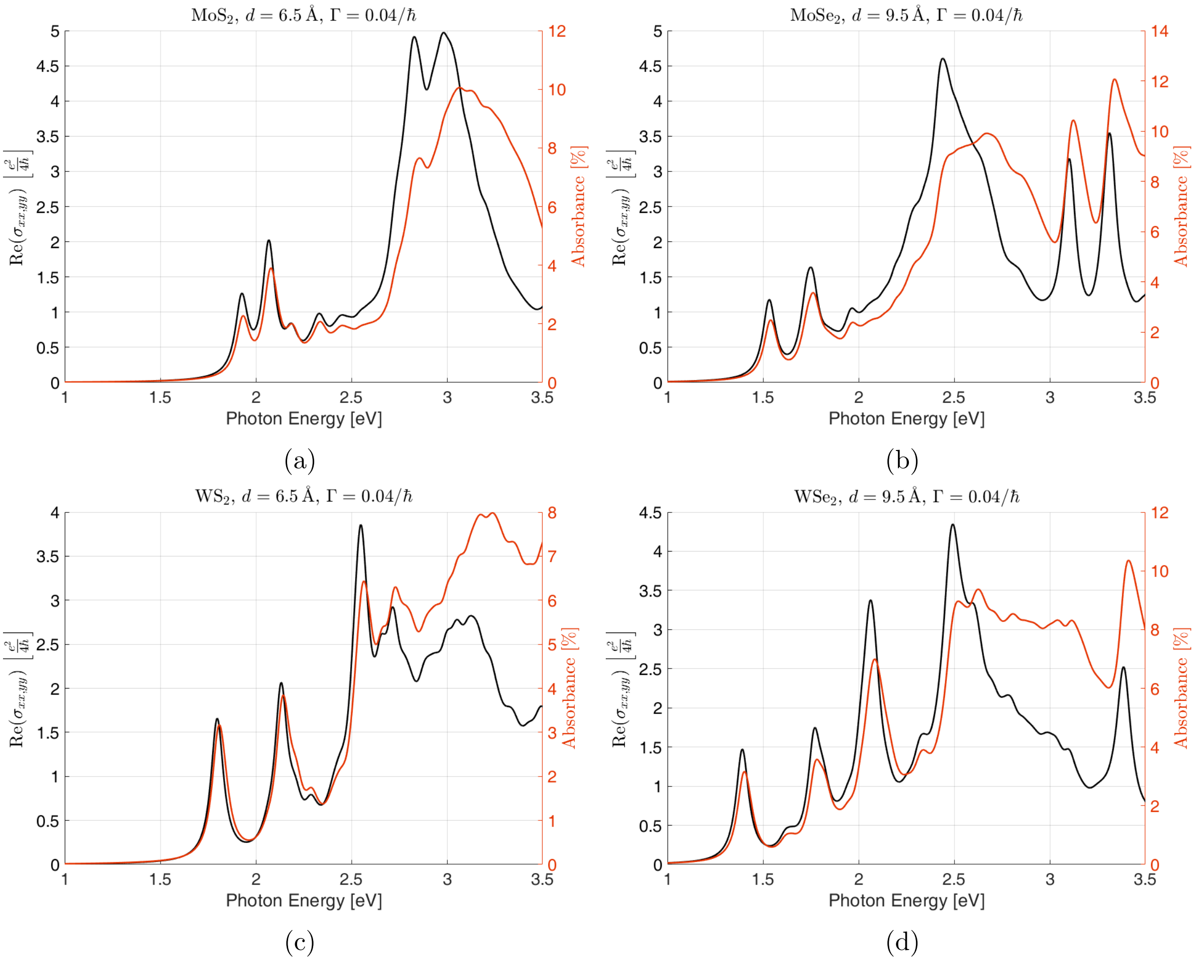

(a) (b)

(c) (d)

Figure 4.2.2: The sheet conductivity and absorbance of (a) MoS$_2$, (b) MoSe$_2$, (c) WS$_2$, and (d) WSe$_2$.

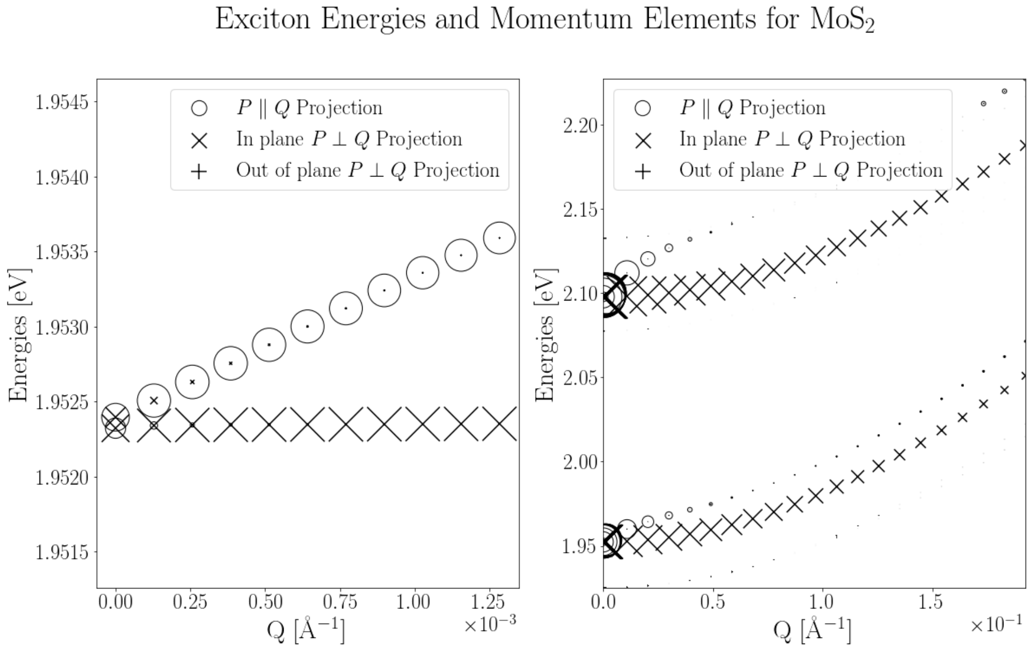

(a) MoS$_2$ - $M_p^* = 1.40m_e$

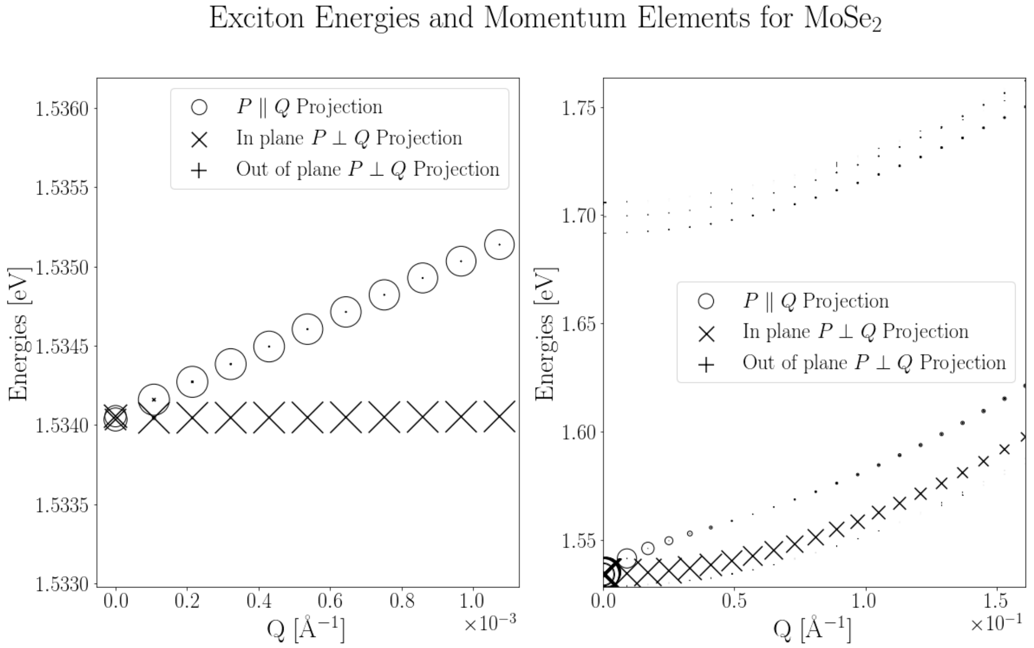

(b) MoSe$_2$ - $M_p^* = 1.53m_e$

Figure 4.2.3: Dispersion plots for (a) MoS$_2$ and (b) MoSe$_2$, fitted with a polynomial fit. The effective masses calculated as per equation (4.2.3) has been added to each plot. The plots also show the squared projection of the momentum matrix elements upon **Q** for each point. The larger the circle (cross) the more optical activity along the parallel (perpendicular) projection.

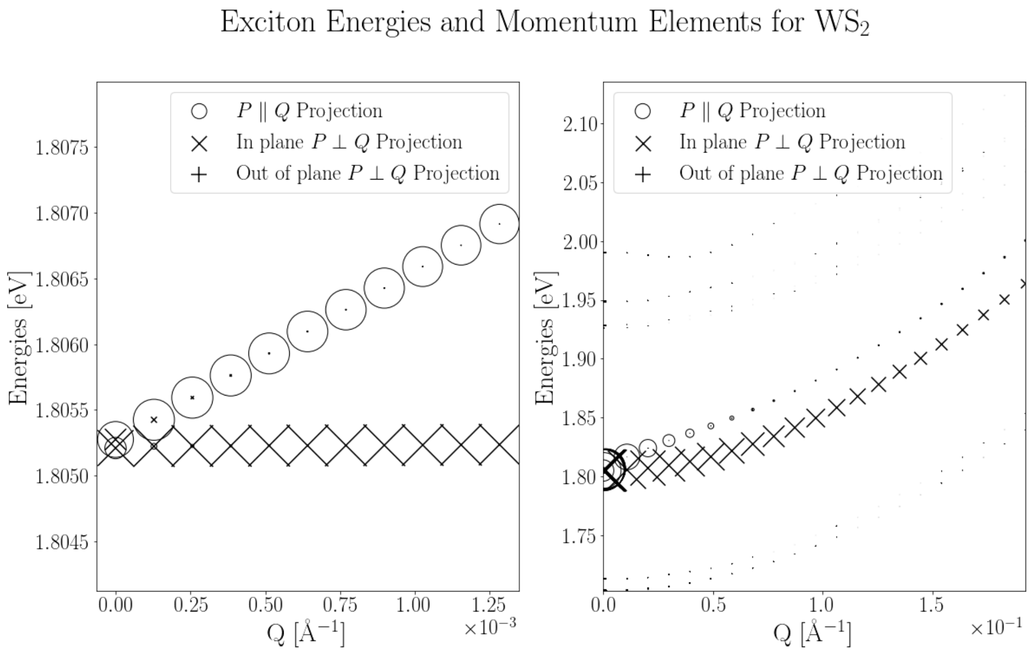

(a) WS$_2$ - $M_p^* = 0.867 m_e$

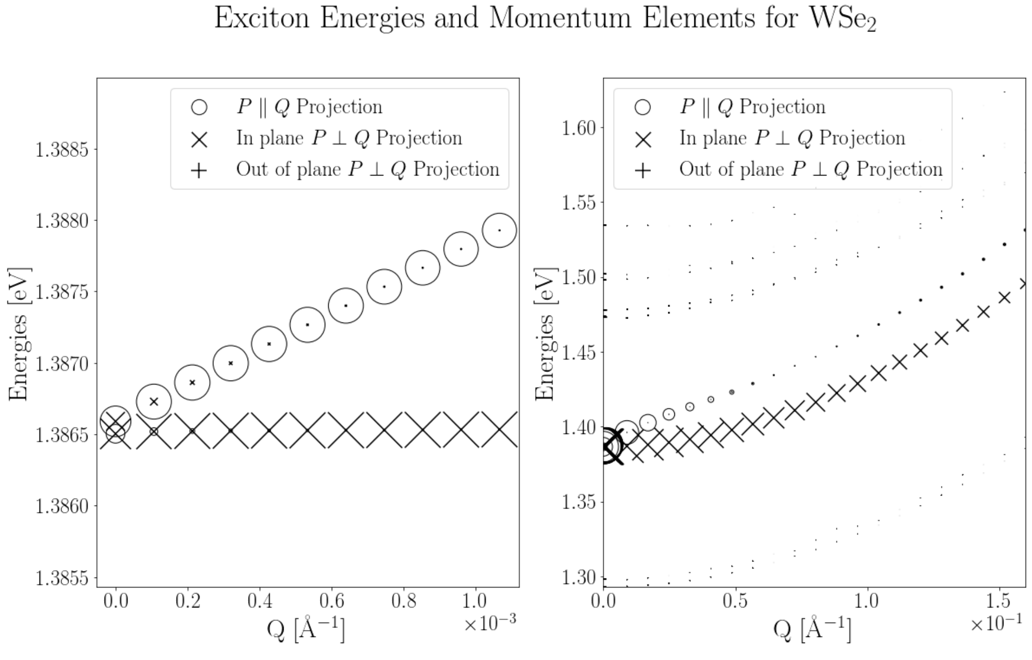

(b) WSe$_2$ - $M_p^* = 0.877 m_e$

Figure 4.2.4: Dispersion plots for (a) WS$_2$ and (b) WSe$_2$, fitted with a polynomial fit. The effective masses calculated as per equation (4.2.3) has been added to each plot. The plots also show the squared projection of the momentum matrix elements upon **Q** for each point. The larger the circle (cross) the more optical activity along the parallel (perpendicular) projection.

4.3 Emission Results for TMDs

This section will focus on the results of the emission model explained in section 3.5. Figure 4.3.1a shows the thermally averaged radiative lifetime at different temperatures for the different TMDs. It can be seen that the relation is mostly linear due to the prevalence of the parabolic band, in agreement with the articles [9, 10]. Figure 4.3.1b shows the angular dependence of emission. It can be seen that this spectrum is largely independent of the TMD in question.

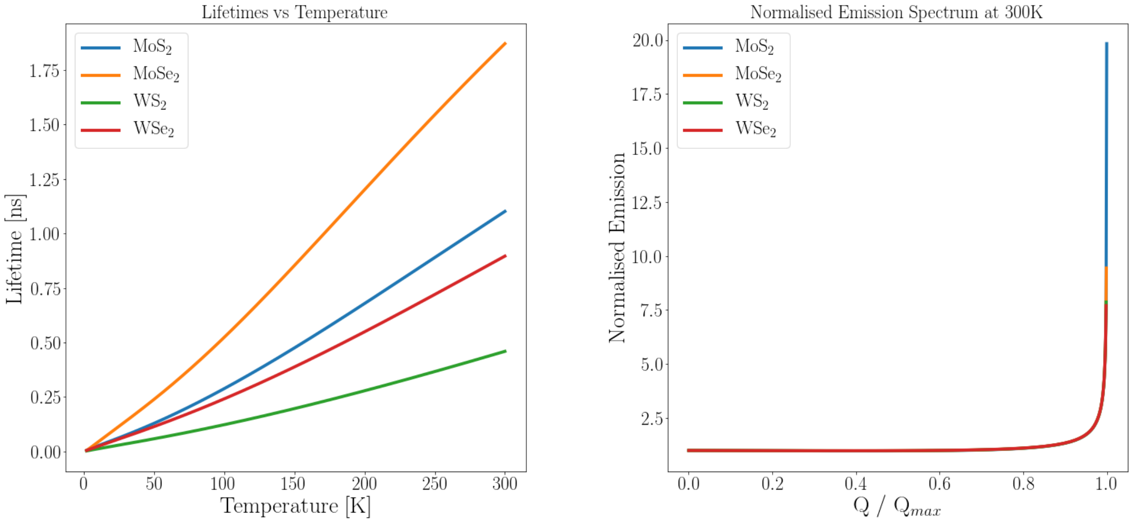

(a) (b)

Figure 4.3.1: (a): Calculated lifetimes for the different TMDs at different temperatures. (b): Calculated normalised emission $\Gamma(\mathbf{Q})/\Gamma_0$ at $T = 300\text{K}$, as a function of Q, where $Q_{\text{max}} = \omega/c \approx 0.9 \cdot 10^{-3}\text{Å}^{-1}$.

4.4 Purcell Effect on Lifetimes

In figure 4.4.1, the lifetimes for the four TMDs in various dielectric environment can be seen. The geometry is as displayed in figure 3.6.1 with $\varepsilon_1 = \varepsilon_2 = 1$ and a sapphire reflector with refractive index $n = 1.75$. These computations were performed using the Purcell effect procedure described in section 3.6. However, ε_a and ε_b used in computing the screened potentials for the BSE are still set equal to 1. These plots shows the general tendency a substrate close to the layer with dielectric constant ε_3 leads to a more extreme Purcell enhancement.

In figure 4.4.2, the lifetimes of the four TMDs can be seen inside the closed cavity configureation shown in figure 3.6.2. Here the bottom-most layer is set as a Bragg reflector of 16 alternating layers of TiO_2 ($n = 2.57$) and SiO_2 ($n = 1.46$), while the uppermost layer is set as sapphire with refractive index $n = 1.75$. The computations were done using the procedure outlines in section 3.6.2, with $\varepsilon_1 = 1$.

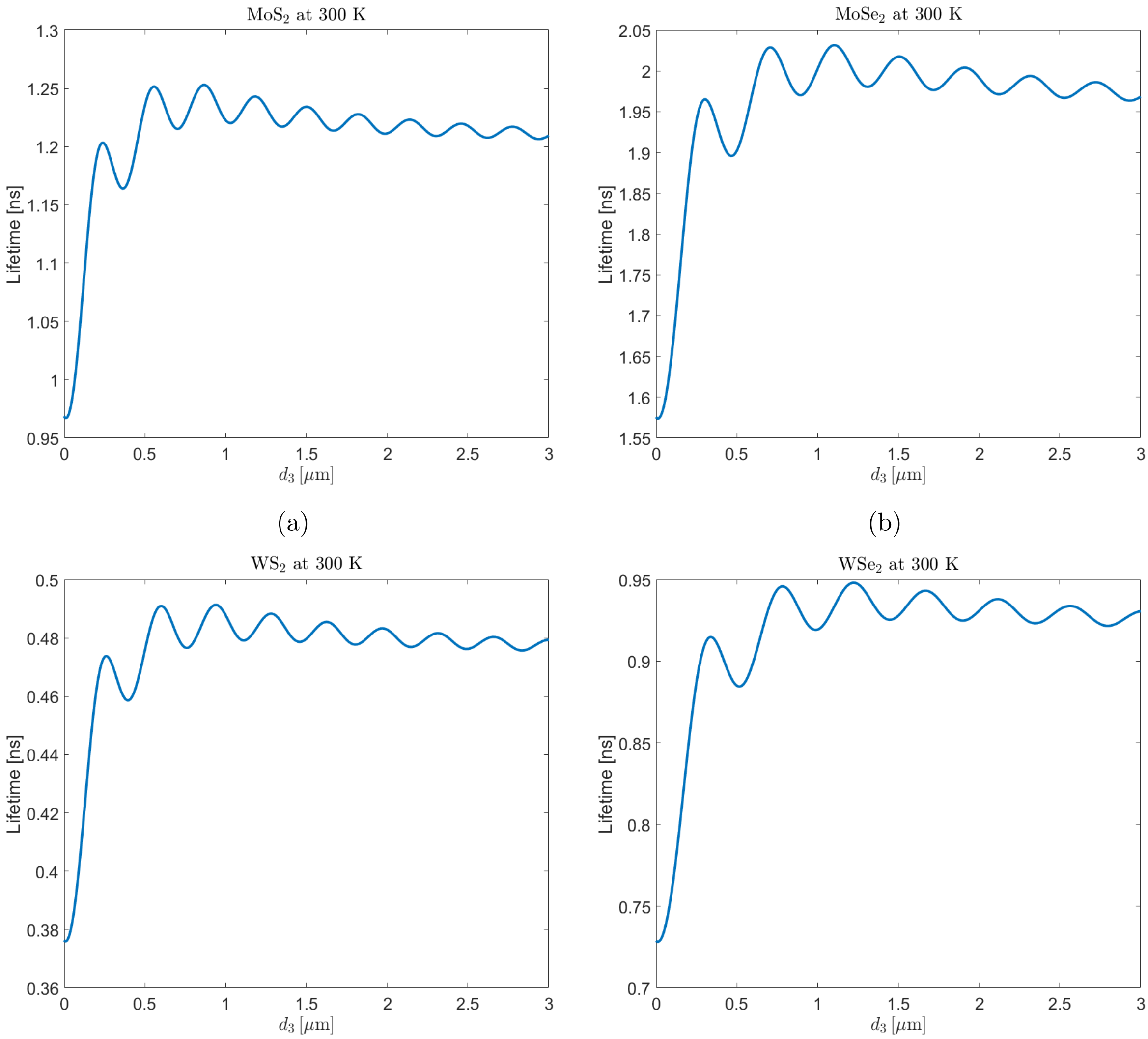

(a) (b)

(c) (d)

Figure 4.4.1: The Purcell effect on the lifetimes of (a) MoS$_2$, (b) MoSe$_2$, (c) WS$_2$, and (d) WSe$_2$ with respect to the distance (d in figure 3.6.1) to a sapphire ($n = 1.75$) reflector.

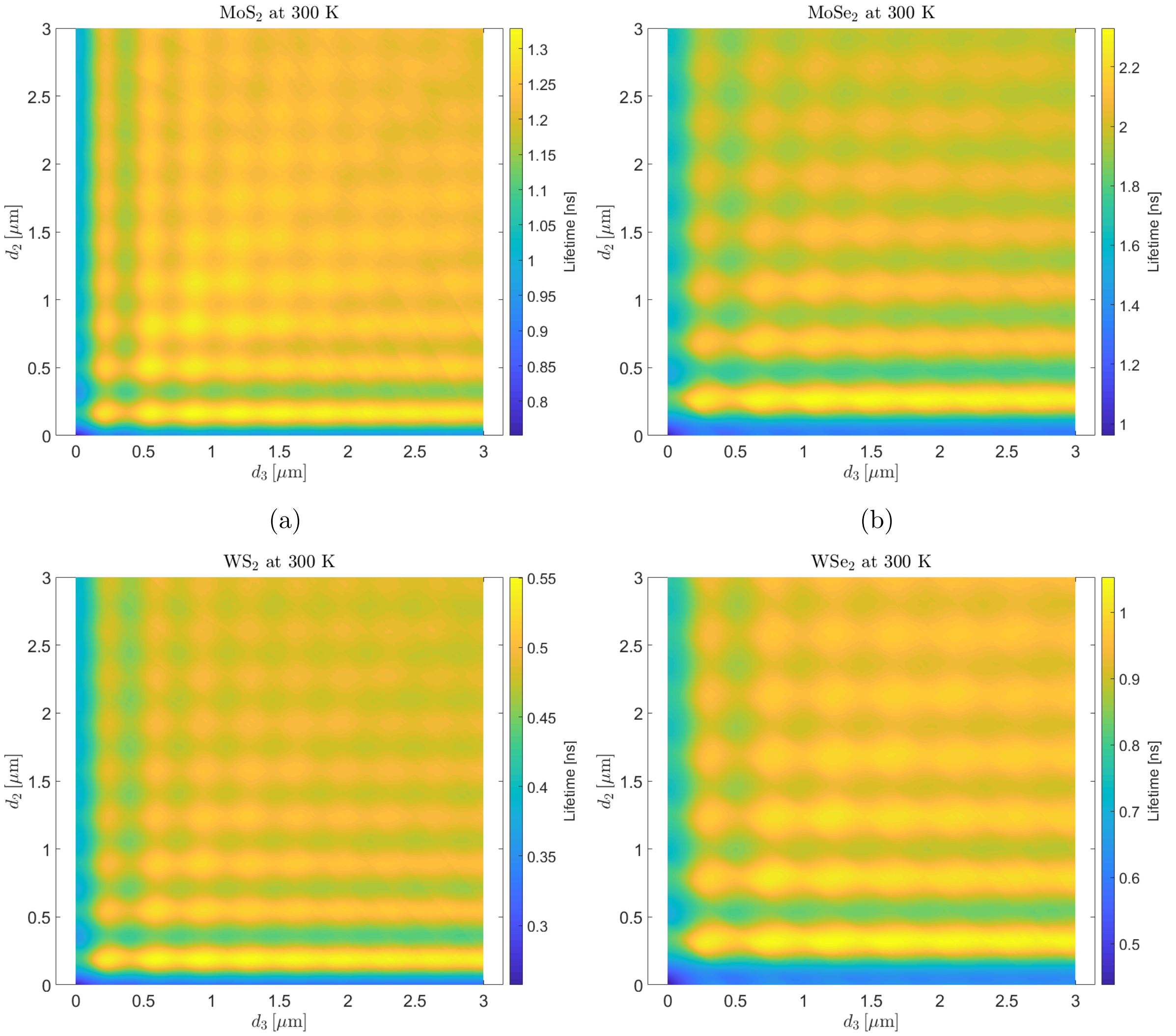

(a) (b)

(c) (d)

Figure 4.4.2: The Purcell effect on the lifetimes of (a) MoS$_2$, (b) MoSe$_2$, (c) WS$_2$, and (d) WSe$_2$ with respect to the distances to the cavity walls (d_1 and d_2 in figure 3.6.2). Here the upper wall is once again sapphire, while the bottom wall is a Bragg reflector with 16 layers of alternating TiO and SiO.

5 Discussion

This chapter seeks to discuss the many factors which have played significant roles in calculating the optical and radiative properties of the TMDs. Furthermore, measurements and calculations by other groups will be compared to the results obtained in this project and further discussed. In addition, the models used in this project will be applied to In_2Se_2 and C_2H_2 showing the versatility of the models. Finally, the many approximations and simplifications made in our model will be discussed.

5.1 Optical Spectra

The optical absorbance of MoS_2, as an example, can be compared to the optical absorbance found from BSE-calculations seen in C2DB [20]. There seems to be a lot of resemblance except for the C-peak at 3 eV, which peaks sharply to about 70% absorbance in the C2DB dataset. However, it is worth noticing that the C2DB absorbance was found using 4 × 4 bands and a cut-off energy of 50 eV compared to 2 × 2 spin-orbit hybridised bands and a cut-off energy of 600 eV in our case.

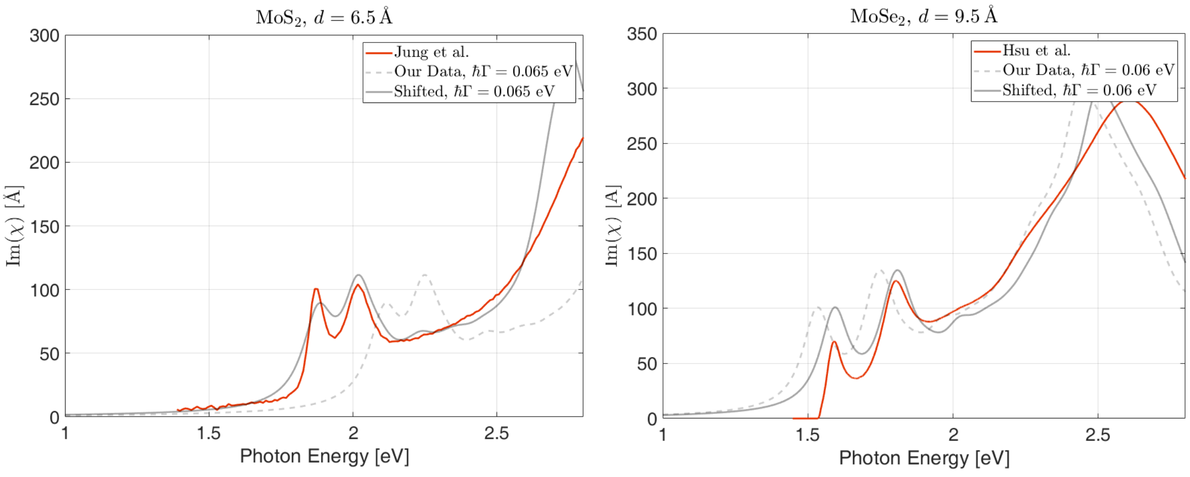

(a) (b)

Figure 5.1.1: Sheet susceptibility of molybdenum-based TMDs compared to experimentally obtained data.

Furthermore, it's interesting to compare our optical properties to experimental values. The sheet susceptibility is found as $\text{Im}\{\chi\} = 2nkd$, where $\tilde{n} = n + ik$ denotes the refractive index, and d denotes the layer thickness. In figures 5.1.1 and 5.1.2, we have used $d = 6.5$ Å for sulphur-based TMDs and $d = 9.5$ Å for selenide-based TMDs, since these choices seems to yield the best results for us. This should be compared to MoS_2-thicknesses of 6-7.5 Å and WSe_2-thicknesses of $\simeq 8$ Å [34, 35]. All TMDs except for $MoSe_2$ has been compared to data obtained by G. Jung

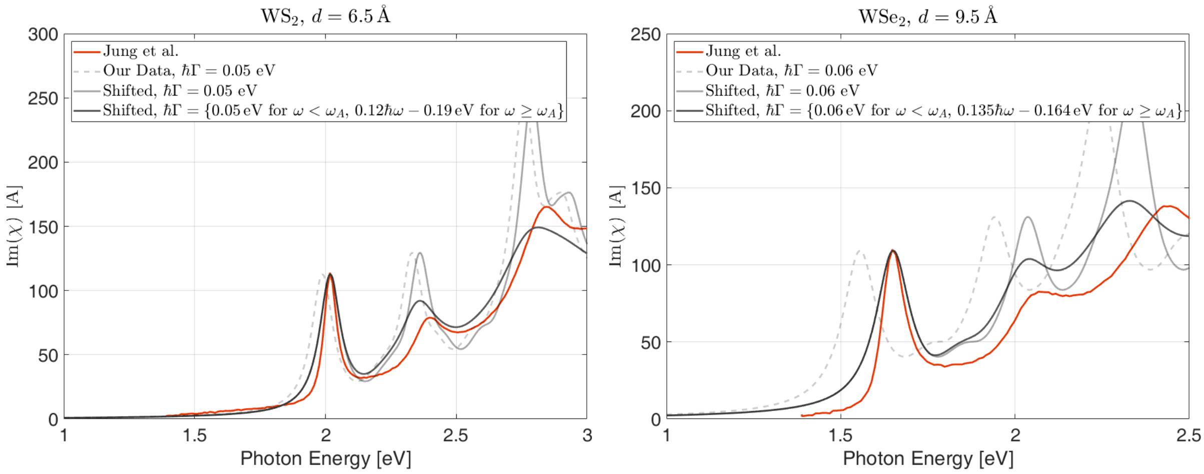

(a) (b)

Figure 5.1.2: Sheet susceptibility of tungsten-based TMDs compared to experimentally obtained data.

et al. [36], where they measure the refrative index of TMDs on sapphire using conventional spectroscopic ellipsometry. As such, our BSE calculations were performed using $\varepsilon_b = (1.76)^2$, which corresponds to A exciton resonance [37], but the GW bandgap is still based on vacuum parameters. As such, a shift is in the energies is expected and accounted for. In the case of MoSe$_2$, we have used experimental data found by C. Hsu et al. [38], where they measured the optical response on a SiO$_2$-substrate of varying thickness, and then extrapolated the data to find the vacuum response. Thus, our calculations were performed using $\varepsilon_b = 1$, and the data fits rather well, but a small shift in energy is still needed. For the tungsten-based TMDs, we have also tried using a Γ that varies linearly with ω, whenever ω exceeds the A exciton resonance, which seems to yield well-behaved correlation with the experimental data.

It is important to notice, that the refractive index of the substrate also varies with ω, which is not taken into consideration in these calculations. Moreover, we see improved correlation between our computations and experimental data, when we use $\Gamma = \Gamma(\omega)$, which to no surprise suggests that this might be the case.

Another important thing to note is the connection between the linewidth parameter Γ_w and the emission rate $\Gamma_e = \frac{1}{\tau}$, since broadening effects should be partially connected to the emission rate. In figure 4.2.2, we use $\Gamma_w = 0.04\,\text{eV}/\hbar \approx 6.08 \cdot 10^{13}\,\text{s}^{-1}$, this corresponds to a lifetime of $\tau_w = 1.65 \cdot 10^{-2}\,\text{ns}$. Presumably, other factors might play more significant roles in determining the broadening, such as structural defects, impurities and temperature broadening.

5.2 Exciton Dispersions

In figure 4.2.3 and 4.2.4, the exciton dispersions and effective masses of the lowest bright excitons can be seen. The effective masses can be compared to those attained from a more naive approach, that is, assuming the exciton effective mass is simply the sum of the effective masses of the holes and electrons. Thus, using data from [20], the effective masses should be

$$\begin{aligned}
\text{MoS}_2\text{:}\quad & M^*_{\text{sum}} = 0.43 + 0.53 = 0.96 \quad \text{BSE: } 1.40, && (5.2.1)\\
\text{MoSe}_2\text{:}\quad & M^*_{\text{sum}} = 0.49 + 0.58 = 1.07 \quad \text{BSE: } 1.53, && (5.2.2)\\
\text{WS}_2\text{:}\quad & M^*_{\text{sum}} = 0.33 + 0.34 = 0.67 \quad \text{BSE: } 0.867, && (5.2.3)\\
\text{WSe}_2\text{:}\quad & M^*_{\text{sum}} = 0.39 + 0.36 = 0.75 \quad \text{BSE: } 0.877. && (5.2.4)
\end{aligned}$$

For WS_2 and WSe_2 these results are fairly close to the effective masses obtained by fitting, however they are significantly lower than the masses obtained for MoS_2 and $MoSe_2$.

In an article by D. Y. Qiu et al. [39], they perform a similar calculation of the Q-dependence of energy for MoS_2. They similarly find a parabolic and a linear band. In addition, their parabolic fit yields a effective mass of $M_p^* \approx 1.4$. Furthermore, they explain the deviation between the naive approach to effective masses and the observed effective masses, by an effective Hamiltonian, which they fit the ab-initio calculations to, yielding an expressions for the parabolic- and linear band.

Similar results are found by T. Deilmann et al. [40]. They also perform a calculation for MoS_2, albeit this time including the parallel projection of the momentum elements. The article once again shows similar dispersions to those of this project, and furthermore the sizes of the momentum elements seem to agree. They also make calculations for the other TMDs presented in this project, which all agree with the tendencies of our results.

A few attempts at measuring these dispersions have been made. In particular for WSe_2, an article has been published by J. Hong et al. [41], where they use momentum resolved electron energy loss spectroscopy (q-EELS) to measure the dispersion. They find a parabolic dispersion with an effective mass of $M^*_{q\text{-EELS}} = 0.65$, which is significantly lower than the calculated effective mass. This deviation is expected to be caused by a combination of the silicon substrate the measurements were made upon and an error introduced by the scissor shift approximation. In particular, when comparing the DFT to the G0W0 calculations of C2DB, the valence band seems to have a significantly lower effective mass for the G0W0 calculation. In an article by M. Schneider et al. [42], they attempt to measure the dispersion for WSe_2 optically and obtain very low values of this effective mass. An obvious problem of measuring the dispersion optically is of course the optical momentum limit, meaning that the curvature of the parabolic dispersion is insoluble compared to the optical broadening at the effective masses predicted in this project. Furthermore, an explanation for extremely low observed values of the effective masses could be the linear bands, as is also proposed in the article.

5.3 Emission

In figure 4.3.1a, the excitonic lifetimes' dependence on the temperature, for different types of TMDs, can be seen. As expected from section 3.5.1, the dependence is somewhat linear, which has also been concluded in different kinds of literature [9, 10, 43]. When comparing our theoretically obtained lifetimes with the lifetimes obtained experimentally, seen in table 5.1, our lifetimes generally undershoot the experimental measurements. Some of this can be attributed to the fact that our calculations are for TMDs in vacuum, while all experimental data found, is for TMDs placed on a quartz or a silicon substrate. However, if we were to include effects arising from the dielectric environment, the calculations would be considerably more intricate. First of all, the pseudo-energy and BSE calculations would need a screened potential incorporating the substrate. Moreover, the Purcell enhancement discussed in chapter 2.4 would need to be included as well. To get a grasp on how crucial the Purcell enhancement is, one should look at figure 4.4.1, where it can be seen that the lifetime can vary significantly with an in- or decrease in the distance from the reflector.

Table 5.1: Experimental and theoretical lifetimes of examined TMDs at 300 K. The data needed to calculate the lifetimes of MoS_2, $MoSe_2$, WS_2 and WSe_2 were found using the conventional method of time-resolved photoluminescence (PL). When measured upon, MoS_2, $MoSe_2$ and WSe_2 were all placed on a SiO_2 ($n = 1.45$) substrate and WS_2 was placed on a SiO_2 ($n = 1.45$) - silicon ($n = 3.96$) substrate.

	Experimental	Theoretical
MoS_2	2 ± 0.1 ns [44] or 3 ± 1 ns [17]	1.10 ns
$MoSe_2$	900 ps [45]	1.87 ns
WS_2	805 ± 37 ps [46] or $\tau_1 \approx 248$ ps and $\tau_2 \approx 800$ ps [47]	0.46 ns
WSe_2	4 ns [12] or 4.1 ns [48]	0.87 ns

It is worth pointing out that photoluminescence varies significantly with the defects and impurities of the sample [12]. Moreover, the calculations of this project do not take the existence of dark states below bright excitonic states into account. The low energy dark excitons can significantly reduce the number of bright excitons at thermal equilibrium, and therefore PL measurements can give an "effective" radiative lifetime orders of magnitude longer than the intrinsic radiative lifetime of the purely bright excitons [12].

5.3.1 General Defects

There is a significant difference between the perfect intrinsic 2D structured TMDs and the ones manufactured in practice. Manufactured TMDs will have a number of possible impurities, which have effects on the electronic properties. The most common structural defect in TMDs are vacancies [49]. In MoS_2, sulphur vacancies will create unpaired electrons, resulting in n-doping the material, which will form a non-zero density of occupied states in the bandgap. In addition to sulphur vacancies, molybdenum vacancies may also occur, which will p-dope the material, and it has been shown that a single sample of MoS_2 can exhibit both vacancies in different areas of the sample [50].

Less dominating defects in TMDs are other atomic species replacing vacancies in the lattice, which can result in further p- or n-doping. Furthermore, since the TMDs can have edges and ripples on the surface, as well as the TMDs folding onto themselves. Therefore, the TMDs will not have a perfect infinite periodicity, which will have an effect on the electronic properties [49]. Overall, these defects have been found to result in two effects regarding the excitonic lifetime in TMDs, namely creating a defect-mediated non-radiative Auger decay process [14], and creating dark states with a significantly longer lifetime [17, 51]. The first of these effects is usually counteracted by passivating the chalcoginide vacancies by using either superacid treatment or voltage gating [13–16]. Furthermore, the second of these defects has been counteracted by further chemical treatment as shown in the article by H. M. Bretscher [17]. In addition, C. Jin et al. [12] postulates that for WSe_2 at exciton A resonance, only ≈ 4% of the states remain bright at room temperature.

Both the experimental values for MoS_2 [17, 44] were measured on a SiO_2 substrate, using either a superacid or gate voltage to prevent sulphur vacancies and chemically treated the sample to prevent dark states. H. L. Pradeepa et al. [44], who found the lifetime to be 2 ns, mechanically exfoliated the sample onto the substrate, whereas H. Bretscher et al. [17], who found a lifetime of 3 ns, chemically grew their sample on the substrate. Thus, experimental data where the sample is chemically grown, and where vacancies and dark states have been diminished, seem to agree with our data the most. The remaining experimental data from table 5.1, only takes a few or none of the aforementioned affecting factors into account, and this experimental data does indeed deviate significantly from our theoretical data.

5.3.2 Intrinsic Radiative Decay and Spin-Forbidden Dark States

In an article by C. Robert et al. [52], they measured the lifetime of $MoSe_2$ and WSe_2 at temperatures as low as 7 K. They found that for these extremely low temperatures, the defect assisted decay processes are negligible compared to the radiative decay, allowing for measurements of the intrinsic radiative decay rate. Furthermore, they find that at temperatures below 40 K, the decay rate is much faster than the time it takes to reach a thermal quasi-equilibrium. Using this, they measured the intrinsic radiative lifetimes to be $\tau_{rad}^0 = 1.8 \pm 0.2\,\mathrm{ps}$ for $MoSe_2$ and $\tau_{rad}^0 = 2.0 \pm 0.2\,\mathrm{ps}$ for WSe_2. These values should be compared to the quantity $\frac{1}{\Gamma_0}$, that is the non-thermally distributed lifetime, which in our case is $0.42\,\mathrm{ps}$ for $MoSe_2$ and $0.29\,\mathrm{ps}$ for WSe_2. Explanations for this deviation can, among other, be thermal scattering and the linewidth and pulse-time of the excitation laser, which changes the initial distribution of excitons. Furthermore, in the article they conclude that the result for WSe_2 is unreliable due to spin-forbidden dark states beneath the bright excitonic states. However, they wrongly conclude that since DFTs and G0W0 calculations for $MoSe_2$ show that the band-gap is spin-allowed, then the lowest energy exciton should be aswell. The BSE-calculations of this project, as well as others [53], show that the lowest exciton state for all the TMDs presented in this project is a dark state.

5.3.3 The Quasi Equilibrium Assumption

Another approximation used in the computation of the radiative lifetimes is the thermal averaging seen in equation (3.5.21). It suggests a thermal equilibrium of the excitonic states, but excitonic states should not be able to be in such an equilibrium, since they in their very existence are (thermal) excitations. Thus, what we use can perhaps be described as a thermal quasi-equilibrium, which is to be understood as the thermal equilibrium of the excitonic states. This should however be a decent approximation, if the thermal scattering is much faster that the emission rate, which should be the case at room temperature since the phonon scattering scales with temperature.

In an article by A. O. Slobodenuik et al. [54], they study the thermal distribution of an excitonic reservoir in a 2D material. They find different cases depending on the emission rate and phonon scattering rate, where in some cases it is possible for a depletion of the optically active part of the reservoir to happen. This especially happens at low temperatures, which causes the phonon scattering rate to become the dominant part of the emission process. This could be a possible explanation of the results obtained in the article [52], where for low temperatures a reciprocal proportionality to temperature is observed. However, at room temperature the phonon scattering rate is expected to be fast enough for the quasi equilibrium assumption to hold true.

5.3.4 Biexcitons and Trions

The calculations in this project take no regard to any excitation beyond the singly excited exciton. Thus, the effects of multiple excitons, trions, and biexcitons, which have proven prevalent in the TMDs presented in this project [16], are not taken into account. In the article by D. Lien et al. [16], they study the effect on the quantum yield of these effects, where they found that biexcitons start dominating at high exciton generation rates, meaning that effects of these could have played a significant role on the measurements referred to in the previous sections. Furthermore, trions are of particular importance due to the often n-doped nature of TMDs, offering free electrons to the formation of these. The exact effect of biexcitons and trions are difficult to quantify in terms of emission rate, however they significantly add to the difficulty of obtaining reliable measurements of the intrinsic exciton emission.

5.4 Purcell Effect

The dielectric geometry seen in figure 4.4.1 is extremely simple, but still shows the importance of the Purcell effect attributed from a substrate. In particular, it shows that the substrate can significantly improve the emission rate of the emitter placed upon it. In an article by J. Horng et al. [18], a slightly more complicated geometry is used as they experimentally consider $MoSe_2$ encapsulated in hBN. Compared to figure 3.6.2, they use sapphire as ε_3, while ε_2 corresponds to a Bragg reflector of alternating SiO_2 and TiO_2 layers [19]. As they vary the mirror distance, d_3, of a vacuum layer (corresponding to our ε_1), they measure the reflection contrast of the entire geometry. At the A excitonic resonance, they observe a periodic dependence (with some broadening) ranging all the way from nearly 0% absorption to almost 100% with respect to d, which can be attributed to the Purcell effect. At distances corresponding to low absorption, the $MoSe_2$-layer most likely reaches an excitonic saturation, meaning all the available excitonic states at that energy are occupied. For the sections of high absorption, the opposite is then thought to be the case, namely that the emission rate is much faster than the absorption rate, making absorption possible. In figure 4.4.2, we also see some periodicity in the lifetime with respect to distance, which might oscillate sufficiently in amplitude to allow for switching between the two extremes of saturation.

In a more naive approach, one might choose to simply model the Purcell enhancement of 2D-materials based on the assumption of a point dipole as opposed to our planar dipole. This would lead to the following expression for the Purcell enhancement of a point dipole near a surface [22, ch. 33], namely

$$P_{\parallel} = 1 + \frac{3}{4q_1}\mathrm{Re}\left\{ \int_0^{\infty} \frac{q_\rho}{q_{z1}} \left(r^{(s)} - r^{(p)} \frac{q_{z1}^2}{q_1^2} \right) \mathrm{e}^{2iq_{z1}d} dq_\rho \right\}, \tag{5.4.1}$$

$$P_{\perp} = 1 + \frac{3}{2q_1^3}\mathrm{Re}\left\{ \int_0^{\infty} \frac{q_\rho^3}{q_{z1}} r^{(p)} \mathrm{e}^{2iq_{z1}d} dq_\rho \right\}, \tag{5.4.2}$$

where the subscript denotes the orientation of the dipole with respect to the surface. Clearly, this does not incorporate the $\mathbf{Q}$-dependence similarly to what we find, instead the Purcell enhancement is found identically for all $\mathbf{Q}$, which is then multiplied by the vacuum emission rate.

A strength of having the field described in a Green's formalism is that one can easily generalise the formulas to more complicated and advanced geometries. These formulas are rarely solvable analytically, however there exists a rich field of methods for solving these numerically using volume and surface integration methods [55]. Practically, this is done by replacing equation (2.4.9) with the more general expression [55]

$$\overleftrightarrow{\mathbf{G}}^{(i)}(\mathbf{r}, \mathbf{r}') = \left(\overleftrightarrow{\mathbf{I}} + \frac{1}{k^2}\nabla\nabla \right) \frac{\mathrm{e}^{ik|\mathbf{r}-\mathbf{r}'|}}{4\pi|\mathbf{r}-\mathbf{r}'|}. \tag{5.4.3}$$

This then allows for efficiently modelling the Purcell enhancement of complicated structures, and furthermore allows for said structures to be periodic or set in a layered reference geometry.

A noteworthy remark regarding the Purcell calculations of this project is, that none of them take evanescent waves into account. Naturally, it should be expected that when the emitter is enclosed in a narrow cavity, that such waves will have a significant effect. However, in the case of vacuum surroundings, they should play no role at all.

5.5 Other 2D Materials

The parabolic and linear band observed for MoS_2, $MoSe_2$, WS_2, and WSe_2 are naturally not a general property for all 2D-materials, rather most materials don't have this attribute due to their bandgap not being centered at a spin symmetric k-point. A direct semiconductor with only a parabolic band could be C_2H_2, which has a bandgap around the Γ-point of symmetry. Furthermore, many 2D materials are indirect semiconductors, which also changes their emission profiles significantly. One such material could be In_2Se_2, which has an indirect bandgap centered around the Γ-point of symmetry. The energies and momentum elements can be seen in figure 5.5.1. The mostly constant momentum elements and purely parabolic dispersion of C_2H_2 gives a linear temperature dependence for the optical lifetime calculations, as can be seen in figure 5.5.2b. On the other hand, the non Γ-centered pseudo ground-state for In_2Se_2 yields a reciprocal dependence on the temperature, as shown in figure 5.5.2a.

In an article by T. Venanzi et al. [56], they measure on few layer InSe, where they also find a reciprocal dependence on temperature for the lifetime. Furthermore, in the measurements taken at $T = 4\,\mathrm{K}$, they find that the lifetimes for few layer InSe grows very large, around 400 ns, as expected due to the indirect bandgap. This is in accordance with the well known fact that In_2Se_2 approaches a direct bandgap, as the crystal approaches bulk. In our model, the lifetime at $T = 4\,\mathrm{K}$ grows huge, however measurements will measure significantly lower lifetimes due to phonons and defects. Furthermore they also measure the temperature dependence of 24-layer InSe where they also find a reciprocal temperature dependence in accordance with 5.5.2a.

It is worth noticing that while the assumption that the angular dependence of Q is irrelevant for the TMDs shown in this project, the same may not be true for other materials such as In_2Se_2 and C_2H_2, potentially adding some error to the optical lifetimes presented here.

The reciprocal temperature dependence for In_2Se_2 seen in figure 5.5.1a can be explained fairly simply from the Boltzmann factor, and can be described by considering the system as a two-band system involving an optically active band of constant energy $E_1(Q) = \varepsilon_1$ for $Q < \omega/c$ and a non-optical active parabolic band of energy, centered around the indirect bandgap Q_{ind}, $E_2(Q) = \frac{\hbar^2(Q-Q_{ind})^2}{2M}$. Defining $\gamma = \sqrt{\frac{\hbar^2}{Mk_BT}}$, the partition functions can then be expressed as

$$Z_1 = \sum_{Q<\omega/c} \mathrm{e}^{-\frac{\varepsilon_1}{k_BT}} \simeq \frac{A\mathrm{e}^{-\frac{\varepsilon_1}{k_BT}}\omega^2}{4\pi c^2}, \tag{5.5.1}$$

$$Z_2 = \sum_{Q} \mathrm{e}^{-\frac{1}{2}\gamma^2(Q-Q_{ind})^2} \simeq \frac{A}{2\pi}\left(\frac{\mathrm{e}^{-\frac{1}{2}\gamma^2 Q_{ind}^2}}{\gamma^2} + \frac{1}{\gamma}\sqrt{\frac{\pi}{2}}Q_{ind}\left(1 + \operatorname{erf}\left(\frac{1}{\sqrt{2}}\gamma Q_{ind}\right)\right)\right) \tag{5.5.2}$$

$$\simeq \frac{A}{2\pi}\left(\frac{1}{\gamma^2} + \frac{1}{\gamma}\sqrt{\frac{\pi}{2}}Q_{ind} + Q_{ind}^2\right) =: \frac{A}{2\pi}f(\gamma), \tag{5.5.3}$$

$$\frac{1}{Z_1 + Z_2} = \frac{2\pi}{A}\frac{1}{f(\gamma) + \frac{\omega^2}{2c^2}\mathrm{e}^{-\frac{\varepsilon_1}{k_BT}}}. \tag{5.5.4}$$

To calculate the emission rate, one needs only to sum over the optically active band. Assuming the momentum element to be constant for $Q < \omega/c$, as well as utilising the fact that it is always perpendicular to $\mathbf{Q}$ and parallel to z, the $\mathbf{Q}$-dependent 2D emission rate can be found as

$$\Gamma_{2D}(\mathbf{Q}) = 2\Gamma_0\frac{Q^2 c}{q_z\omega}, \tag{5.5.5}$$

where Γ_0 is defined as in equation (3.5.1). Equation (5.5.5) only holds true for $\mathbf{P}_{exc} \parallel z$. The

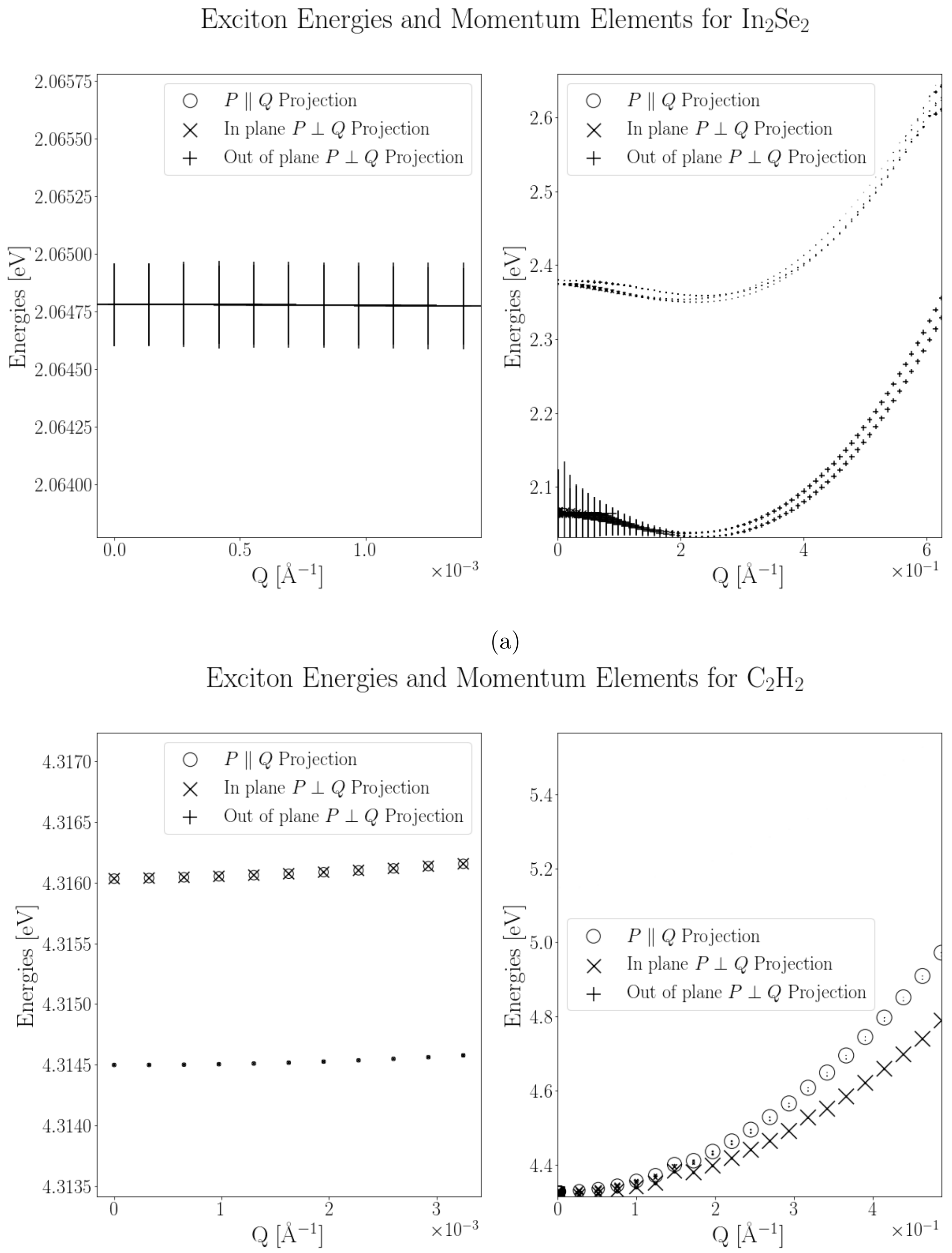

(a)

(b)

Figure 5.5.1: Dispersion plots for (a) In$_2$Se$_2$ and (b) C$_2$H$_2$. The plots also show the squared projection of the momentum matrix elements upon $\mathbf{Q}$ for each point. The larger the circle (cross) the more optical activity along the parallel (perpendicular) projection.

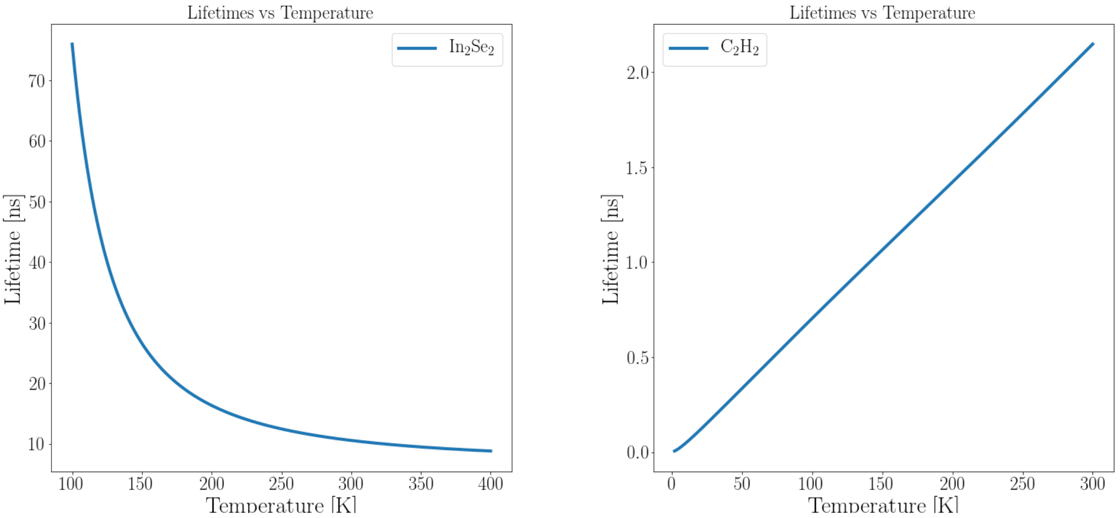

(a) (b)

Figure 5.5.2: Plots of the lifetime with respect to temperature of (a) In_2Se_2 and (b) C_2H_2, based on the dispersion plots in figure 5.5.1.

emission rate is

$$\langle\Gamma\rangle = \left(\frac{1}{f(\gamma)+\frac{\omega^2}{2c^2}\mathrm{e}^{-\frac{\varepsilon_1}{k_BT}}}\right)\int_0^{\omega/c} 2\Gamma_0 \frac{Q^2c}{\omega}\left(\frac{\omega^2}{c^2}-Q^2\right)^{-1/2} \mathrm{e}^{-\frac{\varepsilon_1}{k_BT}} Q dQ \tag{5.5.6}$$

$$= \frac{\Gamma_0\frac{4\omega^2}{3c^2}\mathrm{e}^{-\frac{\varepsilon_1}{k_BT}}}{f(\gamma)+\frac{\omega^2}{2c^2}\mathrm{e}^{-\frac{\varepsilon_1}{k_BT}}}. \tag{5.5.7}$$

The lifetime is then the reciprocal of this

$$\tau = \Gamma_0^{-1}\left(\frac{3}{8}+\frac{3c^2}{4\omega^2}\left(\frac{1}{\gamma^2}+\frac{1}{\gamma}\sqrt{\frac{\pi}{2}}Q_{ind}+Q_{ind}^2\right)\mathrm{e}^{\frac{\varepsilon_1}{k_BT}}\right) \tag{5.5.8}$$

$$= \frac{3\Gamma_0^{-1}}{8}\left(1+\frac{2c^2}{\omega^2}\left(\frac{Mk_BT}{\hbar^2}+\sqrt{\frac{\pi M k_BT}{2\hbar^2}}Q_{ind}+Q_{ind}^2\right)\mathrm{e}^{\frac{\varepsilon_1}{k_BT}}\right). \tag{5.5.9}$$

Most of these quantities can be approximated directly from a DFT bandstructure and a BSE calculation for $Q = 0$. Setting $M = 3m_e$, $Q_{ind} = 0.25\,\text{Å}^{-1}$, $\omega = \frac{2.05\,\text{eV}}{\hbar}$, $\varepsilon_1 = 50\,\text{meV}$ and $\Gamma = 1.662 \cdot 10^{13}\,s^{-1}$, yields the plot of figure 5.5.3. Finally, we have calculated the both the in-plane and out-of-plane elements of the sheet conductivity tensor and optical absorption for In_2Se_2, which can be seen in figure 5.5.4. As expected, the lowest exciton peak is z-polarised. Comparing to C2DB the results show many of the same features, with some differences, expected to be caused by the Keldysh screening used in our calculation.

In an article by Han-Chin Cha et al. [57], they perform spectroscopic and microscopic measurements on monolayer flakes of In_2Se_2, which have been obtained through chemical vapor deposition. In their optical absorption spectra they see a large broadening, where no visible peaks in the area between 1 eV and 4 eV can be distinguished. This broadening can be due to aforementioned factors such as structural defects, impurities and temperature broadening. We calculated the optical absorbance spectra of 1-layer In_2Se_2, which can be seen on figure 5.5.5, where the thickness d was set to 16.93 Å, which is the lattice parameter they measure in the article [57]. It can be seen that, for a large broadening, $\hbar\Gamma = 0.35$ eV, our calculated result are

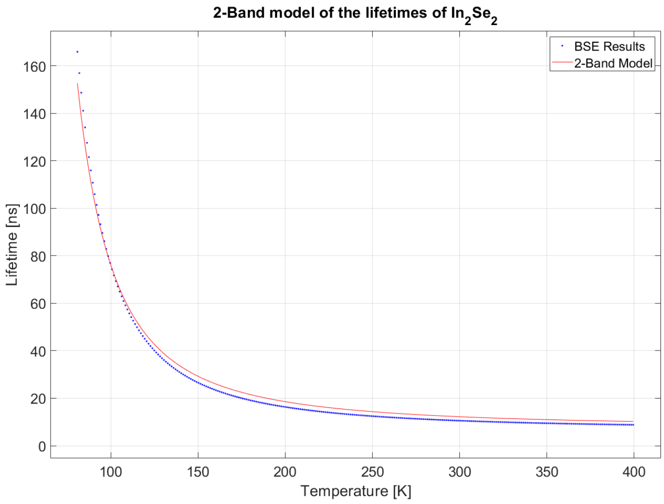

Figure 5.5.3: Comparison between the calculated lifetimes for In_2Se_2, as calculated by the BSE-model and the simple 2D model of equation (5.5.9).

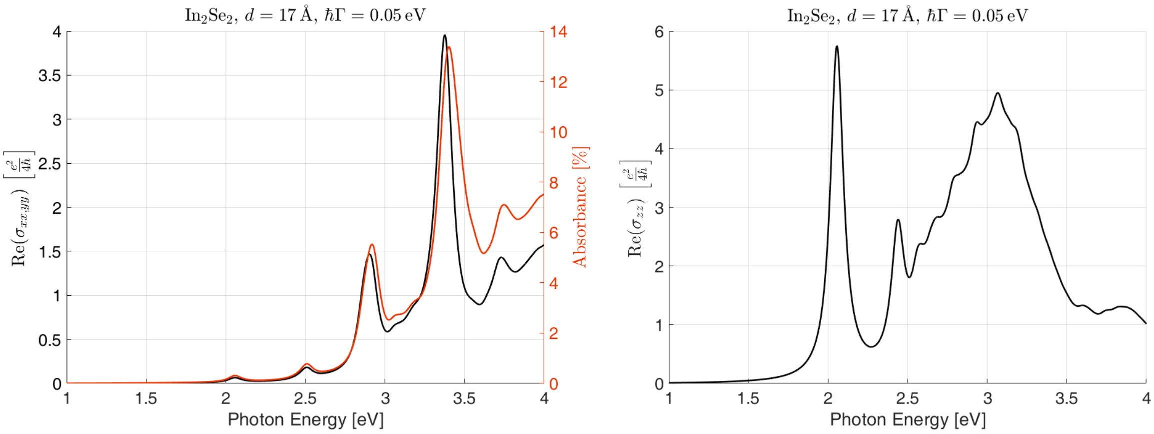

(a) (b)

Figure 5.5.4: Optical spectra of In_2Se_2 using $\hbar\Gamma = 0.05$ eV and 4×4 bands including spin-orbit hybridisation.

quite similar to the optical absorbance spectra in their article. They also measured a PL spectra where they found emission peaks at ≈ 2.4 eV, which they assigned to peak A, and a broad peak at 2.95 which the assigned to the B peak. These values are in terms of energy quite close the the peaks calculated in this project, with some shift due to the substrate.

5.6 Computational Handling

On the computational side of things there have been made a couple of approximations, which can introduce some amount of error to the calculations presented in this report. In particular, the approximation of using a Keldysh potential and scissor shift operator are among the most significant of these. Comparing the DFT and G0W0 results found in C2DB [20], one finds that the effective mass of the hole should be lower than that of the DFT, for all the TMDs presented. This in turn will reduce the effective mass of the exciton, and thus reduce the theorised lifetime. The effect of the Keldysh approximation is more complicated, but effectively it should have a

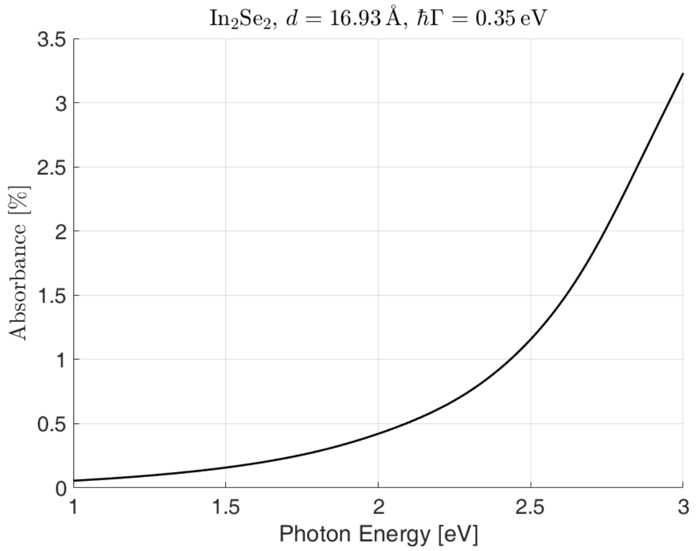

Figure 5.5.5: Optical absorbance spectra of 1-layer In_2Se_2.

delocalising effect on the exciton states. However, due to the strong localisation of the A and B excitons, these should not be affected much, in accordance with the comparisons discussed in section 5.1.

The calculation includes a lot of different parameters to converge, in order to obtain reliable results. These have been introduced throughout the implementation section, and seem to converge at the resolutions used in the presented calculations, however higher parameters are expected to improve results further and yield a slight correction to the results, which seems to be less than 5% for MoS_2. An example of this is that the linear and parabolic band should be entirely degenerate for $Q = 0$, but the results presented don't entirely reflect this due to numerical error.

6 Summary

In summary, we have presented a theoretical model for describing emission properties of TMDs, as well as other 2-dimensional semiconductors. The model implements a Bethe-Salpeter calculation based on a scissor-shifted DFT calculation, where the reciprocal space is interpolated to achieve a semi-continuous k-point grid allowing for a continuous momentum calculation of optical calculations for a photon with momentum $\mathbf{q}$. This enables modelling the emission rates of the system based on a thermal quasi-equilibrium for the excitons, as well as obtaining an angular spectrum of normalised lifetimes. The angular spectrum as well as the emission rates are then used in an optical model, allowing for obtaining the Purcell factor of a layered optical environment. Furthermore, this calculation is also shown to be generalisable to any environment using the Green's function formalism.

From this model multiple results can be obtained. Firstly, the BSE results provide the basis for optical properties using linear perturbation theory, which shows good agreement with experimental data. Secondly, the interpolated semi-continuous BSE results provide the lifetime calculations which are found to be in the ns range, in agreement with experimental data. When considering all the external factors, as well as the Purcell factor, these results seem very reasonable. Finally, the Purcell calculations show a periodic tendency with respect to the distance between the source and reflector, which has also been shown experimentally.

7 References

[1] M. T., X. F., and A. P., "Graphene photodetectors for high-speed optical communications.," *Nature Photonics*, vol. 4, pp. 297–301, 2010. DOI: `https://doi.org/10.1038/nphoton.2010.40`.

[2] Z. Lin, Y. Liu, U. Halim, *et al.*, "Solution-processable 2d semiconductors for high-performance large-area electronics," *Springer Nature*, vol. 562, pp. 254–258, 2018.

[3] J. J. Mortensen, L. B. Hansen, and K. W. Jacobsen, "Real-space grid implementation of the projector augmented wave method," *Phys. Rev. B*, vol. 71, p. 035 109, 3 Jan. 2005. DOI: `10.1103/PhysRevB.71.035109`. [Online]. Available: `https://link.aps.org/doi/10.1103/PhysRevB.71.035109`.

[4] J. Enkovaara, C. Rostgaard, J. J. Mortensen, *et al.*, "Electronic structure calculations with GPAW: A real-space implementation of the projector augmented-wave method," *Journal of Physics: Condensed Matter*, vol. 22, no. 25, p. 253 202, Jun. 2010. DOI: `10.1088/0953-8984/22/25/253202`. [Online]. Available: `https://doi.org/10.1088%2F0953-8984%2F22%2F25%2F253202`.

[5] J. Yan, J. J. Mortensen, K. W. Jacobsen, and K. S. Thygesen, "Linear density response function in the projector augmented wave method: Applications to solids, surfaces, and interfaces," *Phys. Rev. B*, vol. 83, p. 245 122, 24 Jun. 2011. DOI: `10.1103/PhysRevB.83.245122`. [Online]. Available: `https://link.aps.org/doi/10.1103/PhysRevB.83.245122`.

[6] A. H. Larsen, J. J. Mortensen, J. Blomqvist, *et al.*, "The atomic simulation environment—a python library for working with atoms," *Journal of Physics: Condensed Matter*, vol. 29, no. 27, p. 273 002, 2017. [Online]. Available: `http://stacks.iop.org/0953-8984/29/i=27/a=273002`.

[7] S. R. Bahn and K. W. Jacobsen, "An object-oriented scripting interface to a legacy electronic structure code," English, *Comput. Sci. Eng.*, vol. 4, no. 3, pp. 56–66, May 2002, ISSN: 1521-9615. DOI: `10.1109/5992.998641`.

[8] C. Rostgaard, "The projector augmented-wave method," 2009. arXiv: `0910.1921`.

[9] H. Wang, C. Zhang, W. Chan, C. Manolatou, S. Tiwari, and F. Rana, "Radiative lifetimes of excitons and trions in monolayers of the metal dichalcogenide mos2," *Physical Review B*, vol. 93, no. 4, Jan. 2016, ISSN: 2469-9969. DOI: `10.1103/physrevb.93.045407`. [Online]. Available: `http://dx.doi.org/10.1103/PhysRevB.93.045407`.

[10] M. Palummo, M. Bernardi, and J. C. Grossman, "Exciton radiative lifetimes in two-dimensional transition metal dichalcogenides," *Nano Letters*, vol. 15, no. 5, pp. 2794–2800, 2015, PMID: 25798735. DOI: `10.1021/nl503799t`. eprint: `https://doi.org/10.1021/nl503799t`. [Online]. Available: `https://doi.org/10.1021/nl503799t`.

[11] L. Xu, L. Zhao, Y. Wang, M. Zou, Q. Zhang, and A. Cao, "Analysis of photoluminescence behavior of high-quality single-layer mos2," *Nano Research*, vol. 12, no. 7, pp. 1619–1624, Jul. 2019, ISSN: 1998-0000. DOI: `10.1007/s12274-019-2401-0`. [Online]. Available: `https://doi.org/10.1007/s12274-019-2401-0`.

[12] C. Jin, J. Kim, K. Wu, *et al.*, "On optical dipole moment and radiative recombination lifetime of excitons in wse2," *Advanced Functional Materials*, 2016, ISSN: 1616-301X. DOI: `10.1002/adfm.201601741`.

[13] M. Amani, P. Taheri, R. Addou, G. H. Ahn, D. Kiriya, D.-H. Lien, J. W. Ager, R. M. Wallace, and A. Javey, "Recombination kinetics and effects of superacid treatment in sulfur- and selenium-based transition metal dichalcogenides," *Nano Letters*, vol. 16, no. 4, pp. 2786–2791, 2016, PMID: 26978038. DOI: `10.1021/acs.nanolett.6b00536`. eprint: `https://doi.org/10.1021/acs.nanolett.6b00536`. [Online]. Available: `https://doi.org/10.1021/acs.nanolett.6b00536`.

[14] M. Amani, D.-H. Lien, D. Kiriya, *et al.*, "Near-unity photoluminescence quantum yield in mos2," *Science*, vol. 350, pp. 1065–1068, Nov. 2015. DOI: `10.1126/science.aad2114`.

[15] H. Kim, D.-H. Lien, M. Amani, J. W. Ager, and A. Javey, "Highly stable near-unity photoluminescence yield in monolayer mos2 by fluoropolymer encapsulation and superacid treatment," *ACS Nano*, vol. 11, no. 5, pp. 5179–5185, 2017, PMID: 28467698. DOI: `10.1021/acsnano.7b02521`. [Online]. Available: `https://doi.org/10.1021/acsnano.7b02521`.

[16] D.-H. Lien, S. Z. Uddin, M. Yeh, M. Amani, H. Kim, I. Ager, E. Yablonovitch, and A. Javey, "Electrical suppression of all nonradiative recombination pathways in monolayer semiconductors," May 2019.

[17] H. Bretscher, Z. Li, J. Xiao, *et al.*, "The bright side of defects in mos_2 and ws_2 and a generalizable chemical treatment protocol for defect passivation," Feb. 2020.

[18] J. Horng, Y. H. Chou, T. Chang, C.-Y. Hsu, T.-c. Lu, and H. deng, "Engineering effects of vacuum fluctuations on two-dimensional semiconductors," Mar. 2019.

[19] J. Horng, E. Martin, Y. H. Chou, *et al.*, "Perfect absorption by an atomically thin crystal," Aug. 2019.

[20] S. Haastrup, M. Strange, M. Pandey, *et al.*, "The computational 2d materials database: High-throughput modeling and discovery of atomically thin crystals," *2D Materials*, vol. 5, no. 4, p. 042 002, Sep. 2018, ISSN: 2053-1583. DOI: `10.1088/2053-1583/aacfc1`. [Online]. Available: `http://dx.doi.org/10.1088/2053-1583/aacfc1`.

[21] R. Loudon, *The Quantum Theory of Light.* Oxford: Clarendon Press, 1973.

[22] T. G. Pedersen, "Electric, optical & magnetic properties of nanostructures," Aalborg University, 2019.

[23] J. Dahl, *Introduction to the Quantum World of Atoms and Molecules.* World Scientific, 2001.

[24] M. Rohlfing and S. G. Louie, "Electron-hole excitations and optical spectra from first principles," *Phys. Rev. B*, vol. 62, pp. 4927–4944, 8 Aug. 2000. DOI: `10.1103/PhysRevB.62.4927`.

[25] B. H. L. Novotny, *Principles of Nano-Optics*, First Edition. Cambridge University Press, 2006.

[26] J. P. Perdew, K. Burke, and M. Ernzerhof, "Generalized gradient approximation made simple," *Phys. Rev. Lett.*, vol. 77, pp. 3865–3868, 18 Oct. 1996. DOI: `10.1103/PhysRevLett.77.3865`. [Online]. Available: `https://link.aps.org/doi/10.1103/PhysRevLett.77.3865`.

[27] J. Gusakova, X. Wang, L. Shiau, A. Krivosheeva, V. Shaposhnikov, V. Borisenko, V. Gusakov, and B. Tay, "Electronic properties of bulk and monolayer tmds: Theoretical study within dft framework (gvj-2e method)," *physica status solidi (a)*, vol. 214, p. 1 700 218, Sep. 2017. DOI: `10.1002/pssa.201700218`.

[28] T. Olsen, "Designing in-plane heterostructures of quantum spin hall insulators from first principles: 1t'-mos2 with adsorbates," English, *Physical Review B (Condensed Matter and Materials Physics)*, vol. 94, no. 23, 2016, ©2016 American Physical Society, ISSN: 1098-0121. DOI: `10.1103/PhysRevB.94.235106`.

[29] Z. H. Levine and D. C. Allan, "Linear optical response in silicon and germanium including self-energy effects," *Phys. Rev. Lett.*, vol. 63, pp. 1719–1722, 16 Oct. 1989. DOI: `10.1103/PhysRevLett.63.1719`. [Online]. Available: `https://link.aps.org/doi/10.1103/PhysRevLett.63.1719`.

[30] ——, "Quasiparticle calculation of the dielectric response of silicon and germanium," *Phys. Rev. B*, vol. 43, pp. 4187–4207, 5 Feb. 1991. DOI: `10.1103/PhysRevB.43.4187`. [Online]. Available: `https://link.aps.org/doi/10.1103/PhysRevB.43.4187`.

[31] Z. H. Levine, "One-electron formalism for second-harmonic generation in crystalline semiconductors," *Phys. Rev. B*, vol. 42, pp. 3567–3577, 6 Aug. 1990. DOI: `10.1103/PhysRevB.42.3567`. [Online]. Available: `https://link.aps.org/doi/10.1103/PhysRevB.42.3567`.

[32] Z. H. Levine and D. C. Allan, "Optical second-harmonic generation in iii-v semiconductors: Detailed formulation and computational results," *Phys. Rev. B*, vol. 44, pp. 12 781–12 793, 23 Dec. 1991. DOI: `10.1103/PhysRevB.44.12781`. [Online]. Available: `https://link.aps.org/doi/10.1103/PhysRevB.44.12781`.

[33] R. Del Sole and R. Girlanda, "Optical properties of semiconductors within the independent-quasiparticle approximation," *Phys. Rev. B*, vol. 48, pp. 11 789–11 795, 16 Oct. 1993. DOI: `10.1103/PhysRevB.48.11789`. [Online]. Available: `https://link.aps.org/doi/10.1103/PhysRevB.48.11789`.

[34] H. Li, J. Wu, X. Huang, G. Lu, J. Yang, X. Lu, Q. Xiong, and H. Zhang, "Rapid and reliable thickness identification of two-dimensional nanosheets using optical microscopy," *ACS Nano*, vol. 7, no. 11, pp. 10 344–10 353, 2013, PMID: 24131442. DOI: `10.1021/nn4047474`. [Online]. Available: `ttps://doi.org/10.1021/nn4047474`.

[35] E. Ridolfi, C. H. Lewenkopf, and V. M. Pereira, "Excitonic structure of the optical conductivity in mos2 monolayers," *Phys. Rev. B*, vol. 97, p. 205 409, 20 May 2018. DOI: `10.1103/PhysRevB.97.205409`. [Online]. Available: `https://link.aps.org/doi/10.1103/PhysRevB.97.205409`.

[36] G.-H. Jung, S. Yoo, and Q.-H. Park, "Measuring the optical permittivity of two-dimensional materials without a priori knowledge of electronic transitions," *Nanophotonics*, vol. 8, no. 2, pp. 263–270, 2018. [Online]. Available: `https://www.degruyter.com/view/journals/nanoph/8/2/article-p263.xml`.

[37] R. L. Kelly, "Program of the 1972 annual meeting of the optical society of america," *J. Opt. Soc. Am.*, vol. 62, no. 11, pp. 1336–1336, Nov. 1972. DOI: `10.1364/JOSA.62.001336`. [Online]. Available: `http://www.osapublishing.org/abstract.cfm?URI=josa-62-11-1336`.

[38] C. Hsu, R. Frisenda, R. Schmidt, A. Arora, S. M. de Vasconcellos, R. Bratschitsch, H. S. J. van der Zant, and A. Castellanos-Gomez, "Thickness-dependent refractive index of 1l, 2l, and 3l mos2, mose2, ws2, and wse2," *Advanced Optical Materials*, vol. 7, no. 13, p. 1 900 239, 2019. DOI: `10.1002/adom.201900239`. [Online]. Available: `https://onlinelibrary.wiley.com/doi/abs/10.1002/adom.201900239`.

[39] D. Qiu, T. Cao, and S. Louie, "Nonanalyticity, valley quantum phases, and lightlike exciton dispersion in monolayer transition metal dichalcogenides: Theory and first-principles calculations," *Physical review letters*, vol. 115, p. 176 801, Nov. 2015. DOI: `10.1103/PhysRevLett.115.176801`.

[40] T. Deilmann and K. S. Thygesen, "Finite-momentum exciton landscape in mono- and bilayer transition metal dichalcogenides," *2D Materials*, vol. 6, no. 3, p. 035 003, Apr. 2019. DOI: `10.1088/2053-1583/ab0e1d`. [Online]. Available: `https://doi.org/10.1088%2F2053-1583%2Fab0e1d`.

[41] J. Hong, R. Senga, T. Pichler, and K. Suenaga, "Probing exciton dispersions of freestanding monolayer wse2 by momentum-resolved electron energy-loss spectroscopy," *Physical Review Letters*, vol. 124, Feb. 2020. DOI: `10.1103/PhysRevLett.124.087401`.

[42] L. M. Schneider, S. S. Esdaille, D. A. Rhodes, K. Barmak, J. C. Hone, and A. Rahimi-Iman, "Shedding light on exciton’s nature in monolayer quantum material by optical dispersion measurements," *Opt. Express*, vol. 27, no. 26, pp. 37 131–37 149, Dec. 2019. DOI: `10.1364/OE.27.037131`. [Online]. Available: `http://www.opticsexpress.org/abstract.cfm?URI=oe-27-26-37131`.

[43] P. Maurizia, B. Marco, and G. J. C., "Exciton radiative lifetimes in two-dimensional transition metal dichalcogenides," *Nano Lett.*, vol. 15, no. 5, pp. 2794–2800, 2015. [Online]. Available: `https://doi.org/10.1021/nl503799t`.

[44] H. L. Pradeepa, M. Praloy, B. Aveek, and B. J. K., "Electrical and chemical tuning of exciton lifetime in monolayer mos2 for field-effect transistors," *ACS Applied Nano Materials*, vol. 3, no. 1, pp. 641–647, 2020. DOI: `10.1021/acsanm.9b02170`.

[45] N. Kumar, Q. Cui, F. Ceballos, D. He, Y. Wang, and H. Zhao, "Exciton-exciton annihilation in mose2 monolayers," *Phys. Rev. B*, vol. 89, p. 125 427, 12 Mar. 2014. DOI: `10.1103/PhysRevB.89.125427`. [Online]. Available: `https://link.aps.org/doi/10.1103/PhysRevB.89.125427`.

[46] Y. Long and H. Libai, "Exciton dynamics and annihilation in ws2 2d semiconductors," *Nanoscale*, vol. 7, pp. 7402–7408, Mar. 2015. DOI: `10.1039/C5NR00383K`.

[47] A. Tanoh, J. Alexander-Webber, J. Xiao, *et al.*, "Enhancing photoluminescence and mobilities in ws2 monolayers with oleic acid ligands," *Nano Letters*, vol. 19, Aug. 2019. DOI: `10.1021/acs.nanolett.9b02431`.

[48] H. Kim, G. Ahn, J. Cho, *et al.*, "Synthetic wse 2 monolayers with high photoluminescence quantum yield," *Science Advances*, vol. 5, eaau4728, Jan. 2019. DOI: `10.1126/sciadv.aau4728`.

[49] Z. Lin, B. Carvalho, E. Kahn, R. Lv, R. Rao, H. Terrones, M. Pimenta, and M. Terrones, "Defect engineering of two-dimensional transition metal dichalcogenides," *2D Materials*, vol. 3, p. 022 002, Apr. 2016. DOI: `10.1088/2053-1583/3/2/022002`.

[50] S. McDonnell, R. Addou, C. Buie, R. M. Wallace, and C. L. Hinkle, "Defect-dominated doping and contact resistance in mos2," *ACS Nano*, vol. 8, no. 3, pp. 2880–2888, 2014, PMID: 24484444. DOI: `10.1021/nn500044q`. [Online]. Available: `https://doi.org/10.1021/nn500044q`.

[51] A. Goodman, A. Willard, and W. Tisdale, "Exciton trapping is responsible for the long apparent lifetime in acid-treated mos2," *Physical Review B*, vol. 96, Jun. 2017. DOI: `10.1103/PhysRevB.96.121404`.

[52] C. Robert, D. Lagarde, F. Cadiz, *et al.*, "Exciton radiative lifetime in transition metal dichalcogenide monolayers," *Phys. Rev. B*, vol. 93, p. 205 423, 20 May 2016. DOI: `10.1103/PhysRevB.93.205423`. [Online]. Available: `https://link.aps.org/doi/10.1103/PhysRevB.93.205423`.

[53] T. Deilmann and K. S. Thygesen, "Dark excitations in monolayer transition metal dichalcogenides," *Phys. Rev. B*, vol. 96, p. 201 113, 20 Nov. 2017. DOI: `10.1103/PhysRevB.96.201113`. [Online]. Available: `https://link.aps.org/doi/10.1103/PhysRevB.96.201113`.

[54] A. O. Slobodeniuk and D. M. Basko, "Exciton-phonon relaxation bottleneck and radiative decay of thermal exciton reservoir in two-dimensional materials," *Phys. Rev. B*, vol. 94, p. 205 423, 20 Nov. 2016. DOI: `10.1103/PhysRevB.94.205423`. [Online]. Available: `https://link.aps.org/doi/10.1103/PhysRevB.94.205423`.

[55] T. Søndergaard, *Green's Function Integral Equation Methods in Nano-Optics*. Boca Raton, 2019.

[56] T. Venanzi, H. Arora, S. Winnerl, *et al.*, "Photoluminescence dynamics in few-layer inse," *Physical Review Materials*, vol. 4, Apr. 2020. DOI: `10.1103/PhysRevMaterials.4.044001`.

[57] H.-C. Chang, C.-L. Tu, K.-I. Lin, J. Pu, T. Takenobu, C.-N. Hsiao, and C.-H. Chen, "Synthesis of large-area inse monolayers by chemical vapor deposition," *Small (Weinheim an der Bergstrasse, Germany)*, vol. 14, e1802351, Aug. 2018. DOI: `10.1002/smll.201802351`.

[58] J. D. Jackson, *Classical electrodynamics*, 3rd ed. New York, NY: Wiley, 1999.

[59] F. Rasmussen and K. Thygesen, "Computational 2d materials database: Electronic structure of transition-metal dichalcogenides and oxides," English, *The Journal of Physical Chemistry Part C*, vol. 119, no. 23, pp. 13 169–13 183, 2015, ISSN: 1932-7447. DOI: `10.1021/acs.jpcc.5b02950`.

[60] P. Milonni, "Field quantization and radiative processes in dispersive dielectric media," *Journal of Modern Optics*, vol. 42, no. 10, pp. 1991–2004, 1995. DOI: `10.1080/09500349514551741`. eprint: `https://doi.org/10.1080/09500349514551741`. [Online]. Available: `https://doi.org/10.1080/09500349514551741`.

[61] D. C. Liu and J. Nocedal, "On the limited memory bfgs method for large scale optimization," *Mathematical Programming*, vol. 45, pp. 503–528, 1989.

[62] R. Fletcher, "A new approach to variable metric algorithms," *The Computer Journal*, vol. 13, no. 3, pp. 317–322, Jan. 1970, ISSN: 0010-4620. DOI: `10.1093/comjnl/13.3.317`. eprint: `https://academic.oup.com/comjnl/article-pdf/13/3/317/988678/130317.pdf`. [Online]. Available: `https://doi.org/10.1093/comjnl/13.3.317`.

[63] C. G. BROYDEN, "The Convergence of a Class of Double-rank Minimization Algorithms 1. General Considerations," *IMA Journal of Applied Mathematics*, vol. 6, no. 1, pp. 76–90, Mar. 1970, ISSN: 0272-4960. DOI: `10.1093/imamat/6.1.76`. eprint: `https://academic.oup.com/imamat/article-pdf/6/1/76/2233756/6-1-76.pdf`. [Online]. Available: `https://doi.org/10.1093/imamat/6.1.76`.

[64] D. Goldfarb, "A family of variable-metric methods derived by variational means," *Mathematics of Computation*, vol. 24, no. 109, pp. 23–26, 1970, ISSN: 00255718, 10886842. [Online]. Available: `http://www.jstor.org/stable/2004873`.

[65] D. F. Shanno, “Conditioning of quasi-newton methods for function minimization,” *Mathematics of Computation*, vol. 24, no. 111, pp. 647–656, 1970, ISSN: 00255718, 10886842. [Online]. Available: `http://www.jstor.org/stable/2004840`.

[66] G. A. Ermolaev, D. I. Yakubovsky, Y. V. Stebunov, A. V. Arsenin, and V. S. Volkov, “Spectral ellipsometry of monolayer transition metal dichalcogenides: Analysis of excitonic peaks in dispersion,” *Journal of Vacuum Science & Technology B*, vol. 38, no. 1, p. 014 002, 2020. DOI: `10.1116/1.5122683`. [Online]. Available: `https://doi.org/10.1116/1.5122683`.

[67] I. H. Malitson, “Interspecimen comparison of the refractive index of fused silica,” *J. Opt. Soc. Am.*, vol. 55, no. 10, pp. 1205–1209, Oct. 1965. DOI: `10.1364/JOSA.55.001205`. [Online]. Available: `http://www.osapublishing.org/abstract.cfm?URI=josa-55-10-1205`.

A Appendix

A.1 Quantum Harmonic Oscillator - Annihilation and Creation Operators

Consider the Hamiltonian of a one-dimensional quantum mechanical system with a harmonic potential, namely

$$\hat{\mathcal{H}} = \frac{\hat{p}^2}{2m} + \frac{1}{2}m\omega^2\hat{r}^2. \tag{A.1.1}$$

Here, $\hat{\mathbf{p}} = -i\hbar\nabla$ is the momentum operator and $\hat{\mathbf{r}} = \mathbf{r}$ is simply the position operator. From here, two new operators may be defined, which are given as

$$\hat{a} = \frac{1}{\sqrt{2m\hbar\omega}}(m\omega\hat{r} + i\hat{p}), \tag{A.1.2}$$

$$\hat{a}^\dagger = \frac{1}{\sqrt{2m\hbar\omega}}(m\omega\hat{r} - i\hat{p}). \tag{A.1.3}$$

$\hat{a}$ and $\hat{a}^\dagger$ are called the *annihilation/destruction*- and *creation* operator of the harmonic oscillator, respectively. They do not represent any observable of the system [21], they do however have very useful properties for further calculations. By rearranging, the following can be seen:

$$\hat{r} = \sqrt{\frac{\hbar}{2m\omega}}(\hat{a}^\dagger + \hat{a}), \tag{A.1.4}$$

$$\hat{p} = i\sqrt{\frac{m\hbar\omega}{2}}(\hat{a}^\dagger - \hat{a}). \tag{A.1.5}$$

Using the commutation relation of $\hat{p}$ and $\hat{r}$, namely that $[\hat{r}, \hat{p}] = i\hbar$, it can easily be shown that

$$\hat{a}\hat{a}^\dagger = \frac{1}{\hbar\omega}\left(\hat{\mathcal{H}} + \frac{1}{2}\hbar\omega\right), \tag{A.1.6}$$

$$\hat{a}^\dagger\hat{a} = \frac{1}{\hbar\omega}\left(\hat{\mathcal{H}} - \frac{1}{2}\hbar\omega\right). \tag{A.1.7}$$

This shows, that $[\hat{a}, \hat{a}^\dagger] = 1$. Moreover, by adding equations (A.1.6) and (A.1.7), it can be seen that

$$\hat{\mathcal{H}} = \frac{1}{2}\hbar\omega\left(\hat{a}\hat{a}^\dagger + \hat{a}^\dagger\hat{a}\right) = \hbar\omega\left(\hat{a}^\dagger\hat{a} + \frac{1}{2}\right). \tag{A.1.8}$$

Thus, the Hamiltonian can be written in terms of the two new operators. Now, let $|n\rangle$ denote the eigenstate with eigenvalue E_n. As such, the eigenvalue equation is now simply

$$\hat{\mathcal{H}}\,|n\rangle = \hbar\omega\left(\hat{a}^\dagger\hat{a} + \frac{1}{2}\right)|n\rangle = E_n\,|n\rangle. \tag{A.1.9}$$

Letting $\hat{a}^\dagger$ operate from the left on both sides of equation (A.1.9) results in

$$E_n \hat{a}^\dagger |n\rangle = \hbar\omega \left(\hat{a}^\dagger \hat{a}^\dagger \hat{a} + \frac{1}{2}\hat{a}^\dagger \right) |n\rangle \tag{A.1.10}$$

$$= \hbar\omega \left(\hat{a}^\dagger \hat{a} \hat{a}^\dagger - \hat{a}^\dagger + \frac{1}{2}\hat{a}^\dagger \right) |n\rangle . \tag{A.1.11}$$

Here, the commutation relation was put to use. Next, the equation can be rearranged such that it reads

$$\hbar\omega \left(\hat{a}^\dagger \hat{a} + \frac{1}{2} \right) \hat{a}^\dagger |n\rangle = \hat{\mathcal{H}} \hat{a}^\dagger |n\rangle = (E_n + \hbar\omega)\, \hat{a}^\dagger |n\rangle . \tag{A.1.12}$$

As such, the harmonic oscillator has an eigenstate $\hat{a}^\dagger |n\rangle$ with corresponding eigenvalue $E_n + \hbar\omega$. This eigenstate and eigenvalue will be denoted as $\hat{a}^\dagger |n\rangle = |n+1\rangle$ and $E_n + \hbar\omega = E_{n+1}$. Now equation (A.1.12) can be rewritten as

$$\hat{\mathcal{H}} |n+1\rangle = E_{n+1} |n+1\rangle , \tag{A.1.13}$$

This means that for a given energy level, E_n, of the harmonic-oscillator, a higher energy level, E_{n+1}, differing by $\hbar\omega$ exists. As such, the energy levels are equispaced and have no upper bounds, the latter of these properties agreeing with classical mechanics. Analogously, it can be shown that

$$\hat{\mathcal{H}} \hat{a} |a\rangle = E_{n-1} \hat{a} |n\rangle , \tag{A.1.14}$$

where $E_{n-1} = E_n - \hbar\omega$ is the eigenvalue of the eigenstate $\hat{a}|n\rangle$. Using a similar notation as previously, one can write equation (A.1.14) as

$$\hat{\mathcal{H}} |n-1\rangle = E_{n-1} |n\rangle , \tag{A.1.15}$$

where $|n-1\rangle = \hat{a}|n\rangle$. However, the total energy of the oscillator is positive, implying a lower bound. As such, iterative use of $\hat{a}$ on any eigenstate should at some point result in the ground state, which will be denoted as $|0\rangle$ with energy E_0. As such, when considering

$$\hat{\mathcal{H}} \hat{a} |0\rangle = (E_0 - \hbar\omega) \hat{a} |0\rangle , \tag{A.1.16}$$

the only solution must be $\hat{a}|0\rangle = 0$, since there is no eigenstate of lower energy than the ground state. Using this solution for the ground state in equation (A.1.9), it can be seen that

$$\hat{\mathcal{H}} |0\rangle = \frac{1}{2}\hbar\omega |0\rangle = E_0 |0\rangle . \tag{A.1.17}$$

This means that $E_0 = \hbar\omega/2$, which leads to

$$E_n = \left(n + \frac{1}{2} \right) \hbar\omega, \quad n = 1, 2, 3, ..., \tag{A.1.18}$$

and this is in agreement with the usual result for the quantum harmonic oscillator. In conclusion, the operators $\hat{a}$ and $\hat{a}^\dagger$ respectively destroys or creates a quantum of energy with a value of $\hbar\omega$ in the oscillators excitation energy.

A.1.1 Number Operator

The number operator, denoted $\hat{n}$, may be defined as

$$\hat{n} = \hat{a}^{\dagger}\hat{a}. \tag{A.1.19}$$

When looking at equation (A.1.9) and (A.1.18), it is evident that

$$\hat{n}\left|n\right\rangle = n\left|n\right\rangle. \tag{A.1.20}$$

The derivation so far has not taken normalisation of the eigenstates $|n\rangle$ into account. If the eigenstates are normalised, the following conditions must hold true, namely that

$$\langle n-1\,|\,n-1\rangle = \langle n\,|\,n\rangle = \langle n+1\,|\,n+1\rangle = 1, \quad n > 0. \tag{A.1.21}$$

When different normalised eigenstates are related, additional factors must appear. As an example, the unnormalised relation from before reads $|n-1\rangle = \hat{a}\,|n\rangle$, which can be compared to the normalised case, namely

$$C_n\left|n-1\right\rangle = \hat{a}\left|n\right\rangle. \tag{A.1.22}$$

Now, by using the Hermitian conjugate on both sides, it can be seen that

$$\begin{aligned}\left\langle n-1\right| C_n^{\dagger}C_n\left|n-1\right\rangle &= \left\langle n\right|\hat{a}^{\dagger}\hat{a}\left|n\right\rangle,\\ |C_n|^2 &= n.\end{aligned} \tag{A.1.23}$$

Ultimately, this results in the expression, that

$$\hat{a}\left|n\right\rangle = n^{\frac{1}{2}}\left|n-1\right\rangle, \tag{A.1.24}$$

which is in agreement with the expected result of the ground state. The same approach can be used for $\hat{a}^{\dagger}\,|n\rangle = |n+1\rangle$, meaning

$$\hat{a}^{\dagger}\left|n\right\rangle = (n+1)^{\frac{1}{2}}\left|n+1\right\rangle. \tag{A.1.25}$$

Since it can be advantageous to work with normalised eigenstates, equation (A.1.24) and equation (A.1.25) will be the preferred equations to work with. Moreover, different eigenstates of the oscillator are orthogonal. As such, the only nonvanishing matrix elements of the annihilation and creation operaters are

$$\langle n-1|\hat{a}|n\rangle = n^{\frac{1}{2}} \quad \text{and} \quad \langle n+1|\hat{a}^{\dagger}|n\rangle = (n+1)^{\frac{1}{2}}, \tag{A.1.26}$$

respectively.

A.2 The Projector Augmented Wave Method

The purpose of this section is to give a description of the basic theory of the projector augmented wave (PAW) method. This knowledge is the foundation of all calculation in this report. Due to the orthogonality of wave functions in density functional theory (DFT), they will oscillate rapidly close to the core of an atom, since all the states are non-zero in this region. When moving substantially further away from the core, only the higher energy states are non-zero, meaning the the wave function in this area is a lot smoother.

A.2.1 Transformation Operator

To address the problem of the wave function being significantly different in varying regions of space, a linear transformation $\hat{\mathcal{T}}$ is needed. This transformation should take an auxiliary smooth wave function $|\tilde{\psi}_n\rangle$ to the all true Kohn-Sham (KS) single particle wave function $|\psi_n\rangle$, as such

$$|\psi_n\rangle = \hat{\mathcal{T}}\,|\tilde{\psi}_n\rangle\,, \tag{A.2.1}$$

where the subscript n contains a $\mathbf{k}$ index, a band index and a spin index. The transformed KS equation is then given by

$$\hat{\mathcal{T}}^\dagger \hat{H} \hat{\mathcal{T}}\,|\tilde{\psi}_n\rangle = \varepsilon_n \hat{\mathcal{T}}^\dagger \hat{\mathcal{T}}\,|\tilde{\psi}_n\rangle\,. \tag{A.2.2}$$

Now $\hat{\mathcal{T}}$ has to be defined in a suitable way, such that the auxiliary wave functions becomes smooth, when solving equation (A.2.2). Since the wave function already is smooth from a curtain minimum distance from the core, then $\hat{\mathcal{T}}$ only has to modify the wave function below this minimum. This minimum can be seen as an augmentation sphere. Therefore, $\hat{\mathcal{T}}$ should be defined as

$$\hat{\mathcal{T}} = 1 + \sum_a \hat{\mathcal{T}}^a, \tag{A.2.3}$$

where a is an atom index, and $\hat{\mathcal{T}}^a$ is an atom centered transformation, which has no effect outside the augmentation sphere, given as $|\mathbf{r} - \mathbf{R}^a| < r_c^a$. The cut-off radii, r_c^a, is chosen such that there is no overlap between augmentation spheres of different atoms. Now for each of the partial waves ϕ_i^a of the total wave function, a corresponding smooth auxiliary partial wave function, $\tilde{\phi}_i^a$ is defined such that

$$|\phi_i^a\rangle = \left(1 + \hat{\mathcal{T}}^a\right)|\tilde{\phi}_i^a\rangle \quad \Longleftrightarrow \quad \hat{\mathcal{T}}^a\,|\tilde{\phi}_i^a\rangle = |\phi_i^a\rangle - |\tilde{\phi}_i^a\rangle \tag{A.2.4}$$

for all i, a. Since $\hat{\mathcal{T}}^a$ has no effect outside the augmentation spheres, this requires the partial waves to be the same outside the spheres, meaning

$$\forall a, \quad \phi_i^a(\mathbf{r}) = \tilde{\phi}_i^a(\mathbf{r}), \text{ for } r > r_c^a. \tag{A.2.5}$$

The smooth partial wave function is assumed to form a complete set inside the sphere, which means it can be expanded as

$$|\tilde{\psi}_n\rangle = \sum_i P_{ni}^a\,|\tilde{\phi}_i^a\rangle\,, \text{ for } |\mathbf{r} - \mathbf{R}^a| < r_c^a, \tag{A.2.6}$$

where P_{ni}^a is an unknown expansion factor. With the knowledge that $|\phi_i^a\rangle = \hat{\mathcal{T}}\,|\tilde{\phi}_i^a\rangle$, it can be seen that

$$|\psi_n\rangle = \hat{\mathcal{T}}\,|\tilde{\psi}_n\rangle = \sum_i P_{ni}^a\,|\phi_i^a\rangle\,, \text{ for } |\mathbf{r} - \mathbf{R}^a| < r_c^a, \tag{A.2.7}$$

which means that ψ and $\tilde{\psi}$ have the exact same expansion coefficients. Due to the assumption of $\hat{\mathcal{T}}$ being linear, the expansion coefficients must be linear functionals of $|\tilde{\psi}_n\rangle$, meaning that

$$P_{ni}^a = \langle \tilde{p}_i^a | \tilde{\psi}_n \rangle = \int \tilde{p}_i^{a*} \left(\mathbf{r} - \mathbf{R}^a \right) \tilde{\psi}_n(\mathbf{r}) d\mathbf{r}, \tag{A.2.8}$$

where $|\tilde{p}_i^a\rangle$ are some fixed functions termed smooth projector functions [8]. Due to the lack of overlap between each augmentation sphere, the one center expansion of the smooth all electron wave function $|\tilde{\psi}_n^a\rangle = \sum_i |\phi_i^a\rangle \langle \tilde{p}_i^a | \tilde{\psi}_n \rangle$ is expected to reduce to $|\tilde{\psi}\rangle$ itself inside the augmentation sphere denoted by a. This means the smooth projector function must satisfy

$$\sum_i |\tilde{\phi}_i^a\rangle \langle \tilde{p}_i^a| = 1, \tag{A.2.9}$$

inside each of the augmentation spheres. Thus, this also means that

$$\langle \tilde{p}_{i_1}^a | \tilde{\phi}_{i_2}^a \rangle = \delta_{i_1, i_2}, \text{ for } |\mathbf{r} - \mathbf{R}^a| < r_c^a, \tag{A.2.10}$$

in other words this implies the projector function is orthonormal to the smooth partial waves inside the augmentation spheres. Now by combining equation (A.2.4) and (A.2.9), it can be seen that

$$\hat{\mathcal{T}}^a = \sum_i \hat{\mathcal{T}}^a \, |\tilde{\phi}_i^a\rangle \langle \tilde{p}_i^a| = \sum_i \left(|\phi_i^a\rangle - |\tilde{\phi}_i^a\rangle \right) \langle \tilde{p}_i^a| \, . \tag{A.2.11}$$

Now by using equation (A.2.3) an expression for the linear transformation $\hat{\mathcal{T}}$ can be found,

$$\hat{\mathcal{T}} = 1 + \sum_a \sum_i \left(|\phi_i^a\rangle - |\tilde{\phi}_i^a\rangle \right) \langle \tilde{p}_i^a| \, . \tag{A.2.12}$$

Then the transformation of the all electron KS wave function, $\psi_n(\mathbf{r}) = \langle \mathbf{r} | \psi_n \rangle$ can be obtained as

$$\psi_n(\mathbf{r}) = \tilde{\psi}_n(\mathbf{r}) + \sum_a \sum_i \left(\phi_i^a(\mathbf{r}) - \tilde{\phi}_i^a(\mathbf{r}) \right) \langle \tilde{p}_i^a | \tilde{\psi}_n \rangle \, , \tag{A.2.13}$$

where $\tilde{\psi}_n(\mathbf{r})$ can be found by solving the eigenvalue problem in equation (A.2.2).

A.2.2 Local Operator Matrix Elements

Consider a local operator, $\hat{O}$. An operator is said to be local if it does not correlate separate parts of space [8], that is if

$$\langle \mathbf{r} | \hat{O} | \mathbf{r}' \rangle = 0 \quad \text{for} \quad \mathbf{r} \neq \mathbf{r}'. \tag{A.2.14}$$

In the PAW formalism, the local operator matrix element between two different states, ψ_n and $\psi_{n'}$, can be expressed using equation (A.2.13) as

$$\begin{aligned} \langle \psi_n | \hat{O} | \psi_{n'} \rangle = {} & \langle \tilde{\psi}_n | \hat{O} | \tilde{\psi}_{n'} \rangle \\ & + \sum_{a,i} \langle \tilde{p}_i^a | \tilde{\psi}_n \rangle^* \langle \phi_i^a(\mathbf{r}) - \tilde{\phi}_i^a(\mathbf{r}) | \hat{O} | \tilde{\psi}_{n'} \rangle \\ & + \sum_{b,j} \langle \tilde{p}_j^b | \tilde{\psi}_{n'} \rangle \langle \tilde{\psi}_n | \hat{O} | \phi_j^b(\mathbf{r}) - \tilde{\phi}_j^b(\mathbf{r}) \rangle \\ & + \sum_{a,i} \sum_{b,j} \delta_{ab} \langle \tilde{p}_i^a | \tilde{\psi}_n \rangle^* \langle \tilde{p}_j^b | \tilde{\psi}_{n'} \rangle \langle \phi_i^a(\mathbf{r}) - \tilde{\phi}_i^a(\mathbf{r}) | \hat{O} | \phi_j^b(\mathbf{r}) - \tilde{\phi}_j^b(\mathbf{r}) \rangle \, . \end{aligned} \tag{A.2.15}$$

The Kronecker delta-function on the last term occurs due to the operator being local. This can be seen by use of equation (A.2.5). If $\mathbf{r}$ is in augmentation sphere a and $a \neq b$, then $\phi_j^b(\mathbf{r}) - \tilde{\phi}_j^b(\mathbf{r})$

will vanish, and vice versa. If $\mathbf{r}$ is neither in augmentation spheres a or b, then both the bra and the ket will vanish. From here, equation (A.2.9) can be used, since

$$\langle \phi_i^a(\mathbf{r}) - \tilde{\phi}_i^a(\mathbf{r}) | \hat{O} | \tilde{\psi}_{n'} \rangle = \langle \phi_i^a(\mathbf{r}) - \tilde{\phi}_i^a(\mathbf{r}) | \hat{O} \sum_j | \tilde{\phi}_j^a \rangle \langle \tilde{p}_j^a | \tilde{\psi}_{n'} \rangle \,, \tag{A.2.16}$$

$$\langle \tilde{\psi}_n | \hat{O} | \phi_j^b(\mathbf{r}) - \tilde{\phi}_j^b(\mathbf{r}) \rangle = \langle \tilde{\psi}_n | \sum_i | \tilde{p}_i^b \rangle \langle \tilde{\phi}_i^b | \hat{O} | \phi_j^b(\mathbf{r}) - \tilde{\phi}_j^b(\mathbf{r}) \rangle \,. \tag{A.2.17}$$

Inserting these two expressions in equation (A.2.15), replacing b by a in the third term, and dissolving the Kronecker delta-function in the sum in the last term, makes the following expression come to life:

$$\begin{aligned}
\langle \psi_n | \hat{O} | \psi_{n'} \rangle = {} & \langle \tilde{\psi}_n | \hat{O} | \tilde{\psi}_{n'} \rangle \\
& + \sum_a \sum_{i,j} \langle \tilde{p}_i^a | \tilde{\psi}_n \rangle^* \langle \tilde{p}_j^a | \tilde{\psi}_{n'} \rangle \langle \phi_i^a(\mathbf{r}) - \tilde{\phi}_i^a(\mathbf{r}) | \hat{O} | \tilde{\phi}_j^a \rangle \\
& + \sum_a \sum_{i,j} \langle \tilde{p}_j^a | \tilde{\psi}_{n'} \rangle \langle \tilde{p}_i^a | \tilde{\psi}_n \rangle^* \langle \tilde{\phi}_i^a | \hat{O} | \phi_j^a(\mathbf{r}) - \tilde{\phi}_j^a(\mathbf{r}) \rangle \\
& + \sum_a \sum_{i,j} \langle \tilde{p}_i^a | \tilde{\psi}_n \rangle^* \langle \tilde{p}_j^a | \tilde{\psi}_{n'} \rangle \langle \phi_i^a(\mathbf{r}) - \tilde{\phi}_i^a(\mathbf{r}) | \hat{O} | \phi_j^a(\mathbf{r}) - \tilde{\phi}_j^a(\mathbf{r}) \rangle \,.
\end{aligned} \tag{A.2.18}$$

From here, the rest of the procedure simply involves cancelling equal terms of opposite sign, and the expression reduces to

$$\langle \psi_n | \hat{O} | \psi_{n'} \rangle = \langle \tilde{\psi}_n | \hat{O} | \tilde{\psi}_{n'} \rangle + \sum_a \sum_{i,j} \langle \tilde{p}_i^a | \tilde{\psi}_n \rangle^* \langle \tilde{p}_j^a | \tilde{\psi}_{n'} \rangle \Big(\langle \phi_i^a | \hat{O} | \phi_j^a \rangle - \langle \tilde{\phi}_i^a | \hat{O} | \tilde{\phi}_j^a \rangle \Big) \,. \tag{A.2.19}$$

A.3 Cavity Fresnel Coefficients

This section will concern itself with the derivation of the reflection coefficient, r^*_{down}. The two reflection coefficient, which are the starting point, can be seen in the following:

$$r^*_{\mathrm{up}} = r_E + t_E^2 r_{13} \mathrm{e}^{2id_3q_{z1}} \sum_{n=0}^{\infty} \left(r^*_{\mathrm{down}} r_{13} \mathrm{e}^{2id_3q_{z1}} \right)^n = r_E + \frac{t_E^2 r_{13} \mathrm{e}^{2id_3q_{z1}}}{1 - r^*_{\mathrm{down}} r_{13} \mathrm{e}^{2id_3q_{z1}}}, \tag{A.3.1}$$

$$r^*_{\mathrm{down}} = r_E + t_E^2 r_{12} \mathrm{e}^{2id_2q_{z1}} \sum_{n=0}^{\infty} \left(r^*_{\mathrm{up}} r_{12} \mathrm{e}^{2id_2q_{z1}} \right)^n = r_E + \frac{t_E^2 r_{12} \mathrm{e}^{2id_2q_{z1}}}{1 - r^*_{\mathrm{up}} r_{12} \mathrm{e}^{2id_2q_{z1}}}. \tag{A.3.2}$$

From here, we simply need to solve two equations with two variables. This is as follows:

$$r^*_{\mathrm{down}} = r_E + \frac{t_E^2 r_{12} \mathrm{e}^{2id_2q_{z1}}}{1 - r^*_{\mathrm{up}} r_{12} \mathrm{e}^{2id_2q_{z1}}} \tag{A.3.3}$$

$$\Rightarrow r^*_{\mathrm{up}} r_{12} \mathrm{e}^{2id_2q_{z1}} = 1 - \frac{t_E^2 r_{12} \mathrm{e}^{2id_2q_{z1}}}{r^*_{\mathrm{down}} - r_E} \tag{A.3.4}$$

$$\Rightarrow r_E r_{12} \mathrm{e}^{2id_2q_{z1}} + \frac{t_E^2 r_{12} r_{13} \mathrm{e}^{2i(d_3+d_2)q_{z1}}}{1 - r^*_{\mathrm{down}} r_{13} \mathrm{e}^{2id_3q_{z1}}} = 1 - \frac{t_E^2 r_{12} \mathrm{e}^{2id_2q_{z1}}}{r^*_{\mathrm{down}} - r_E} \tag{A.3.5}$$

$$\Rightarrow 1 - r_E r_{12} \mathrm{e}^{2id_2q_{z1}} = \frac{t_E^2 r_{12} r_{13} \mathrm{e}^{2i(d_3+d_2)q_{z1}}}{1 - r^*_{\mathrm{down}} r_{13} \mathrm{e}^{2id_3q_{z1}}} + \frac{t_E^2 r_{12} \mathrm{e}^{2id_2q_{z1}}}{r^*_{\mathrm{down}} - r_E} \tag{A.3.6}$$

$$= \frac{\left(1 - r^*_{\mathrm{down}} r_{13} \mathrm{e}^{2id_3q_{z1}}\right) t_E^2 r_{12} \mathrm{e}^{2id_2q_{z1}} + \left(r^*_{\mathrm{down}} - r_E\right) t_E^2 r_{12} r_{13} \mathrm{e}^{2i(d_3+d_2)q_{z1}}}{\left(1 - r^*_{\mathrm{down}} r_{13} \mathrm{e}^{2id_3q_{z1}}\right) \left(r^*_{\mathrm{down}} - r_E\right)} \tag{A.3.7}$$

$$= \frac{\left(1 - r_E r_{13} \mathrm{e}^{2id_3q_{z1}}\right) t_E^2 r_{12} \mathrm{e}^{2id_2q_{z1}}}{r^*_{\mathrm{down}} - r_E - (r^*_{\mathrm{down}})^2 r_{13} \mathrm{e}^{2id_3q_{z1}} + r_E r^*_{\mathrm{down}} r_{13} \mathrm{e}^{2id_3q_{z1}}} \tag{A.3.8}$$

$$\Rightarrow \frac{\left(1 + r_E r_{13} \mathrm{e}^{2id_3q_{z1}}\right) t_E^2 r_{12} \mathrm{e}^{2id_2q_{z1}}}{1 + r_E r_{12} \mathrm{e}^{2id_2q_{z1}}} + r_E = (1 + r_E r_{13} \mathrm{e}^{2id_3q_{z1}}) r^*_{\mathrm{down}} - (r^*_{\mathrm{down}})^2 r_{13} \mathrm{e}^{2id_3q_{z1}} \tag{A.3.9}$$

$$\Rightarrow r^*_{\mathrm{down}} = \frac{-1 - r_E r_{13} \mathrm{e}^{2id_3q_{z1}} \pm \sqrt{D_d}}{-2 r_{13} \mathrm{e}^{2id_3q_{z1}}}, \tag{A.3.10}$$

where

$$D_d = \left(1 - r_E r_{13} \mathrm{e}^{2id_3q_{z1}}\right)^2 - \frac{4\left(1 - r_E r_{13} \mathrm{e}^{2id_3q_{z1}}\right) t_E^2 r_{12} r_{13} \mathrm{e}^{2iq_{z1}(d_2+d_3)}}{1 + r_E r_{12} \mathrm{e}^{2id_2q_{z1}}}. \tag{A.3.11}$$